9-3-2013

Microwave Triggered Laser Ionization of Air

Ehsan Vadiee

Recommended Citation

Vadiee, Ehsan. "Microwave Triggered Laser Ionization of Air." (2013). https://digitalrepository.unm.edu/ece_etds/256

Ehsan Vadiee

Candidate

Electrical and Computer Engineering

Department

This thesis is approved, and it is acceptable in quality and form for publication:

Approved by the Thesis Committee:

Edl Schamiloglu , Chairperson

Christos Christodoulou

Sarita Prasad

Microwave Triggered Laser Ionization of Air

By

Ehsan Vadiee

B.S., Science and Research University, 2010

THESIS

Submitted in Partial Fulfillment of the

Requirements for the Degree of

Master of Science

Electrical Engineering

The University of New Mexico

Albuquerque, New Mexico

July, 2013

DEDICATION

To My Parents and

My Dear Uncle

Acknowledgments

Microwave Triggered Laser Ionization of Air

By

Ehsan Vadiee

M.S., Electrical Engineering, University of New Mexico, 2013

ABSTRACT

In this thesis the measurements and analyses of high power electromagnetic wave interaction with a laser-induced plasma (LIP) have been investigated. The laser-induced breakdown processes in air generated by focusing a 600 mJ, 7 ns pulselength, 1064 nm wavelength Nd:YAG laser onto a 30 µm spot size at an atmospheric pressure of 631 Torr are examined. The breakdown threshold electric field is measured and compared with classical and quantum theoretical ionization models at this short wavelength. A universal scaling analysis of these results allows one to predict some aspects of high power microwave (HPM) breakdown based on measured laser breakdown observations. The 1064 nm laser-induced effective field intensities for air breakdown data calculated based on the collisional cascade and multiphoton breakdown theories are used to compare with the experimental results.

Experimental diagnostics of the laser deposition are interpreted using the compressible spatially adaptive radiation magnetohydrodynamic particle-in-cell code MAGIC invoking the ponderomotive approximation to describe the laser–plasma interaction. The 2-D MATLAB simulations of the temporal and spatial evolution of the LIP are also in agreement with the theoretical results.

An X-band relativistic backward wave oscillator (RBWO) at the Pulsed Power, Beams, and Microwaves Laboratory was constructed at the University of New Mexico (UNM) and is used as the HPM source. The RBWO produces a microwave pulse of

maximum power 400 MW, frequency of 10.1 GHz, and energy of 6.8 Joules. Special care was given to synchronize the RBWO and the pulsed laser system in order to achieve a high degree of spatial and temporal overlap. Different detectors are used to observe the overlap- a photodiode (PD), microphone, microwave detector, and others. Shadowgraphy with a nanosecond time resolution will be used to detect changes in the shockwave fronts when the HPM signal overlaps the laser pulse in time and space. Detailed experimental setup and experimental results are presented.

A complete theoretical investigation using the impedance transformation method including scattering, partial reflections, and collisional absorption based on the transfer of energy from the wave to the plasma and generation of fast electrons, is presented. A discussion on the effects of various unmagnetized plasma parameters on the transmitted, absorbed, and reflected power is presented.

Index Terms - Laser-Induced Plasma, Nd:YAG Laser, Shadowgraphy, Spectroscopy, Air Plasma, Electromagnetic Waves, High Power Microwaves, Wave Propagation, Plasma Diagnostics.

TABLE OF CONTENTS

List of Figures

CHAPTER 1

INTRODUCTION

The motivation of this study is the possibility of drag reduction/flight control in supersonic flight using plasmas. There are two main aspects for flight control: vehicle maneuverability and vehicle trim. They can generally be improved by either modification of the surface forces or thrust vectoring. Energy deposition in an extended path of air, along the vehicle velocity vector and ahead of the shockwave, can change the pressure distribution of the vehicle and cause extra thrust force. Energy deposition creates a long, low density, high temperature, and low pressure region of plasma that we can term a plasmoid. It can mitigate the shock and reduce drag. Some shock interactions can often lead to catastrophic events for a vehicle. Drag reduction reduces the air resistance and fuel consumption greatly. Furthermore, it leads to less stringent material requirements, less damage due to shock interference, and increased performance envelopes .

The scope of this research is broad. It encompasses a wide variety of energy deposition techniques (e.g., plasma arcs, laser pulse, microwaves, electron beams, glow discharge, etc.) and a wide range of applications (e.g., drag reduction, lift and moment enhancement, improved combustion and mixing, modification of shock structure, etc.). However, energy deposition with microwaves and a laser discharge has several advantages such as: 1) The actuation time is effectively instantaneous compared to characteristic flow field timescales; 2) the energy deposition can be positioned either on or off the vehicle, 3) the possibility of pushing air out of a vehicle's way, several meters, ahead of the vehicle .

To realize energy deposition effects on the supersonic vehicle's performance, we can use laser radiation to produce an extended strip of hot, ionized gas. Generally, through focusing the energetic laser beam to a point, air can be ionized. The high energy, short laser pulses have been found to propagate over large distances while heating and ionizing the air in their path. This is referred to as filamentation. The filamenting pulses have been found to extend over a few tens of

meters and the filament diameters have been reported to range from 0.1 to several millimeters. The objective is to create a long narrow path of heated gas that can be scaled to large dimensions.

It has been shown numerically and experimentally that an increased shock speed and decreased pressure jump are experienced when a shockwave encounters a heated swath of gas. When the vehicle moves through the heated region the semispherical shockwaves continue to move outwards. Thus, the vehicle sees a low density region with its shockwave expanding outwards. The air remaining within the expanding shockwave reaches a high temperature, with a lower density and higher speed of sound in comparison to the surrounding air.

The energy can be deposited either at a point ahead of the shockwave, or in an extended region oriented in the direction of the shockwave's propagation. In our study, we investigated the possibility of drag reduction due to a point source. The point heating results in pressure change but the overall impact on the shockwave is still minimal. In terms of supersonic vehicle flight, a small amount of air can be pushed outwards from the point source. Our goal in this research is to create a larger point source, along with shockwaves, by synchronizing a short pulse laser with an HPM wave beam. It can give us a better approximation to model an extended region of filamentation.

In this chapter, a review is given of laser-induced gas breakdown and the interaction of an HPM wave beam and a laser plasma in atmospheric air at the altitude of the laboratory. 1064 nm laser-induced breakdown research is introduced, and the measured breakdown threshold based on microwave breakdown theory is discussed. Multiphoton and cascade ionization processes are also discussed. The diagnostics of a 1064 nm LIP include a shockwave diagnostic, laser shadowgraphy, optical emission PD, and open shutter camera. The focus of this work is to study the evolution and dynamics of plasma expansion when an HPM wave beam is overlapped in space and time with a very small, localized region of plasma formed by a high energy laser pulse.

The organization of the remainder of this thesis is summarized in Section 1.3.

1.1. Overview of the 1064 nm Laser-induced Plasma and Microwave Discharge in Atmosphere

The ionization energy of air can be obtained by the relative average of the ionization potentials of its constitutive parameters - nitrogen, oxygen, and helium. The ionization potential of air is 15.6 eV. The photon energy of visible and infrared laser radiation is below this and, thus, it

requires 10-300 photons to be absorbed within an excitation lifetime of the order of $<10^{-14}$ s. Therefore, the ionization process of infrared and visible lasers is mostly related to collisional cascade ionization (CCI). The photon energy for the 1064 nm laser with pulse duration 7 ns and energy per pulse of 600 mJ is $\varepsilon_\gamma = h\nu = 1.167 \, eV$ requiring approximately 14 photons ($N = \frac{W_i}{\varepsilon_\gamma} = \frac{16.6 \, eV}{1.167 \, eV} \approx 14$ photons) to be absorbed in a quantum lifetime of $\tau = \frac{\hbar}{\varepsilon_\gamma} = 5.1 \times 10^{-16}$ s for the ionization of air. In the infrared regime, for our experimental case of Q-switched laser radiation at 1064 nm, 14 photons are required to be absorbed within a short excitation time [8]. The total number of photons per pulse is 3.1×10^{18}, which means that if the laser is focused, breakdown initiation is very quick. Therefore, multiphoton ionization (MPI) plays the dominant role in the air breakdown initiation mechanism.

Generally, CCI best describes breakdown at long laser pulselengths (>10 ns) and high pressures (>0.14 atm). MPI theory best describes breakdown at short pulselengths (<1 ns) and low pressure (mTorr) [1].

The measurements and analyses are studied for air breakdown processes generated by focusing a 1064 nm, 600 mJ, 7 ns high power IR laser radiation onto a 50 μm spot size ($w = f\alpha/2$). This produces laser power densities up to a few TW/cm^2. This is well above the threshold power flux required for the ionization of air, 10^8-10^{10} W/cm^2 [2].

The laser breakdown is analyzed and compared with quantum statistical and classical ionization models [9],[10]. Our investigation of the breakdown threshold field intensities for air using a Nd:YAG 1064 nm Q-switched laser radiation is extended to the threshold field requirements by using HPM radiation [3].

The features of the LIP are diagnosed using several optical diagnostics. The plasma shadowgraphy technique is also employed [4] using a fast gated imaging technique for visualizing the laser-induced gas-dynamic processes of the LIP. Shadowgraphy measurements in and near the focus can shed light on typical post-breakdown effects. Shadowgraphy can measure the shockwave immediately after the breakdown of air and the dynamics of the plasma expansion.

A high resolution microphone is employed to analyze the intensity of sound waves created by the breakdown and the decay time of the plasma. The plasma decay measurements are compared with a simplified decay model based on the continuity equation to analyze the dominant loss mechanisms involved, such as recombination losses and diffusion loss.

The HPM waves are ordinary electromagnetic radiation and the generation of plasma using them can be described using basic electromagnetic theory. The microwave plasmas are often of particular interest due to their ability to provide a high density of charged particles and active species. Under the strong pulsed RF electric field, electrons gain sufficient energy to overcome the ionization potential, and if there is sufficient ionization, the electron density grows exponentially with ionization rate ν_i. The HPM breakdown has been investigated experimentally ,[5] and computationally [6].

1.2. Review of Microwave-Assisted Laser-Induced Breakdown Research

The interaction of electromagnetic waves and tunable LIP media has been studied by various authors as an important topic in plasma wave applications [7], [8]. By using plasma layers, optimal reflection, absorption, and transmission required in stealth applications, radio communications, ultrafast vehicles, radio astronomy, etc., can be studied. In the article by Vidmar [9] it was suggested that a nonuniform plasma slab can be used as a broadband radar absorbing layer. Interaction between electromagnetic waves and an unmagnetized plasma is numerically studied in [10]. In a subsequent study, the results of the interaction of RF waves and plasma generated at atmospheric pressure are presented [11]. The scattering matrix method is suggested for the analysis of electromagnetic wave propagation through plasmas [12]. Guo and Wang [13] have studied the features of electromagnetic wave incident onto a uniform plasma covering the surface of a metal in atmosphere as the function of plasma parameters. In addition to the general absorption, reflection, and transmission behaviors, special plasma responses are also discussed in the literature. Gradov and Stenflo [4] have discussed the possibility of a nonlinear transparency of dense magnetized plasma and showed that, because of the parametric excitation of surface waves, a significant part of the radiation can penetrate through the plasma. They have suggested a mechanism to increase the transmitted and reflected electromagnetic wave power from a plasma having properly varied the slab density temporally. They indicated that the total radiation energy can be greater than the incident energy due to the release of the stored wave energy in the plasma during short periods.

In the literature, various plasma electron density distributions are studied, such as parabolic, exponential, sinusoidal, and steepened profiles to obtain special characteristics [14]. Frequency

selective characteristics are also discussed as a function of the plasma density profile parameters. Similar to nonuniform plasmas, uniform plasmas are also analyzed in the literature with constant electron density [5]. In [5], electromagnetic wave propagation through a plasma layer with parabolic electron density distribution is studied as a new plasma medium to determine special reflection, absorption, and transmission behaviors. The plasma medium is taken as weakly ionized, steady state, cold, and collisional. The background magnetic field is negligible. A parabolic electron density distribution is used to model the electron density of the LIP. It provides matching of the electromagnetic wave and it is used to obtain improved absorption and transmission characteristics. As shown in [5], these characteristics are tunable by means of laser radiation.

In our analysis, the entire plasma layer is divided into thin, adjacent slabs with constant plasma parameters. Then starting with Maxwell's equations, expressions for the reflected, absorbed, and transmitted powers are derived. The effects of collision frequency, maximum electron density, the lengths of two parts of the density function with respect to each other, and external magnetic field strength are discussed to determine appropriate conditions for broadband and tunable absorption performance accompanied with narrowband reflection behavior.

1.3. Organization of the Thesis

This thesis is organized as follows: Chapters 2 to 5 provide theoretical foundations to our research work. The characteristics of the LIPs are discussed in Chapter 2. In Chapter 3 the theoretical estimates of the breakdown threshold for air using classical collisional cascade theory and MPI theory are discussed. In addition, a method for scaling the measured laser breakdown threshold with the classical microwave breakdown is also discussed. The theoretical and simulation analysis of a LIP and its interaction with HPM radiation is modeled and presented in Chapter 4. A description of the plasma diagnostics used, such as shadowgraphy, acoustic emission, X-ray detector, and PDs, are discussed in Chapters 5, 6, and 7, respectively. Chapters 6 and 7 describe the experimental setup and analysis. Finally, conclusions and suggestions for future work are presented in Chapter 8.

CHAPTER 2

LASER-INDUCED PLASMA

2.1. Optical Breakdown of Gas

Optical breakdown initiation of air and other gases at atmospheric pressure requires laser intensity on the order of $10^{10} W/cm^2$. Although gases under normal pressure are transparent to laser radiation, by enhancing the laser intensity through focusing of the high power laser onto a small volume, they can be opaque and absorptive to laser light. In other words, if the focused laser intensity is stronger than the breakdown threshold of gas, of order $10^6 - 10^7 V/m$, optical breakdown occurs and is accompanied by a spark. Optical breakdown results in the production of charged particles, the absorption of laser light, and the re-radiation of light from the spark. A broad spectrum of emission can be measured from the re-radiation of the spark. The dimensions of the LIP depends on different parameters, such as the frequency of the laser used, the energy per pulse, pulsewidth, focal length, ambient pressure of the gas, and divergence of laser beam [15],[16],[17].

Initial electrons in the focal region within the intense laser beam can obtain sufficient energy through an inverse bremsstrahlung process and by collisions with neutral atoms they can initiate additional ionization. Breakdown causes a rapid rise in electron temperature, electron density, and modification of the electron distribution function f_e. Generally, the number of electrons can grow exponentially through two main processes - MPI and CCI [16],[18]. Breakdown will occur when the electron density reaches a certain critical value despite losses due to diffusion, recombination, etc., within the duration of the laser pulse [18],[3].

Figure 2.1 shows the original laser pulse and the laser profile transmitted through the plasma when breakdown occurs. In the early stages, it is clear that the laser pulse can propagate through the plasma suffering little attenuation. However, at later time after breakdown occurs, the plasma

becomes opaque, leading to a sudden decrease in the amplitude of the transmitted pulse as a spark is initiated. The plasma front has been observed to expand faster at the front and back of the laser pulse, but its expansion slows down following the end of laser pulse [19].
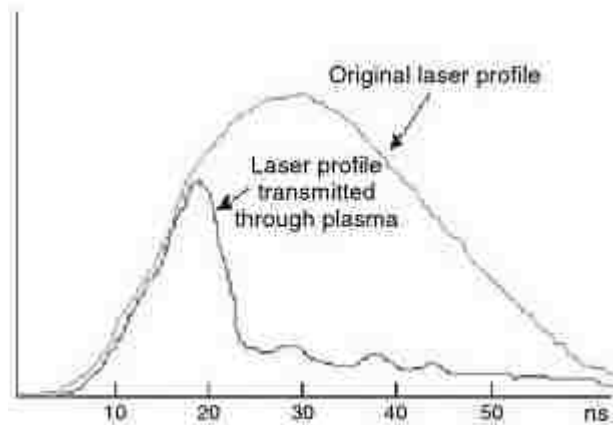
Figure 2.1. A schematic representation of the temporal profile of a laser pulse with and without gas breakdown showing attenuation of the laser pulse [18].

Optical breakdown generally consists of three parts:

1. Pre-ionization stage: In the rising phase of the laser, initial ionization is caused by MPI and inverse bremsstrahlung absorption [2] in which the first set of electrons are emitted from atoms and molecules that have absorbed laser photons. In ambient air, the initial electron density for optical breakdown is about 10^{13} m^{-3}. At low pressures, when collisions are infrequent, the most significant ionization process is MPI. At higher pressures, where collisions are important, CCI determines the evolution of ion and electron densities [17], [20].

2. Heating and expansion phase: after a certain delay, the plasma becomes very absorptive to the laser light, and due to deposition of laser pulse energy in a very short period of time, the plasma expands out from the focal region toward laser beam and shockwaves can propagate outwardly [16],[21].

3. Post-discharge phase: During the end of the laser pulse, the plasma is still expanding as a detonation wave.

Multiphoton, cascade, and avalanche ionization mechanisms are fundamentally different and are described using different theories.

2.2. Multiphoton Ionization

In MPI, multiple (N) simultaneous photons at wavelength λ/N with energy $Nh\nu$ strike bound electrons. As shown in Fig. 2.2, due to the very high flux density of the laser pulse, a bound electron can gain sufficient energy to be freed from the valance band by absorbing a photon's energy through inverse bremsstrahlung when the total energy of photons is greater than the ionization potential of the gas ($Nh\nu > I_p$) [29]. At low pressure due to the low density, the probability of collisional ionization is low and MPI theory best describes the optical breakdown. It is observed that, for gas pressures of 10 Torr and for laser pulses in the femtosecond regime, MPI is the dominant ionization process [18].
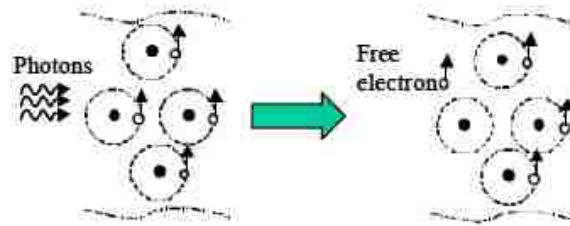
Figure 2.2 A schematic of the MPI process [2].

2.3. Collisional Cascade Ionization

To initialize CCI, a few electrons in the focal breakdown region of the laser are needed that could be liberated by MPI. Classically, the free electrons are accelerated by the electric field and lead to additional collisions with other neutral molecules and gas impurities. A large electric field can cause further ionization and more electrons will be liberated from elastic and inelastic collisions. After obtaining energy from photons that are greater than the ionization potential of the gas, more electrons with lower energy can be released from atomic bonds by inelastic collisions. Avalanche ionization processes are repeated throughout the focal region. If this process continues until an electron density in the range of $10^{18}\ cm^{-3}$ is obtained, breakdown occurs as a vivid spark. In general, the breakdown threshold is characterized as minimum laser intensities at which 10-50% of the laser pulses resulted in a visible optical breakdown [18],[30].

Avalanche ionization theory best describes breakdown at high gas pressure and long pulselengths compared to the momentum collision frequency between electrons and atoms ν_c. The rate at which an electron gains energy from the electric field can be written as [18]:

$$\frac{dW}{dt} = \frac{e^2 E_{eff}^2}{m \nu_c} \cdot \frac{\nu_c^2}{\nu_c^2 + \omega^2}$$

(2.1)

The effective field is given by $E_{eff}^2 = E_0^2 \left(\frac{\nu_c^2}{\nu_c^2 + \omega^2} \right)$, where ω is the angular frequency of the oscillating laser electric field.

In fact, two types of theories can be used to describe the CCI process: classical treatment and quantum-mechanical theory. The classical theory derives from microwave breakdown theory. If the radiation frequency ω is much greater than the collision frequency ν_c and if the photon energy $h\nu$ is greater than the ionization potential, the classical and quantum-mechanical descriptions give very similar results in term of describing the optical breakdown.

Due to the short pulse duration of the laser and the high breakdown threshold of air, LIPs have short MPI and CCI times, on the order of a nanosecond. Based on breakdown measurements and quantum mechanical theories, 88% of the total breakdown is related to the CCI process and about 12% of the ionization process is attributed to the MPI process at atmospheric pressure [21],[32]. The temporal profile of the experimental laser pulse is represented by the following expression [12]:

$$\varphi(t) = 0.274 \times \exp\left[-\exp\left(-0.0144 \times 10^9 t \times 2.92837 \right) - 0.295 \times 10^{-9} t + 6.2 \right]$$

(2.2)

Thus, the laser intensity is given by:

$$I(t) = \frac{W_1}{\pi (f\alpha)^2 \tau} \varphi(t)$$

(2.3)

where W_1 is the pulse energy (600 mJ), f is the focal length of the lens (5-15 cm), α is the divergence of the laser beam, and is the full-width-half-power maximum of the laser pulselength ($\tau = 8 \times 10^{-9}$s). Figure 2.3 shows the temporal variation of the laser energy for different focal lengths. Based on the intensity threshold of the MPI process, the MPI phase begins

with the increasing part of the laser pulse, more specially at τ =1 ns for f=5 cm and τ = 3 ns for f=15 cm. MPI lasts until the time when the laser beam absorption becomes very large and afterwards CCI becomes dominant. CCI starts at τ=3.4 ns for f=15 cm and τ=3.2 ns for f=5 cm.

Figure 2.3. Temporal variation of focused laser beam for P=1 atm and focal lengths of 5 and 15 cm.

2.4. Rate Equation in Optical Breakdown

Excitation is not the only process involved in optical breakdown since different types of losses can be involved as well. Generally, optical breakdown may be established when the rate of ionization ▮ in the avalanche ionization process greatly exceeds the rate of losses. The main loss mechanisms in the optical breakdown are diffusion, attachment, and recombination loss.

The electron-ion collision frequency can be neglected compared to the electron-neutral collision frequency due to the small ionization rate in atmospheric pressure.

Loschmidt's number (n_0) is the number of particles (atoms or molecules) of an ideal gas in a given volume (the number density), ▮. Based on Loschmidt's number, the density of neutral gas molecules at atmospheric pressure is on the order of ▮ m^{-3}, which means that the density saturation limit of atmospheric pressure LIP is high enough for electromagnetic waves to be absorbed by plasma, thereby increasing the plasma density. In general, in atmospheric

10

pressure plasmas (APP), electrons undergo several collisions with other particles and ambient gas molecules. Collisions damp the particles' trajectory and energy rapidly.

The continuity equation governs the rate of growth of electron density [33]:

$$\frac{\partial n}{\partial t} = \sum_{M} w_{M} n^{k_M} + (\nu_i - \nu_a)n + D\nabla^2 n - \alpha n^2 - \beta n^3 \tag{2.4}$$

where $\sum_{M} w_{M} n^{k_M}$ is the MPI rate of various molecular species (in inverse seconds), n=n(r,t) is the number density of electrons (in cm^{-3}), ν_i is the ionization rate which is dependent on the applied electric field (attachments/cm^3·sec/initial electron), ν_a is the attachment rate (attachments/cm^3·s/electron), D is the diffusion coefficient (cm^2/s), α is the recombination coefficient ($1/cm^3$-s), and β is the effective radiative recombination rate coefficient for three-body collisions, which will not seriously affect the breakdown threshold. Terms $D\nabla^2 n$ represent electron diffusion and ∇^2 can be approximated by $-1/\Lambda^2$, where Λ is the diffusion length ($\sqrt{D\nu} = \frac{\pi}{\Lambda^2}$) [30] of the breakdown region. The diffusion equation can be rewritten as:

$$\frac{\partial n}{\partial t} = (\nu_i - \nu_a)n + \frac{D}{\Lambda^2}n - \alpha n^2 \tag{2.5}$$

where $D = kT_e/m_e\nu_m$ and ν_m is the electron-molecule effective-collision frequency, given by

$$\nu_m = n_m \sqrt{3kT_e/m_e}. \tag{2.6}$$

ν_i, ν_a, and D are independent of time and the continuity equation can be solved with initial electron density at t=0 to yield

$$n = n_0 \exp\left[\left(\nu_i - \nu_a - \frac{D}{\Lambda^2}\right)t\right] \tag{2.7}$$

Thus, if $\nu_i > (\nu_a + \alpha)$ the electron density will increase exponentially and breakdown occurs.

11

2.5. Breakdown Mechanism

2.5.1. The Pre-ionization Stage

In the preionization phase of LIPs, MPI and inverse bremsstrahlung are the main ionization processes. Electrons can increase their energy through the inverse bremsstrahlung process and through the absorption of laser quantum energy (through three-body elastic collisions). This phenomenon continues until electrons are able to ionize a molecule and create free secondary electrons. However, during the increasing phase of electron density, this process is in competition with loss processes, such as recombination, attachment, and diffusion. If the ionization rate is greater than the loss rate, preionization electrons can ionize more electrons through elastic and inelastic collisions. The onset of the first set of electrons in the focal volume cannot be produced by a direct photoelectric process because the ionization potential (U_i) of the atoms of the gas is greater than the photon energy [33]. Because of the intense laser radiation, an atom with ionization potential energy greater than the photon energy can be ionized by multiphoton absorption. It was reported that the photon energy of a 193 nm laser beam is 6.42 eV, requiring approximately 3 photons to be absorbed within a photon excitation lifetime of 4.1×10^{-16} s for ionization of air (15.6 eV) [29]. This process contains the simultaneous absorption of S photons with energy $h\nu_{las}$ by a molecule whose ionization potential is U_i.

Multiphoton absorption, featured by the MPI frequency ν_S, can occur in those gas impurities that have an ionization energy lower than that of the gas molecules. For pressures greater than 0.98 atm, other ionization processes should be involved beside the MPI process. Free electrons can absorb photon energies by interacting with an electromagnetic field in the presence of a third body, such as a molecule or an ion [26-33]. This is the inverse bremsstrahlung process. The electron requires a certain amount of inverse bremsstrahlung absorption to obtain sufficient energy to ionize a molecule.

We can consider two electron populations:

A) Electrons that received sufficient energy through the inverse bremsstrahlung process to ionize a molecule.

B) Electrons that need to acquire energy to ionize a molecule. The creation of secondary electrons is defined by the following electron-neutral ionization frequency

$$\nu_{coll} = n_{gas} \, v_e \, \sigma_e = N_{ic} \, \sigma_e \sqrt{K_B T / m_e} \tag{2.8}$$

where σ_e is the electron-neutral collision cross section, $N_{ic} = 10^{19} \times 760 \times 1.013 \times 10^5 / T_g$ is the neutral gas molecule density, K_B is Boltzmann's constant ($1.38 \times 10^{-23}\ J/K$), T is the electron temperature, T_g is the gas temperature, m_e is the electron mass, v_e is the electron mean velocity that can be assumed to be $1.8 \times 10^8\ cm/s$ [34], and n_g is the electron cross section which is given by Veyrie [34] as $n_g = 2 \times 10^{-16}$ cm^{-3}.

By assuming a linear approximation for $\sigma_i(T_e)$ and a Maxwellian distribution for the velocities, Veyrie [22] gives an expression for the ionization frequency as a function of electron temperature T_e

$$\sigma_i(T_e) = 24 n_e \times \frac{10^{-16} n_e}{(8\pi m)^2} (K T_e)^{1/2} (U_i + 2 K T_e) \exp\left(-\frac{U_i}{K T_e}\right) \tag{2.9}$$

with U_i being the ionization potential of the gas ($U_i = 15.6$ eV for atmospheric air). Since the laser plasma is produced in air with dominant molecular species of N_2 and O_2, the ionization potential is a mean balance of the ionization potentials of N_2 and O_2, respectively.

Loss processes occur during the rise of the electron density. Negative ions are created because of the recombination of electrons into neutral species, which is an important process for an electronegative gas. Thus, electron recombination into a molecule produces a negative ion and leads to a decrease in the number of free electrons in the ionized gas. Thus, air acts like an electronegative gas. Another loss mechanism is attachment losses, which consist of two main parts: dissociative attachment and three-body attachment. Eventually, we can define the attachment frequency ν_a as $\nu_a = h_a \nu_{coll}$, where h_a is the mean attachment coefficient ($h_a = 1.5 \times 10{-4}\ s^{-1}$) [28] and ν_{coll} is the electron– neutral collision frequency given by $\nu_{coll} = n_g \sigma_e v_e$.

2.5.2. The Heating and Expansion Stage

In the pre-ionization stage, the electron density generated by MPI is fairly low and the resultant plasma is cold and does not absorb laser flux efficiently. Thus, the process is just localized in the focal region. The optical breakdown of air at atmospheric pressure is usually achieved by

13

MPI if the initial electron density is 10^{13} cm^{-3} during the rising phase of the laser pulse. Meanwhile, after reaching the threshold electron density, breakdown develops beyond the focal region by CCI and the medium becomes highly absorptive of the flux and heated very quickly (in the range of 10^{6} K) and a luminous plasma will be observed [17],[29]. This detonation wave undergoes flux irradiation in a conical zone and it is the absorption of this flux in a layer that will govern the plasma expansion until the end of the laser pulse. Many wave propagation processes are postulated to explain the expansion and heating stage [30].

2.5.3. The Post-Ionization Phase

During the end of the laser pulse, the laser plasma is still at a high temperature ~10^{5} K due to continuous absorption of laser energy and keeps expanding like a Taylor detonation wave as described by Zeldovich [35]. The atmosphere near the plasma focal region is heated, thereby allowing gas that was transparent to the laser pulse and cold to begin absorbing the laser radiation. Once the critical number of electrons is liberated, the ion-electron collision process is dominant and plasma starts expanding to the surrounding atmosphere. By creating the absorbing gas layer, the plasma changes from a weakly ionized gas to a fully developed propagating absorption wave in air. The plasma absorbs most of the energy from laser pulse so that further interaction with the laser irradiation is shielded. The absorption wave propagates toward the laser beam until the irradiation is less than the breakdown threshold of air.

Although, the initial energy is released into conical or elongated plasma, the plasma takes on a spherical shape in due course of time [20]. Figure 2.4 shows the interaction between a propagating plasma and ambient gas [9].
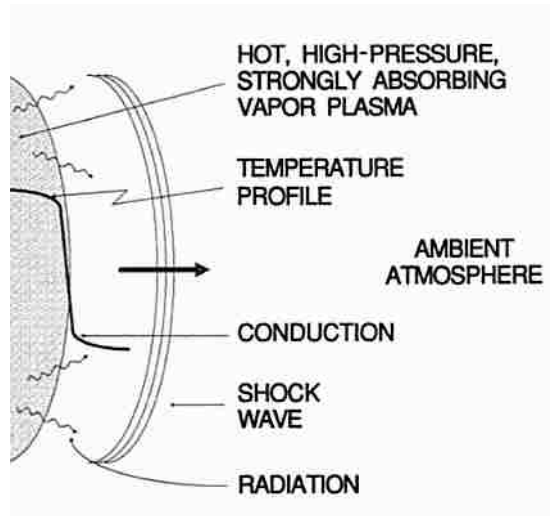
Figure 2.4. Interaction between a propagating plasma and ambient gas [9].

For efficient coupling of electromagnetic waves with laser plasma, the lifetime of the plasma is a useful factor to determine the amount of microwave power that is required to increase or sustain the size of the plasma. The plasma lifetime τ is the time for the initial plasma density n_0 to decrease by a factor 1/e. Estimation of plasma lifetime in atmospheric pressure has been postulated using different models based on loss processes of air as a function of altitude (pressure) and electron density [25]. Due to the high concentration of oxygen in high pressure air in atmospheric plasmas, three-body attachment with oxygen dominates the loss process, which is proportional to the oxygen concentration. On the other hand, for lower air pressures, the concentration of oxygen is less and two-body attachment will be dominant. In laboratory plasmas with electron density of $10^{19} \, cm^{-3}$ and pressure of 1 atm, the plasma lifetime is measured to be approximately 10 ns. Also, by decreasing the surrounding pressure and oxygen concentration, the plasma lifetime will increase by two orders of magnitude in atmospheric pressure.

Due to the fact that three-body attachment is dominant in atmospheric pressure, the continuity equation can be rewritten as:

$$\frac{\partial n(r,t)}{\partial t} = \nu(t) n(r,t) - \alpha n(r,t)^2$$ (2.10)

and the total number of electron in the focal region can be derived as

$$n(t) = n_0 n(r) \exp\left[\int_{t_0}^{t'} v(t') dt' \cdots \left(v \int_{t_0}^{t'} n(t') dt'\right)\right] \tag{2.11}$$

$$n(t) = \exp\left(v \int_{t_0}^{t'} n(t') dt'\right) = n_0 4 \pi^2 d^2 \exp\left[\int_{t_0}^{t'} v(t') dt'\right]. \tag{2.12}$$
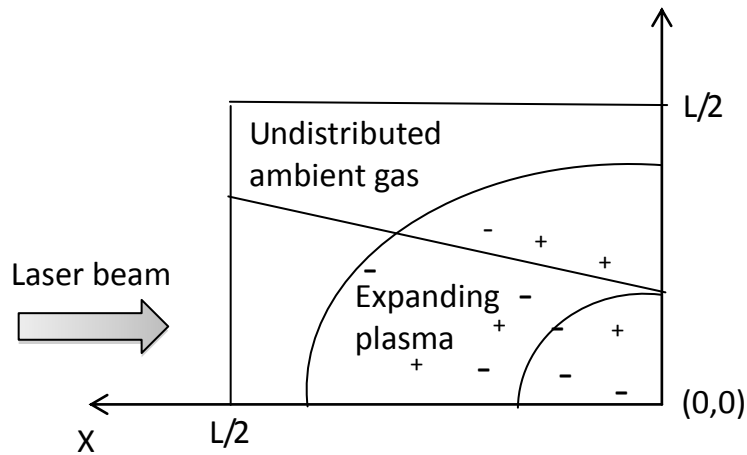
Figure 2.5. Diagram of a quarter of the calculation domain.

For a parabolic pulse with duration $2t_0$, the total number of electrons is

$$n(2t_0) = n_0 4 \pi^2 d^2 \exp\left[2v(2t_0) \cdots \left(v\right)\right]. \tag{2.13}$$

The lifetime of air plasmas as a function of pressure based on Vidmar's experiments [36] is shown in Fig. 2.6.
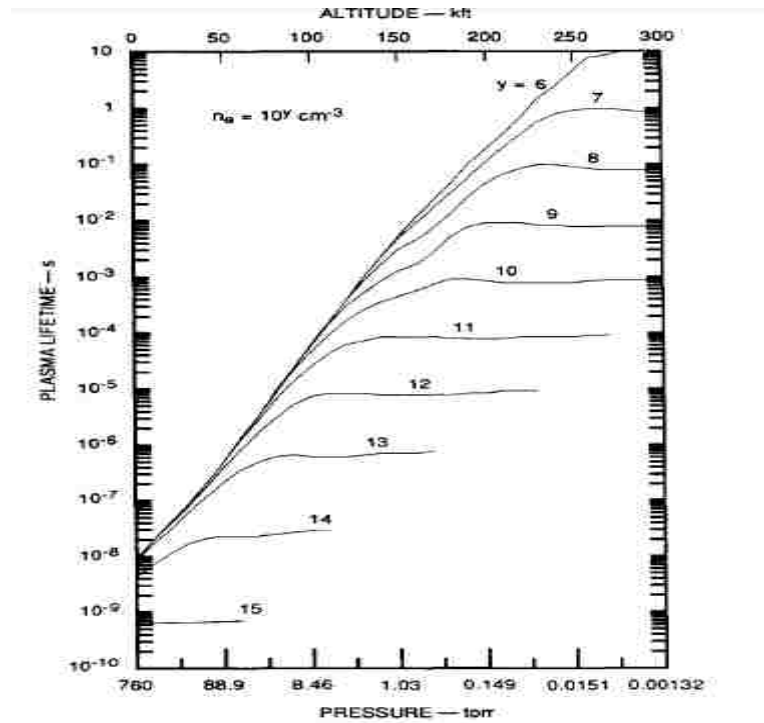
Figure 2.6. Plasma lifetime as a function of pressure for different electron densities [25].

2.6 Simulation Results

2-D MATLAB simulations of the temporal and spatial evolution of the LIP are developed for analysis. The Nd:YAG laser power density distribution can be approximated as a Gaussian. A Gaussian power density distribution in the x-y plane is defined by:

$$I(x,y) = \frac{8P}{\pi d^2} \exp\left[-\left(\frac{2\sqrt{2}}{d}\right)(x^2 + y^2)\right] \tag{2.14}$$

where P [W] is the laser power and d [m] the diameter of the power density distribution.

The spatial power distribution of Nd:YAG laser, SLII-10, with pulse duration 7 ns and energy 600 mJ can be seen in Fig. 2.7.
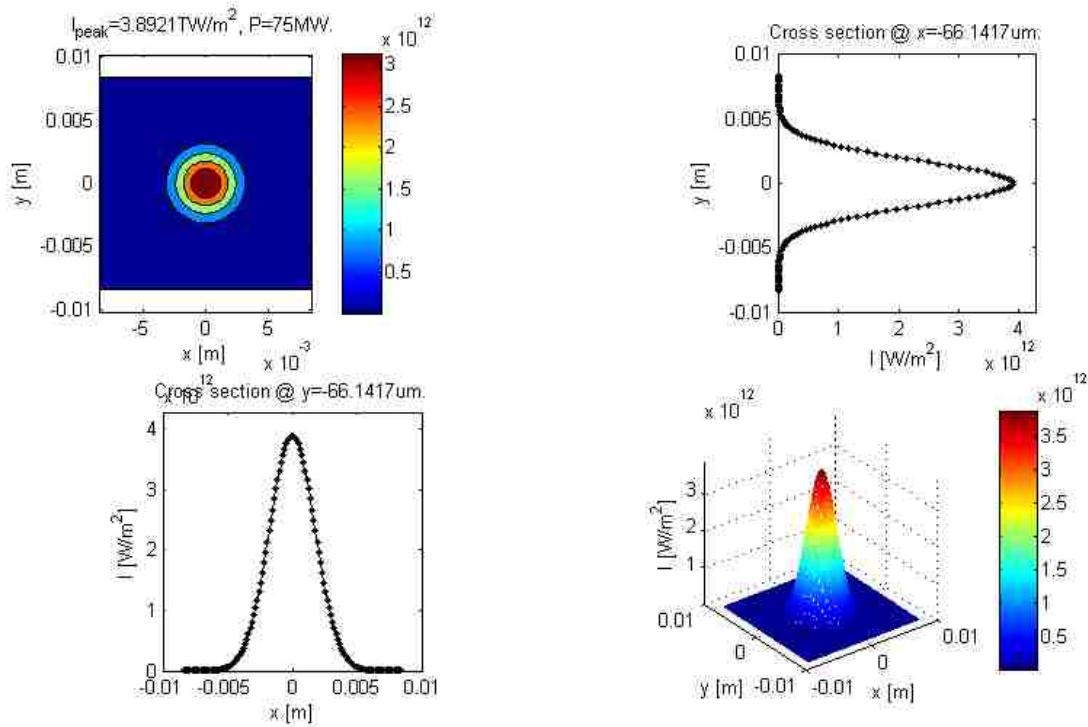
Figure 2.7. Laser intensity distribution along axis of propagation before focusing.

This structure holds data related to a power density distribution $I(x, y)$ [W/m^2] (measured or calculated) at a specified plane along the axis z of propagation of the laser beam before focusing.

We used a standard method, ISO11146, which governs the test methods for beam divergence angles and beam propagation ratios. Figure 2.8 plots the beam dimensions (width, length, and diameter) of the laser beam structure along the optical axis z. We specified all beam parameters in 15 different planes.
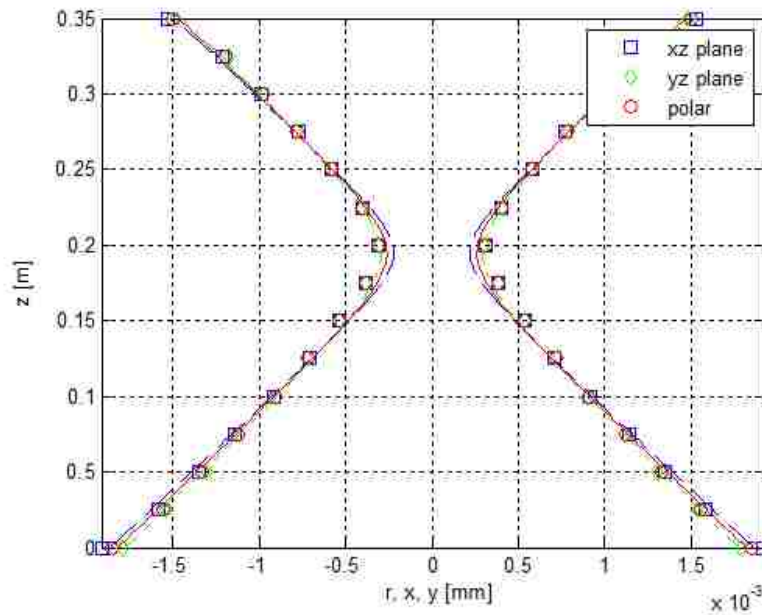
Figure 2.8. Focused laser profile.

Analyzed beam propagation parameters are summarized in Table 2.1.

Table 2.1. Laser beam parameters.

	Focus diameter (μm)	Focus location (cm)	Divergence angle (mrad)	Rayleigh length (μm)
Polar coordinate	0.52192	19.431	0.5	40.06
XZ-plane	0.4412	19.387	0.5	40.06
YZ-plane	0.59159	19.471	0.5	41.5

By assuming a semi-infinite substrate air with constant parameters and a line source of heat of P [W] at the focal point, the line source will induce the following 2D temperature (rise) in the substrate when it is moving at a constant velocity of v [m/s] in the z-direction relative to the surface [27], [29]

19

$$T'(x,y,z,t) = \frac{1}{4\pi K\sqrt{x^2+y^2+z^2}}e^{\dots}\tag{2.15}$$

where K denotes the thermal conductivity [W/(m-K)] and κ the thermal diffusivity [m^2/s] of air. More accurate results can be simulated by assuming a surface heat source (absorbed laser energy) defined by power density I(x,y) [W/m^2] moving over the air surface at the focal point. This surface of air (x-y plane) heat source will induce the following profile of temperature (rise) on the surface when it is moving at a constant velocity of v [m/s] in the z-direction relative to the surface of air [27]

$$T'(x,y,z,t) = \int\int A I(x',y') W(x,y,z,x',y',v) U(\kappa,t,v)\, dx'\, dy'\tag{2.15}$$

where $R=\sqrt{x^2+y^2+z^2}$, $W(x,y,z,x',y',v) = \frac{1}{4\pi K\sqrt{x^2+y^2+z^2}}e^{\dots}$, and

$$U(\kappa,t,v) = \dots\int_0^\infty \dots \exp\left[-\dots\left((\kappa t^2 - \tfrac{D}{2})^2\right)\right] d\kappa\tag{2.16}$$

This expression can be evaluated numerically by using the Fast Fourier Transform (FFT). For simplicity the steady state situation $t > t_0$, so $U = 1$, is considered (see Appendix 1). Figure 2.9 plots the temperature evolution in three different times around the focal region space. The maximum temperature is calculated to be few eV in the focal region. As we expected, the temperature profile propagates towards the laser source. The MATLAB code is reliable for just the first few nanoseconds of laser plasma evolution.
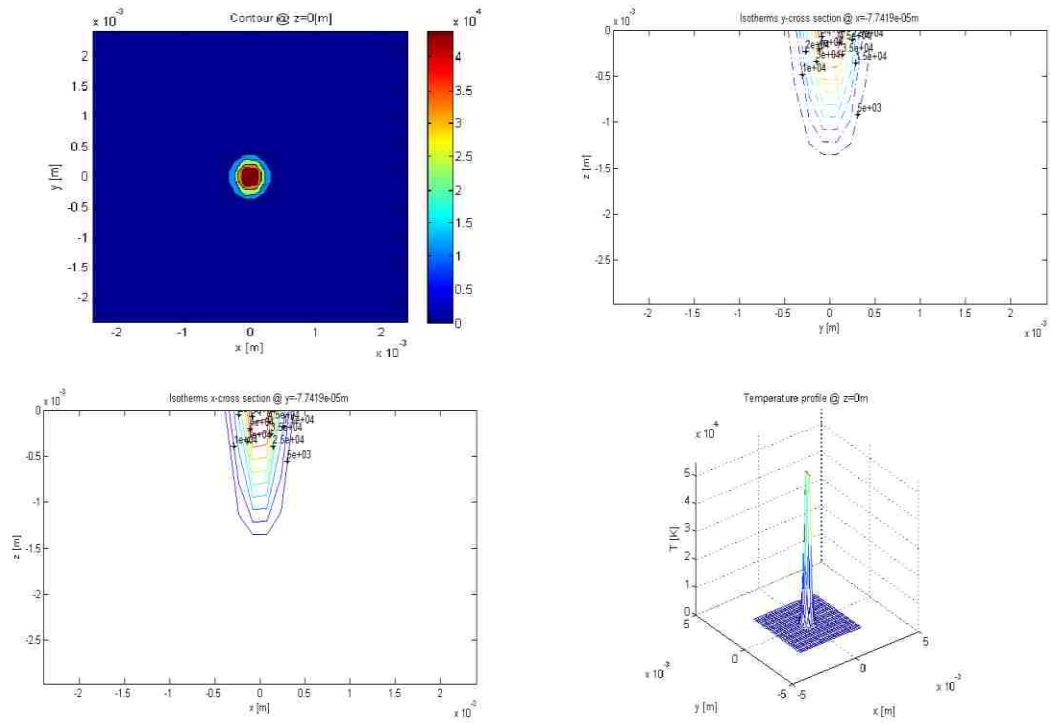
Figure 2.9. (a). Temperature distribution at time t=4 ns.
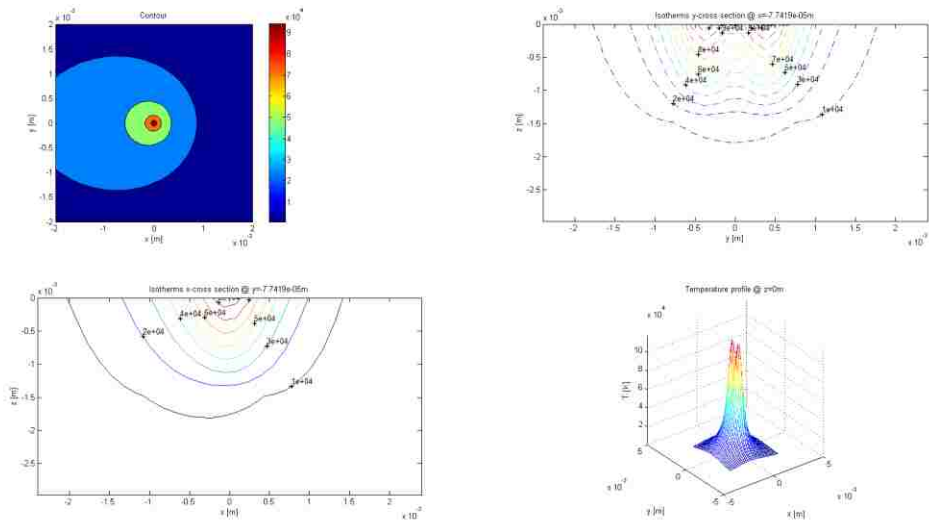
Figure 2.9. (b). Temperature distribution at time t=10 ns.
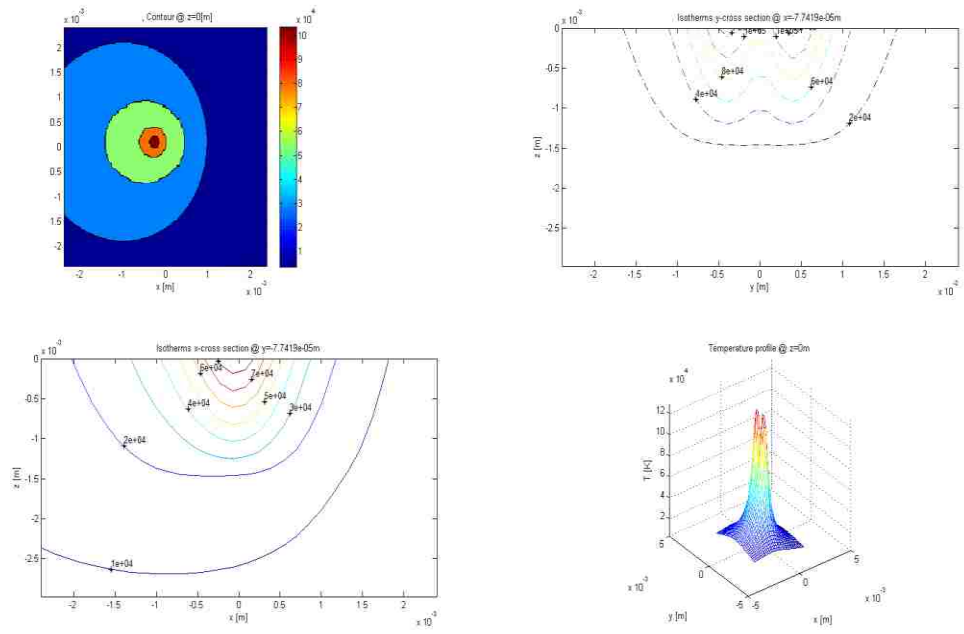
Figure 2.9. (c). Temperature distribution at time t=17 ns

CHAPTER 3

OPTICAL BREAKDOWN THEORY

3.1. Breakdown Threshold

Generally, the breakdown threshold is the lowest irradiance (or power density) at the focal point at which the absorption of energy from the laser pulses undergoes significant change. Based on the ambient gas pressure, type of laser, laser irradiance, beam waist size, pulselength, repetition rate of laser, and dynamics of loss mechanisms, detailed descriptions of the optical breakdown can be postulated. The breakdown threshold is measured and analyzed by two methods: the classical model [29] and the quantum mechanical mode [9]. The classical theory is based on HPM breakdown theory which was investigated experimentally by MacDonald [29]. In order to extend the laser-induced air breakdown process to HPM breakdown where only the CCI approach is taken into account, the effects of MPI need to be quantified and analyzed. In the collisional avalanche ionization based on microwave breakdown theory, when a gas is subjected to an intense oscillating electric field, electrons can gain sufficient energy to ionize neutral molecules and the electron velocity distribution function changes relative to a Maxwellian distribution. The theoretical air breakdown threshold for a 1064 nm pulsed laser is categorized into MPI threshold intensity (W/cm^2) for corresponding photon excitation lifetime $(\tau_{18 h/s} = 3.1 \times 10^{-02} s)$ and CCI threshold intensity (W/cm^2). The quantum mechanical breakdown approach can also be used for optical frequency phenomenon. The estimates show that using two approaches can give us good results for the breakdown thresholds.

3.2. MPI Theory

Nelson conducted some experiments to propose expressions for the breakdown threshold based on MPI [24,31]. When the electron ionization potential is less than the energy of a photon, $W_i \gtrsim \hbar\omega$, two types of field ionizations can be proposed: MPI and tunneling ionization. These ionizations are usually applicable to gases at optical frequencies. MPI occurs when an electron absorbs multiple photons and rises from the ground state to an ionization state. Tunneling ionization occurs when the laser field changes the Coulomb potential of the atoms and the conduction bands so electrons can tunnel through the potential barriers. When the laser pulselength is short or the field is weak, the electron is unable to tunnel through the potential barriers within an optical period; the dominant field ionization is MPI. Figure 3.1 describes both tunneling ionization and MPI.
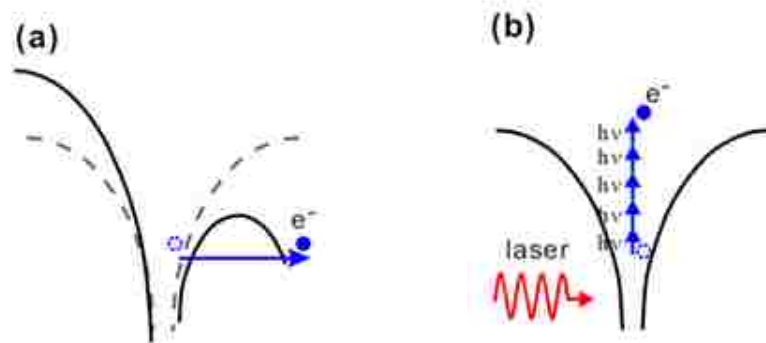
Figure 3.1. (a) Tunneling ionization, and (b) MPI.

Keldysh proposed parameter γ_k [30] that is used to determine the type of the ionization model under given conditions [32]

$$\gamma_k = \frac{\omega\sqrt{2m_e W_i}}{eE}$$

(3.1)

where tunneling ionization dominates when $\gamma_k \ll 1$ and MPI plays the significant role in the first stages of a breakdown. W_i is the ionization potential, E is the applied electric field, and ω is the angular frequency of applied electric field. The ionization potential of N_2 is $W_i = 15.576$ eV, and for

24

the laser intensity in the atmospheric filament with $I \sim 10^{11} \; W/cm^2$ and $\lambda = 1064$ nm, $\gamma_k = 2.7$. Therefore, MPI dominates over tunneling ionization. The MPI rate is modeled by

$$W = \sigma^N n_0 I^N (r, \omega, R).$$ (3.2)

As discussed earlier, the ionization threshold of air ($U_i = 15.6 \; eV$) can be calculated by averaging the ionization thresholds of oxygen, nitrogen, and argon. The photon energy for the 1064 nm laser with pulse duration 7 ns and energy per pulse 600 mJ is $\varepsilon_\gamma = h\nu = 1.167 \; eV$ requiring approximately 14 photons ($N = \frac{U_i}{\varepsilon_\gamma} = \frac{15.6 \; eV}{1.167 \; eV} = 14$ photons) to be absorbed in a quantum lifetime $\tau = \frac{\hbar}{\varepsilon_\gamma} = 5.1 \times 10^{-16}$ s for ionization of air. Thus, a $1.167 \; eV$ photon energy air molecule requires N=14 photons to be ionized in the excitation time. The total number of photon per pulse is 3.1×10^{17}, which means if the laser is focused, the breakdown initiation is very quick. At the beginning of the ionization process, the electrons are created inside the focal volume. The focal region can be approximated as a cylindrical shape with the radius [25]

$$r_b = \frac{f(\theta_{div})}{2}$$ (3.3)

and axial focal length

$$l_b = \frac{(\sqrt{2} - 1) f^2 (\theta_{div})}{2 r_k}$$ (3.4)

where f is the focal length of the lens, r_k is the laser beam radius at the half peak irradiance, and θ_{div} is beam divergence ($\theta_{div} = 0.5$ mrad for Surlite SLII-20). Therefore the focal volume, V_b is

$$V_b = \frac{\pi}{8} \frac{f^2 (\theta_{div})^3}{r_k} (\sqrt{2} - 1).$$ (3.5)
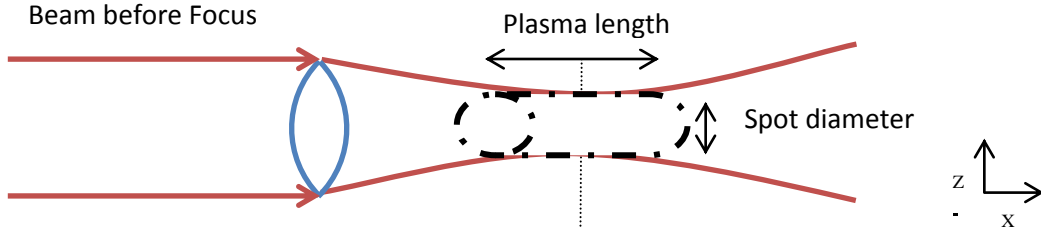
Figure 3.2. Focused laser beam.

For an LIP, the focal spot size can be obtained by using the 1064 nm Q-switched laser and optical parameters. Using a quartz lens with f-number of 20 cm, we can calculate r_f = 50 μm and z_f =82.8 μm. Thus, by knowing the focal volume, we can calculate the characteristic diffusion length of Λ = 12 μm. The ionization threshold is given by the following equation [29]:

$$I_{th} = hN\nu\, W_{th} \tag{3.6}$$

where $W_{th} = \lambda\nu\, N_{th}$ is the interaction threshold in terms of flux density

$$W_{th} = 2C(2\omega)^{1/2}\times 137\times\left(\frac{1}{\omega}\right)^{N} \tag{3.7}$$

C is a constant, 137 is a factor related to the strength of electromagnetic radiation, and N is the MPI coefficient, which is the ratio of the ionization potential of air (15.6 eV for air) to the photon energy ε_ν. Thus, the breakdown threshold intensity value for atmospheric air at 1064 nm is $I_{th} = 1.27\times 10^{11}\ W/cm^2$. The intensity threshold has been checked by different experiments [26,33].

The RMS breakdown electric field is given by [32]

$$E_{rms} = 1.94\times 10^2\sqrt{I_{th}\times 10^{-4}}\ \frac{V}{cm} \tag{3.8}$$

where $E_{rms} = 6.9\times 10^6\ V/cm$. The MPI breakdown threshold intensity is important at lower pressures in the early stages of the initiation of plasma by high power pulsed lasers.

The loss mechanisms, recombination and diffusion, do not have effective impact during the breakdown initiation phase, and so they can be neglected. Bunkin and Fedorov proposed the multiphoton absorption process characterized by the inverse bremsstrahlung coefficients K and K_s [34]. For molecular gases like air, the inelastic collision cross-section is large and there are many

electrons with low energy stage. Thus, the electrons' distribution can be approximated as a Maxwellian distribution at a single temperature.

According to [34] the following expression can be written for the energy absorbed by plasma

$$(K + K_e)I = \frac{d}{dt}\left[n_e\left(\frac{3}{2}kT_e + \epsilon_i\right)\right] \tag{3.9}$$

where

$$K = 3.7 \times 10^5 n_e^2 \left[1 - \exp(-\hbar\omega_0/kT_e)\right]\exp(I/I_c), \tag{3.10}$$

$$K_e = \frac{m_e \hbar\omega}{I_c} \sigma_{ei} \tag{3.11}$$

and $I_c = I_0 c/n_e$ is the multiphoton interaction threshold for an inverse bremsstrahlung process.

In order to determine the electron density variation, $n_e(t)$, and the electron temperature variation, $T_e(t)$, it is possible to solve the following set of partial differential equations

$$\frac{\partial n(r,t)}{\partial t} = (v - v_a)n - D\partial^2 n(r,t)/\partial x^2 - \alpha n^2 \tag{3.12}$$

$$(K + K_e)I = \frac{d}{dt}\left[n_e\left(\frac{3}{2}kT_e + \epsilon_i\right)\right] \tag{3.13}$$

To solve these we need to introduce boundary conditions: the first boundary condition can be $T_e=300K$, $n_e=0$ and $I=I_s$ at time $t=0$. To find another boundary condition, we have to use a condition corresponding to the time τ_s, where the absorption of the laser flux becomes great. Based on the intensity threshold of the MPI process, the MPI phase becomes great with the increasing part of the laser pulse, more specially at $\tau_s = 1$ ns for $f= 5$ cm and $\tau_s =3$ ns for $f=15$ cm.

The Crank-Nicolson method, a numerically stable finite difference method, can be used to solve these partial differential equations.

Figure 3.3 depicts the time variation of the electron density in the focal volume at different pressures. The results are no longer valid after $\tau_s = 3$ ns since the plasma will have propagated out of the focal volume and we will have to use an MHD code to describe this phase of the expansion. When the surrounding pressure increases, the preionization phase also increases. At time $\tau_s = 1$ ns, we obtain an electron density on the order of 10^{18} m^{-3} and electron temperature 10^4 K.
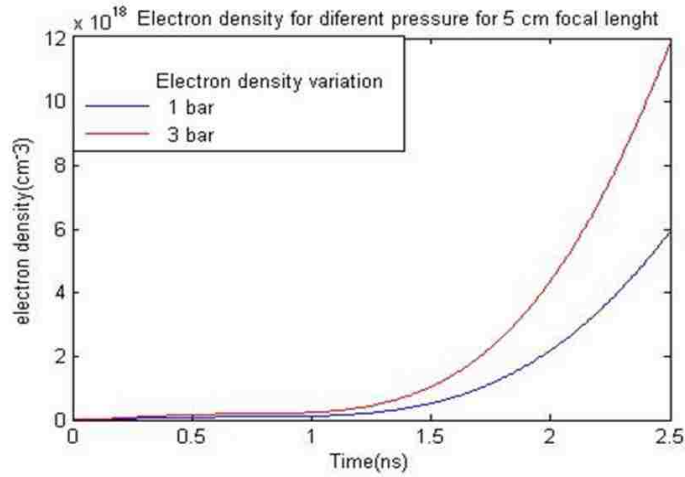
Figure 3.3. Electron density variation for different pressures at f=5 cm.

3.3. Collisional Cascade Ionization Theory

The theory of CCI was first developed for microwave frequencies by MacDonald [29] and has been extended to LIPs by different authors [35],[36]. In the CCI process, free initial electrons produced by the MPI process gain more energy from the laser pulse upon elastic and inelastic collisions by neutral atoms. If the energy is greater than the ionization potential of air, electrons can produce secondary electrons due to elastic and inelastic collisions. In and of itself the breakdown phenomenon implies a rapid exponential rise in the electron density and as a result the electron distribution function can be strongly affected. The criterion that differentiates between the two main mechanisms is the electron-ion collision, which is given by [37],[38]

(3.14)

where N_i is the ion density, T_e is the electron temperature, $U_p = e^2 E^2/4m\omega^2$ (W/cm^2), and $\ln\Lambda_{ie}$ is the coulomb logarithm for the electron-ion collisions. At laser wavelength λ=1064 nm and for a typical filament in air, Z=1, $N_i \sim 10^{16}$ cm^{-3}, $I \sim 5\times 10^{13}$ W/cm^2, $U_p K_{in} > T_e$, $\ln\Lambda_{ie} \sim 10$, the characteristic collision interval is $1/\nu_{ie}$ ~0.5 ns. This is much smaller than the pulse duration (7 ns) of a typical Q-switched Nd:YAG laser, and in this case CCI is more important than MPI. Generally, at low frequencies ($\omega \ll \nu_m$) air can breakdown with RMS electric field [9]

$$E_b = \left[30 \frac{V}{cm}\right] \times \left[air\ pressure\ (mmHg)\right]. \tag{3.15}$$

If the applied frequency is sufficiently low, breakdown can occur during a fraction of the RF cycle and it is in agreement with the Paschen curve breakdown threshold,

$$U_{br} = \frac{A p d}{\ln\left[\frac{B p d}{\ln\left(1+\frac{1}{\gamma}\right)}\right]} \tag{3.16}$$

where U_b is the breakdown intensity threshold, A and B are constants for a given gas and γ is a slow varying function of E/P over a wide range. At higher frequencies ($\omega \ll \nu_m$) E_b scales linearly as

$$E_b = 1.94 \times 10^4 \|I\|^{\frac{1}{2}} \quad \text{V/m}, \tag{3.17}$$

where I is expressed in MW/cm^2. In the early stages of ionization due to increasing laser intensity, the loss mechanism such as diffusion and attachment losses can also be neglected.

Based on Kroll and Watson [9], MacDonald [29], and Scharfman and Morita [39], at microwave frequencies and low pressures, the threshold power density for CCI can be written as

$$U_{MCI} = 1.44 \times 10^6 \|P^2\| + 3.3 \times 10^9 \times I^2 \quad \text{W/cm}^2, \tag{3.18}$$

where P (atm) is ambient pressure.

Although this theory is proposed based on microwave frequencies and pressures below atmospheric pressure, it is possible to scale it to higher wavelengths and pressures because the breakdown power overestimates the threshold by one order of magnitude [17],[30]. The CCI theory shows that a breakdown power flux threshold value for 1.0 μm laser pulse is $P_{b(CCI)} = 7.37 \times 10^{11}$ W/cm^2 and the rms breakdown electric field is $E_b = 1.94 \times 10^{-4} |P_{b(CCI)}|^{\frac{1}{2}} = 1.026 \times 10^8$ V/m. It is obvious that the MPI breakdown threshold is higher than the CCI breakdown threshold because MPI provides free electrons to initiate CCI. The classical and quantum mechanical approaches for predicting the breakdown threshold intensities yield similar results.

Figure 3.4 shows the classical breakdown threshold versus wavelength for different laser pulses at 1 atmospheric pressure (solid line) and low pressure breakdown threshold which is proposed by Morgan (dashed line) [40]. Morgan calculated the irradiance breakdown threshold for triangular laser pulse with duration of t_M at low pressures without assuming the diffusion and recombination losses to be

$$I_{th} = n_0 / \delta \left(\frac{c}{v_{osc}}\right)^2 \frac{1}{\tau K} \ln(1_n V_i n_{e,t}), \tag{3.19}$$

where δ is a constant that depends on the constitutive properties of air, n_n is the gas density, and $\alpha_{io} = n_{io} / n_n$ is the degree of ionization.
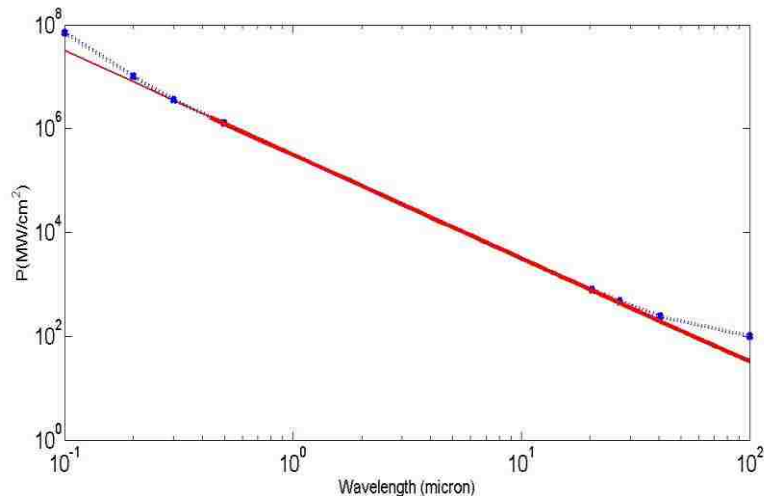
Figure 3.4. Laser breakdown power thresholds for air at 1 atm versus laser wavelength.

Experimental results for air at different breakdown volumes verify the correctness of the theoretical model [41]. It was found that, for all gases examined, as in the theory, the threshold power density increases as the focal volume increases and decreases as the pressure increases.

The CCI theory predicts that the threshold decreases as the pressure increases and, after passing a minimum, increases with increasing pressure (Paschen curve). However, the MPI theory predicts that the threshold is almost independent of the gas pressure.

For the rare gases in the range below atmospheric pressure it is found that the relation between the laser pulse duration and the plasma growth time is the primary factor which determines the breakdown threshold.

3.4. Loss Mechanisms

The recombination and diffusion losses are the main loss mechanisms for a LIP.

3.4.1. Recombination Loss

The process in which the atomic system goes from an initially charged state to a neutral state of lower energy is recombination mechanism and can proceed by two body or three body interactions. In this process, electrons collide with ions and form an excited neutral atom, $M^+ + e^- = M^* + h\nu$. To determine the breakdown threshold accounting for the pulse duration and recombination losses, the nonlinear rate equation (diffusion equation) is:

$$\frac{\partial n_e(r,t)}{\partial t} = (\nu_i)n_e(r,t) - \alpha n_e^2(r,t) \tag{3.20}$$

The recombination rate is proportional to ion concentration, which is equal to the electron concentration for neutral plasma. The rate equation can be rewritten in the integral form [22]:

$$n_e(t) = 4\pi \varepsilon^{3/2} m_e \delta^{3/2} \exp\left[\int_{t_0}^t \nu(t')dt' - \alpha \int_{t_0}^t n_e(t')dt'\right] \tag{3.21}$$

31

where $n(t)$ is the total number of electrons in the focal region and $A_{MPI}^{-1} m_0 n_0 S^3$ [25] is the initial electron density from MPI. By assuming that recombination is a small effect, the electron density for a laser pulse with duration τ is

$$n(\tau) = A_{MPI}^{-1} m_0 S^3 \exp(v_c \tau) \times \exp\left[\left| A_{MPI}^{-1} n_0 m_0 S^3 \left(\frac{M \tau}{v_c v_g}\right)^2 \exp(v_c \tau) \right|\right] \quad (3.22)$$

When the density is high, the recombination loss is dominant and density decays reciprocally. Generally, the main ionization mechanisms are photoionization and CCI, while the recombination processes are separated into three categories: the radiative, three-body, and the dielectronic recombination.

- Radiative Recombination:

    This is the main process of recombination:

$$X_Z^+ + ee = X_{Z-1}^+ + h\omega_p \quad (3.23)$$

    where X_Z is the ion charge state Z. The recombination rate $(cm^3 s^{-1})$ can be written as

$$R_{rr} = 1.9 \times 10^{-13} \frac{x^2}{\sqrt{T_e}} \sum_{n=n_{min}}^{\infty} \frac{\beta}{n^3} e^{\beta/n^2} \int_{\beta/n^2}^{\infty} e^{-t} dt_e \quad (3.24)$$

    where $\beta = X^2 E_{ion}/T_e$ and E_{ion} is the hydrogen ionization energy.

- Three Body Recombination:

    This process is the inverse of the CCI process and can be written as

$$X_Z^+ + ee + ee = ee + X_{Z-1}^+ . \quad (3.25)$$

    Its rate coefficient $(cm^3 s^{-1})$ is:

$$R_{3br} = 1.66 \times 10^{-29} \frac{g(z)}{g(z-1)} \frac{1}{T_e^{9/2}} \exp\left[\left| \frac{E_{ion}(z-1)}{T_e} \right|\right] \quad (3.26)$$

    where $g(z)$ is the statistical weight of the ion state Z.

- Dielectronic Recombination:

    This process occurs when an electron recombines with an ion in an excited state and while doing so it excites a second electron. Thus, the ion is left in an excited state, or it may radiatively decay.

3.4.2. Diffusion Loss

When there is a pressure gradient in a gas, there will be a force on the charged particles in a direction opposite to gradient ($-\nabla n$) that causes a flow of charged particles. This flow is called diffusion. When diffusion is the only loss mechanism the equation of continuity becomes

$$\frac{dn_e(r)}{dt} = (\alpha_i - \alpha_a)n_e(r) + \frac{D}{\lambda^2}n_e(r,t). \tag{3.27}$$

If the electron-neutral collision frequency is greater than $1/\tau$ (τ is the laser pulsewidth), we can assume that the solution is time-independent. Using separation of variables, n(r,t)=n(r)y(t), the equation can be rewritten as [22]

$$\alpha_i(r)n_e(r) + \frac{D}{\lambda^2}n_e(r) = \gamma n_e(r). \tag{3.28}$$

$$y(t) = \exp[\gamma(t)t]. \tag{3.29}$$

Writing this equation in cylindrical coordinates we obtain Bessel's equation. The solution to the time-dependent equation is

$$n_e(r,t) = n_e(r)\exp[\int_0^t \gamma(t')dt'], \tag{3.30}$$

where λ is the diffusion length and characterizes the distance over which a charged particle diffuses to be lost from the plasma [25]. This equation can be solved by assuming a cylindrical focal region with radius r, outside which the photon flux density is zero

$$n_e(r, t) = n_{e0}(r) \sin\left(\frac{\pi x}{L}\right) I_0 \left\|\frac{2.405^2 r^2}{M}\right\|$$

(3.31)

     The type of diffusion that results when the electron and ion concentrations are great enough so that electrostatic force between electron and ions can couple them together is called ambipolar diffusion [42]. When the density is low diffusion loss is dominant and the density decays exponentially with time.

Chapter 4

INTERACTION OF A HIGH POWER MICROWAVE WAVE BEAM WITH A NONUNIFORM PLASMA

4.1. Pulsed RF Breakdown

RF waves are electromagnetic radiation and the generation of plasma using them can be described using basic electromagnetic theory. Microwave-generated plasmas are often of particular interest due to their ability to provide a high density of charged particles and active species. Under the strong pulsed RF electric field, electrons gain sufficient energy to overcome the ionization potential, and if there is sufficient ionization, the electron density grows exponentially with ionization rate w_i. The threshold RMS breakdown electric field for low repetition rate pulses in atmospheric pressure is [43]

$$E_{th} = 28.6 \times (\nu_a / \omega) \left(\frac{N_m}{2.7 \times 10^{19} cm^{-3}} \right) \sqrt{\left(1 + \frac{\omega^2}{\nu_a^2} \right)} \ kV \cdot cm^{-1} \tag{4.1}$$

where N_m is the neutral density.

The special focus of this study is on creating an HPM wave beam at a frequency of 10 GHz. A circular waveguide is used to create this signal with spatial distribution of the TM_{01} mode. The spatial electric field distribution of the TM_{01} mode is shown in Fig. 4.1. The electric field has a maximum around the waveguide. The TM_{01} can be converted to a TE_{11} by a mode converter to achieve a higher power density in the center of the wave beam.

In our experiment, the microwave output has a frequency of 10 GHz and pulse duration of 10 ns. The threshold RMS breakdown electric field is about 38 kV/cm and the pressure of the

surrounding air is 631 Torr. The total time-averaged power radiated can be given by the integral of the Poynting vector over the output aperture

$$P = \text{Re} \oint_S \left[\vec{E} \times \vec{H}^* \right] \cdot d\vec{s} \tag{4.2}$$

For the special case when the output aperture is circular and the half angle of the horn is sufficiently small, the higher order modes are evanescent. The horn is multiple wavelengths long to achieve less reflections.
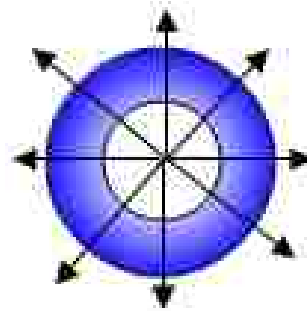
(a)   (b)

Figure 4.1. (a) open-shutter photograph of a plasma ring corresponding to the TM01 mode air breakdown pattern generated by a high-power backward wave oscillator [44]. (b) Spatial variation of electric field in TM01 mode.

With these assumptions, the radial electric field and azimuthal magnetic field for the TM_{01} mode are [44],[45]

$$E_\rho = -\frac{E_m}{\chi_{01}} J_0\left(\frac{\chi_{01}\rho}{R_a}\right) \exp\left(-\frac{j\pi s \rho^2}{R_a^2}\right) \tag{4.3}$$

$$H_\phi = H_0 \chi_{01} \tag{4.4}$$

where $s = R_a^2/(\lambda R_h)$ is the quadratic phase error, R_h is the horn slant height, R_a is the aperture radius, J_0 is the Bessel function of the order zero, and $\frac{\chi_{01}}{R_a}$ is the cutoff wavenumber. With that in mind that the time-averaged power density is

$$P_{avg} = \pi \varepsilon R_a^2 \frac{E_0^2}{\chi_{01}} \left| J_1(\chi_{01}) / J_1\left(\frac{\chi_{01}\rho}{R_a}\right) \right|^2 \tag{4.5}$$

If $\nu_i > \nu_{eff}$, the breakdown will develop exponentially. Generally, as mentioned in Chapter 2, the rise in the ionization is described by the continuity equation for electrons

$$\frac{\partial n_e}{\partial t} = \left(\nu_i - \nu_a - \frac{D}{r^2}\right)n_e \tag{4.6}$$

where ν_a is the effective recombination rate, D_e is the diffusion coefficient, r is the diffusion length, and ν_i is the ionization rate. As long as the diffusion and recombination losses are less than the ionization rate, $\frac{D}{r^2} \ll \nu_i$, the diffusion coefficient for the Maxwellian distribution is approximately ambipolar and given by

$$D_e = 3 \times 10^7 \left(\frac{10^{17}}{N_{gas}}\right)\varepsilon \tag{4.7}$$

where ε is the average electron energy and T is the gas temperature of the gas. Based on the different electron distribution functions, different diffusion coefficients can be obtained. If the mean free path is constant so that $\lambda_m = \lambda_e$ we obtain a different diffusion coefficient using the Druyvesteyn distribution function. The diffusion coefficient from these two distributions (Maxwellian and Druyvesteyn) are similar for the HPM case. Those results are not different from the approximation used by MacDonald [29], Gaskell, and Gittermann [46], which is represented by

$$D = \left(29 + \frac{0.9 N_{ω}}{p}\right)10^5 \quad cm^2 \cdot Torr/sec \tag{4.8}$$

Generally, breakdown occurs when the pulsewidth τ is long enough to make the plasma frequency equal to the wave frequency before the end of the laser pulse. Thus, the breakdown condition for a pulsed RF wave is

$$n(\tau) = n_0 \, e^{\left(\nu_i - \nu_a - \frac{D}{r^2}\right)\tau} \geq n_{cr}, \tag{4.9}$$

where n_0 is the initial electron density and $n_{cr} = \frac{m \omega^2}{4\pi e^2}$ is the density at which the wave frequency ω equals the plasma frequency [47]. The ionization frequency, ν_i increases rapidly with

37

$\frac{W_K^c}{W}$ above the threshold value, whereas $\frac{\nu_a + \nu_d}{\nu}$ varies weakly. This means that, for pulsed systems, we can approximate $\omega_{thresh} \approx \omega_K$:

$$\omega_K > \omega \, \left\| \ln\left(\frac{\nu_{eff}}{\nu_{ei}}\right)\right\| \tag{4.10}$$

The threshold expression can be calculated for single pulse breakdown [47]

$$\frac{E_{eff}}{p} = 18 \left(\frac{\nu_{eff}}{p} \cdot 16\right)^{0.6} \tag{4.11}$$

where the effective electric field is $E_{eff} = E^2/\sqrt{(1+\omega^2/\nu_c^2)}$. Figure 4.2 shows the threshold field for different pulsewidths [17]. The single pulse breakdown condition can join the CW condition as the pulselength increases. When the power is pulsed, breakdown occurs if the electron density reaches the critical value before the end of pulse. Thus, the breakdown threshold field is higher for the CW field. Also, as the pulse repetition rate increases gradually, the threshold field strength for the breakdown decreases until it reaches the CW condition. It is shown that the breakdown condition is unaffected by pulselength when $p\tau > 10^{-3}$ [17].
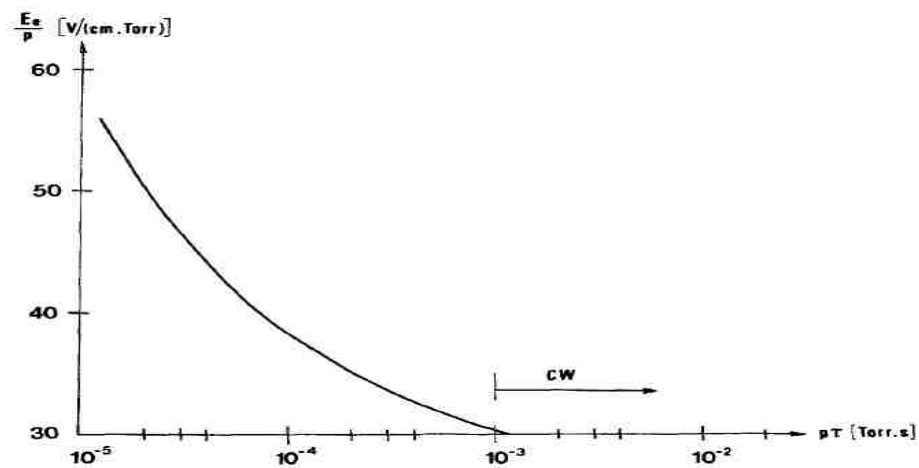
Figure 4.2. Threshold field for single pulse breakdown in constant atmospheric pressure [17].

When free electrons start to oscillate with the oscillating electric field, collisions with neutral particles become more dominant, so these collisions heat up the gas and decrease the

38

threshold intensity. Due to the much larger mobility of the electrons with respect to ions, the electrons are assumed to be responsible for ionization and heating. The electron's equation of motion for the collisional case is

$$m_e \ddot{x} = -eE - \frac{m_e \nu_m (v_e - v_n)}{} \tag{4.12}$$

where $E = E_m \exp(-i\omega t)$ is the applied oscillating electric field. By integrating the equation of motion we obtain the trajectory of the electron as

$$x = -\frac{e E_m}{m_e \omega^2} \exp(-i\omega t) - \frac{\nu_m}{} \int x \, dt \tag{4.13}$$

As obvious, the position of the electron is dependent on time and can be written for the collisionless case as

$$x = -\frac{e E_m}{m_e \omega^2} \exp(-i\omega t). \tag{4.14}$$

The incident electromagnetic radiation can only transfer a specific amount of its energy while it is traveling in the plasma. The remaining energy is transmitted through the plasma or is scattered from the thermal plasma. In order to increase the attenuated power by the collisional plasma, the standing wave can be formed by trapping the electromagnetic wave inside the cavity (i.e., the microwaves) [19].

As a general approximation, each species in the microwave plasma has its own temperature that obeys a Maxwellian distribution. The excitation temperature of electrons T_e and the ionization temperature T_{ion} can be used to specify the atomic excitation and ionization process. The scaling of the various temperatures in the microwave plasma can be given as $T_e > T_{ion} > T_{gas}$ This scaling indicates that the microwave-induced plasma is not in local thermal equilibrium (non-LTE) but for simplicity, the Maxwellian distribution can be used.

4.2. Numerical Results and Discussions

The characteristics of an atmospheric LIP have been studied by different authors. Their investigations show the different interesting characteristics including: high density gradient, lifetime, low electron temperature, unsaturated electron density and highly collisional electrons [9-11],[20]. The required power to maintain the laser plasma in air is fairly high, but an HPM source can assist it to be sustained and developed with the lower power density.

In this study, the atmospheric plasma is generated by using a combination of a laser and an HPM wave beam.

If the ionization process results in a nonuniform electron density, such as a Gaussian profile $N(z,t) = N_{e,exp}\left(\dfrac{z}{l}\right)^2$ or an Epstein profile, the plasma can either reflect or absorb the electromagnetic radiation. In this section we discuss the numerical analysis of the propagation of electromagnetic waves through a LIP and the effects of different plasma parameters on the reflected, absorbed, and transmitted powers.

The density of neutral gas at atmospheric pressure is on the order of $10^{22} - 10^{24}$ m^{-3}, which means that the density saturation limit of the atmospheric pressure LIP is sufficiently high for an electromagnetic wave to be absorbed by the plasma. If a microwave wave beam is directed towards plasma, the electrons are accelerated by the electric field, and the electron density can increase. In general, in atmospheric pressure plasma (APP), electrons undergo several collisions with other particles and ambient gas molecules. Collisions damp particles' trajectories and their energy rapidly increase. The energy of an electromagnetic wave can be coupled into these particles and increase their decay time. The dispersion relation of an electromagnetic wave propagating in the APP with no magnetic field is

$$\omega^2 = \omega_{pe}^2 + c^2 k^2. \tag{4.15}$$

Based on the above equation, an electromagnetic wave can propagate through the unmagnetized plasma and interact with it when the wave frequency ω is greater than the plasma frequency ω_{pe}. The microwave is reflected from the plasma when the electron density is higher than the critical density $n_{cr} = 1.1 \times \dfrac{10^{25}}{\lambda^2}$. Generally, the LIP has the maximum electron density in the range of $10^{18} - 10^{21}$ m^{-3}, so the coupling of a LIP with microwaves is critical and must be studied

for different density gradients. In other words, when $n_e \ll n_c$, the microwave cannot transmit through the plasma and reflects back. In this situation, the electromagnetic wave will turn into a thin evanescent wave on the surface of the plasma. Thus, the plasma frequency is the cut-off frequency and the electron cyclotron frequency is the resonant frequency [22].

As the plasma density falls below the critical density, it rapidly loses its reflective properties. For instance, a plasma with density $n_e = 0.5 n_{crit}$ yields a power reflection coefficient of about 25% [48].

In this study, we tried to propose an analytical investigation for the propagation of a microwave wave beam into laser plasma with a parabolic electron distribution. The effect of absorption, transmission, and reflection of the microwave by an homogenous single slab plasma and an inhomogeneous multiple slab model are discussed below. The whole plasma can be modeled as a three dimensional grid where each grid has a constant electron density n_e. First of all, we discuss the propagation of an electromagnetic wave into one-dimensional single slab plasma with uniform electron density. It is valid as long as the duration of the microwave pulse is less than the time for the plasma to expand. Next, we will be able to perform an analytical investigation of a nonuniform LIP.

Two methods are widely used in the literature. The first one is a method based on the summation of successive reflected and transmitted powers at the plasma interfaces [18], and the second method is related to the scattering matrix method (SMM) [49].

According to the expression, the plasma frequency is $\omega_p = \sqrt{n_e e^2 / m_e \varepsilon_0}$ and can reach a value up to several GHz. When the plasma medium (air) absorbs a significant fraction of electromagnetic energy, a laser supported detonation wave will be formed [50]. Under this condition the axial length of the LIP can be written as

$$ Z = const \left(\frac{(\gamma^2 - 1) \mu \varepsilon_0^2 \omega_0}{\beta \rho_0} \right)^{\frac{2}{3}} \frac{z}{t^2} \tag{4.16} $$

where E_0 is the incident electric field strength, γ is the specific heat ratio, ρ is the density of the ambient gas, β is an absorption factor, and σ is the high frequency conductivity, which is given by $\sigma = e^2 n_e \nu / [m_e (\omega^2 + \nu^2)]$, where ν is the electron collision frequency. For high pressures, we can approximate the length as

$$\chi = const\left(\frac{W K}{p^2}\right)^{?} \frac{?}{?}$$

where W is the total absorbed energy. For better interaction, the plasma dimensions must be comparable to the wavelength of the incoming wave. For better coupling of microwave signal with a LIP, the plasma size must be in the range of millimeters. The dimensions of the LIP are influenced by the electron density, plasma lifetime, temperature, and the pressure of the surrounding gas. It can be increased by different methods such as increasing the laser pulse duration and the energy per pulse of the laser and also by using a lens with a larger focal number.

The host gas (air or a noble gas confined by a membrane) is at ambient atmospheric conditions and under many circumstances has a sufficient heat capacity to cool electrons with little change in the temperature. Thus, air is capable to cool down the LIP rapidly and the lifetime of the plasma in air is very short. By changing the chemistry of the ambient gas (by using a noble gas, as an example), the plasma lifetime can be increased.

The Nd:Yag laser with pulse duration 7 ns and energy 600 mJ can be focused onto air to produce a LIP. This LIP can achieve an irradiance clearly greater than 1 TW$/cm^2$, which exceeds the breakdown threshold of air significantly. In this case, the power density in the focal region is too high. This causes a breakdown before the focal spot and a propagation of the plasma toward the laser beam.
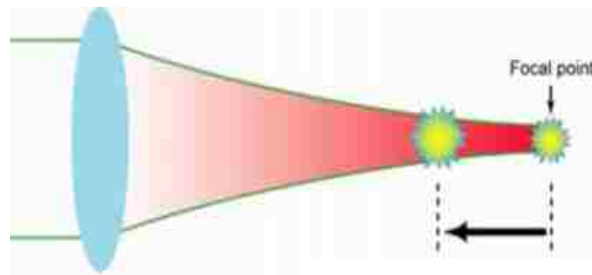
Figure 4.3. Schematic diagram of plasma generation position; as the laser power becomes large, the plasma location will change.

The expansion of the LIP from the focal region creates a density gradient ∇n with approximate scale length $L = V_s \tau$. V_s is the ion acoustic speed and τ is the duration of the expansion. The ion acoustic velocity can be written as

$$v = \int \frac{I \, dt}{\rho_0 \varepsilon} \quad (4.18)$$

For shockwaves or laser-supported radiation waves, the velocity is given by $v = I/\rho_0\varepsilon$, where I is the incident laser intensity, ρ_0 is the mass density of the gas (air), and ε is the internal energy of gas in the specified pressure.
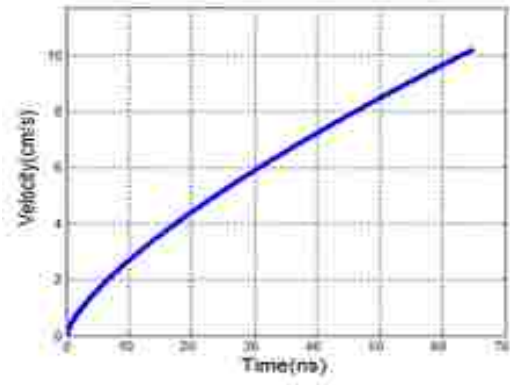
Figure 4.4.The laser shockwave velocity from a laser beam as a function of laser energy.

4.2.1. Electromagnetic Propagation through Uniform Plasma

In the early stages of plasma production, it is shown that the initial density decay time is short in comparison with the time scale of the loss mechanisms diffusion and recombination [51]. For this reason, the boundary of the plasma has a sharp density gradient in comparison to the microwave wavelength. To better understand its interaction with electromagnetic waves, it can be approximated as uniform plasma.

The plasma is assumed to be unmagnetized, lossy, weakly ionized, collisional, homogenous, and the electromagnetic wave is linearly polarized with angular frequency ω and is normally incident onto the plasma slab with an homogenous electron density distribution. As mentioned in Chapter 2, the LIP is also assumed to be cylindrical and homogenous along the focal volume, as show in Fig. 4.5.
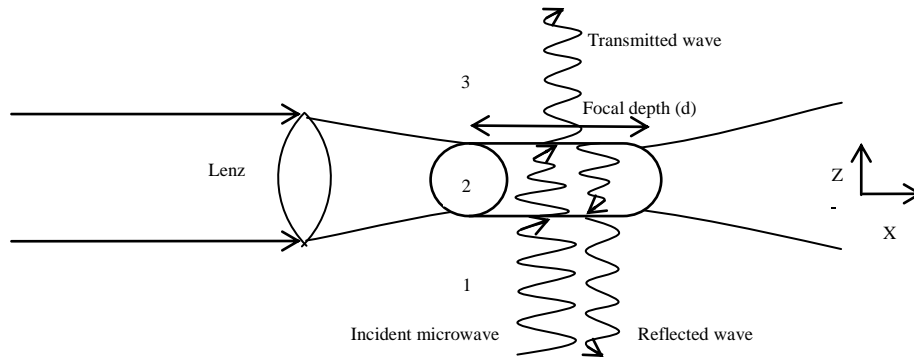
Figure 4.5. Schematic diagram of wave propagation through a uniform plasma.

Some part of the electromagnetic wave is reflected back into region 1, air, and some portion of is transmitted into region 2, the LIP. Due to the air/plasma interfaces, the electromagnetic wave bounces back and forth between the two bounding surfaces. Some portion of the electromagnetic wave is absorbed and some portion is transmitted through regions 1 and 3 (air). The origin of the coordinate is on the bottom surface of the plasma layer.

The unmagnetized, collisional, cold and two dimensional plasma is dispersive with a complex dielectric constant given by

$$\varepsilon_c(\omega) = \varepsilon'_c(\omega) - j\varepsilon''_c = \varepsilon'_c(\omega) - j\,\sigma/\omega\varepsilon_0 \tag{4.19}$$

The electrical conductivity of the plasma σ based on the Buneman equation, can be written as [52]

$$\sigma = \frac{\varepsilon_0 \omega_p^2}{\nu_{eff}(1+\omega^2)} \tag{4.20}$$

where ν_{eff} is the effective resistance of the plasma which can be simplified by neglecting the thermal motion of the electrons and calculated using the Krook operator [52]

$$\nu_{eff} = \frac{\varepsilon_0 m_e}{n_e e^2} \frac{\omega^2}{\frac{j-1}{2}} \tag{4.21}$$

where ω is the frequency of the incoming wave, $\omega_{pe} = \sqrt{\dfrac{N_e e^2}{\varepsilon_0 m_e}}$ is ω_{pe}, $\nu = N_{e0} \sigma \sqrt{\dfrac{8 k_B T}{\pi m_e}}$ is the electron momentum transfer frequency, N_{e0} is the initial electron density, σ is the cross section of the electron elastic collision, k_B is Boltzmann's constant, and T is the electron temperature. With some manipulations, we can obtain the relative permittivity of the plasma based on the Drude-Lorentz model [53]

$$\varepsilon_r(\omega) = Re(\varepsilon_r) + Imag(\varepsilon_r) = 1 - \left(\dfrac{\omega_{pe}^2}{\omega_{coll}^2 + \omega^2} \right) - j \dfrac{\omega_{coll}}{\omega} \left(\dfrac{\omega_{pe}^2}{\omega_{coll}^2 + \omega^2} \right) \tag{4.22}$$

This result is similar to what has been calculated by Appleton [54].

If the plasma is cold and collisionless $\omega_{coll} = 0$, the permittivity expression reduces to the dielectric constant of a collisionless plasma, $\varepsilon_r(\omega) = 1 - \dfrac{\omega_{pe}^2}{\omega^2}$. This dielectric constant is negative in overdense plasma and in the low density plasma goes to the index of refraction of air, a lossless medium. Moreover, since the plasma consists of different free charged particles, its state can be significantly affected by the electromagnetic waves.

It is assumed that the influence of the magnetic field on the charged particles is negligible in comparison to the external electric force. The plasma is in the classical regime with no external magnetic field. The Lorentz force law with linear damping term can be written as

$$F = m_e \dfrac{d^2 r}{dt^2} = F_{Coulomb} + F_f + F_r = e(E(\omega) + v \times B) - \dfrac{m \, \omega_0}{\tau} \dfrac{dr}{dt} - m \omega_0 \omega_0^2 r \tag{4.23}$$

where $F_{Coulomb}$ is the Coulomb force and is caused by an external electric field described by $F_f = -\dfrac{m_e}{\tau} \dfrac{dr}{dt}$ is a frictional force and F_r is the restoring force of the electron due to the return of electrons to their particular equilibrium bonds, which can be negligible. Also, r is the electron movement vector due to the local field acting on the charged particles. The Drude Lorentz equation is inhomogeneous and a second order harmonic differential equation with solution $r = r_0 e^{j\omega t}$ where r_0 [55] can be written as

$$r_0 = \dfrac{\frac{e}{m_e} E_0}{\omega^2 \left((\omega_0^2 - \omega^2) + j \omega \omega \right)} \tag{4.24}$$

45

Displacing a charge, q, by distance $\vec{r}$ is the same as applying an electric moment dipole. Thus, the total polarization vector for n electrons per unit volume can be written as $\vec{P} = \dots$ Therefore, the real and the imaginary part of susceptibility can be derived from the charge polarization:

$$\chi_{p} = \chi'_{p} + i\chi''_{p} = \omega_p^2 \frac{\left(\omega_0^2 - \omega^2\right)}{\left(\omega_0^2 - \omega_0^2\right)^2 + \omega^2 m^2} + i\omega_p^2 \frac{\left(\omega m\right)}{\left(\omega_0^2 - \omega_0^2\right)^2 + \omega^2 m^2} \tag{4.25}$$

Figure 4.6 shows the imaginary part of χ_p as a function of collision frequency ν_{coll} for different ω_p and fixed frequency. Here, it is assumed that the electron density is $N_e = 10^{19}$, 9×10^{18}, and 8×10^{18} m^3, respectively. It is seen that, for low collision frequency, the imaginary part of the susceptibility, which is responsible for the losses, is low and the plasma is not absorptive to the electromagnetic wave. More importantly, at $\nu_{coll} = 10\ GHz$, the imaginary part of χ_p reaches its maximum value when the collision frequency is equal to the electromagnetic frequency, which represents the peak in absorption. The direction of oscillation of the plane polarization is the same as the direction of electron motion. The wave loses its energy in continuously accelerating the electrons.
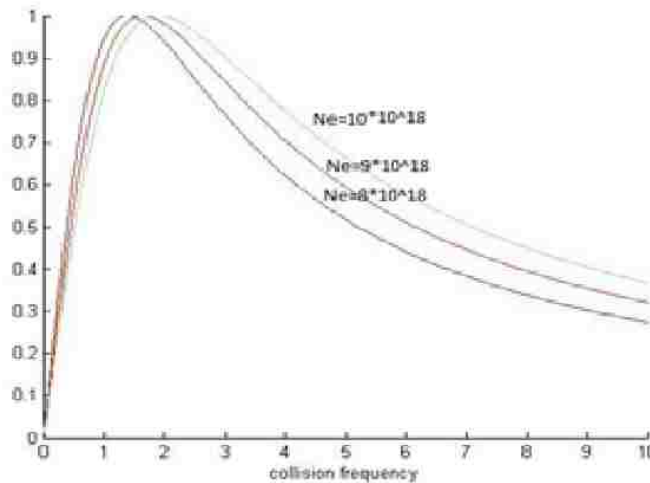
Figure 4.6. Normalized imaginary part of electrical susceptibility as a function of collision frequency (10^{10}) for different electron densities (m^{-3}) based on the Drude model.

From previous expressions, the propagation constant of the electromagnetic wave, k(z), in a collisional plasma is complex (based on $\omega^2 = \omega_p^2 + k^2 c^2$) and is given by:

46

$$k(z) = k_0 \sqrt{1 - \chi_r(z)} = k_r(z) + i k_i(z) \tag{4.26}$$

where k_0/c is the propagation constant, c is the speed of light, $k_r(z)$ and $k_i(z)$ are the real and imaginary parts of the wavenumber, respectively.

The dielectric constant of the plasma has been solved for the real and imaginary parts [42],[56]

$$\sqrt{\varepsilon_j} = r_j \cos(\theta/2) + i r_j \sin(\theta/2) \tag{4.27}$$

where j is the number of the plasma slab and r_j is defined as:

$$r_j = \left[1 - \frac{\omega_p^2}{\omega^2 + \nu^2} \left(1 - \frac{\nu^2}{\omega^2} \right) \right]^{1/2} \tag{4.28}$$

Finally, the real and imaginary parts of the propagation constant for a single plasma slab can be rederived from the dielectric constant of the plasma as

$$k_r(z) = k_0 \left[1 - \frac{\omega_p^2}{\omega^2 + \nu^2} \left(1 - \frac{\nu^2}{\omega^2} \right) \right]^{1/2} \cos(\theta/2) \tag{4.29}$$

$$k_i(z) = k_0 \left[1 - \frac{\omega_p^2}{\omega^2 + \nu^2} \left(1 - \frac{\nu^2}{\omega^2} \right) \right]^{1/2} \sin(\theta/2)$$

where θ is

$$\tan^{-1} \left[\frac{\omega_p^2 \nu}{\omega (\omega^2 + \nu^2 - \omega_p^2)} \right] \qquad \text{Re} (\varepsilon_r) > 0 \tag{4.30}$$

$$\tan^{-1} \left(\left[\frac{\omega_p^2 \nu}{\omega (\omega^2 + \nu^2 - \omega_p^2)} \right] \right) + \pi \qquad \text{Re} (\varepsilon_r) < 0.$$

In Fig. 4.7, the normalized wave number k_r/k_0 in the plasma is plotted as a function of electron density. When the background gas is neglected, the electromagnetic wave is totally reflected back if the wave frequency is less than the plasma frequency.

47
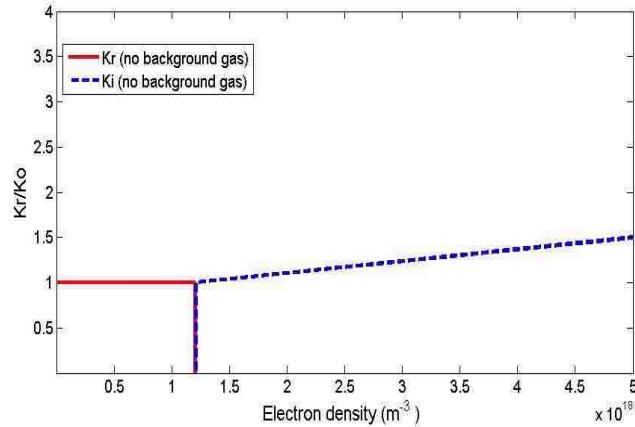
Figure 4.7. The real and imaginary parts of as a function of the electron density without background gas for f=1.6GHz.

From the above equations, as long as $\omega^2 \gg \omega_{pe}^2$, the imaginary part of the wavenumber, like susceptibility, will go to zero when the collision frequency approaches zero. But in the collisional case, the wave power will be attenuated proportional to k_i

$$P^w(z) = P_m^w e^{-2\int_0^z k_i(z)dz} \tag{4.31}$$

The attenuation in dB can be written as 8.68 $\int_0^z k_i(z)dz$.

If the plasma is uniform and collisional, the total attenuated power in the plasma for n reflections is

$$P_n = \sum_{N=1}^{\infty} \|r^{-N}\| P_m^w e^{-2Nk_i z} \tag{4.32}$$

where P_m^w is the power at the entrance of the plasma layer. This phenomenon is different from the case where $\omega^2 < \omega_{pe}^2$, an overcritical plasma. For this condition, the electromagnetic wave turns into an evanescent wave at the interface. As a result, the real part of $k(z)$ indicates the rate of spatial oscillation of electromagnetic wave and the imaginary part of $k(z)$ expresses the decay rate as the wave moves through the absorptive medium.

48

Figure 4.8 plots the attenuated power of the electromagnetic wave for different radiation frequencies propagating in an homogenous plasma.
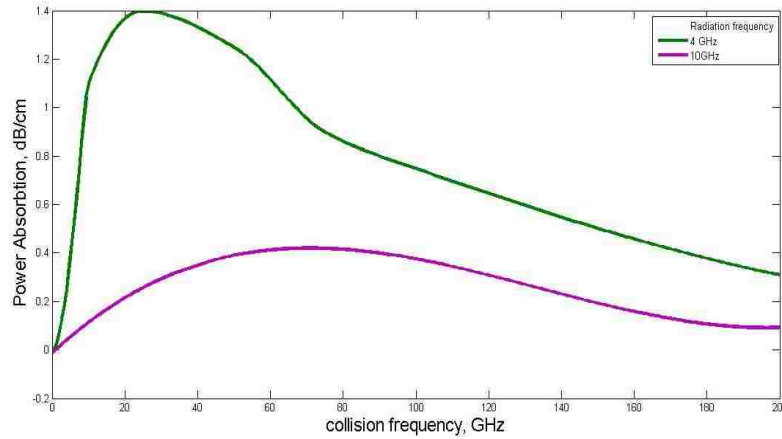
Figure 4.8. Attenuation of the electromagnetic wave in the uniform plasma with f=10 GHz as a function of collision frequency for different frequencies.

Figure 4.8 shows that absorption goes to zero when the collision frequency approaches the extreme limit except for the case when the plasma frequency is greater than the electromagnetic frequency. When the radiation frequency ▮ is almost equal to the collision frequency ▮ the absorbed power reaches its maximum value at resonance. As the electromagnetic wave moves through the plasma, the electrons can oscillate due to the electromagnetic electric field and the electron kinetic energy will be transferred by collisions with the background neutral particles. This causes additional collisional ionization. Transferring energy to the neutral particles is dependent on the collision frequency. If the collision frequency ▮ is low, the electrons do not have sufficient time to respond to the oscillation frequency and the net energy transfer is very poor. This is verified by equation ▮. In the limit of ▮ the collision rate is too high and the 8electromagnetic field cannot accelerate the electrons and little electromagnetic energy can be dissipated.

Figure 4.9 shows an electromagnetic wave propagating toward a plasma with a step density gradient at x=0. The reflected power from the air–plasma interface P_r is [56]

$$\frac{P_r}{P_i} = |r|^2 = \left| \frac{\sqrt{\varepsilon_p} - 1}{\sqrt{\varepsilon_p} + 1} \right|^2 \tag{4.33}$$

where P_i is the incident power on the interface. Figure 4.9a shows the return loss, dB, as a function of ω/ω_{pl}. In the case of a collisionless plasma, the total reflection coefficient occurs when $\omega/\omega_{pl} < 1$ and the attenuated power increases for $\omega/\omega_{pl} > 1$. If collisions are included, the electromagnetic wave always penetrate into the plasma and is not totally reflected at the situation where $\omega/\omega_{pl} = 1$ because the real part of the wavenumber is not zero. By increasing the radiation frequency, the reflected power decreases for all collision frequencies. As the collision frequency increases, the return loss also greatly increases. In fact, by controlling the plasma parameters, the reflected power can be adjusted as desired. Figure 4.9.a shows the insertion loss, dB, as a function

of ω/ω_{pl}.
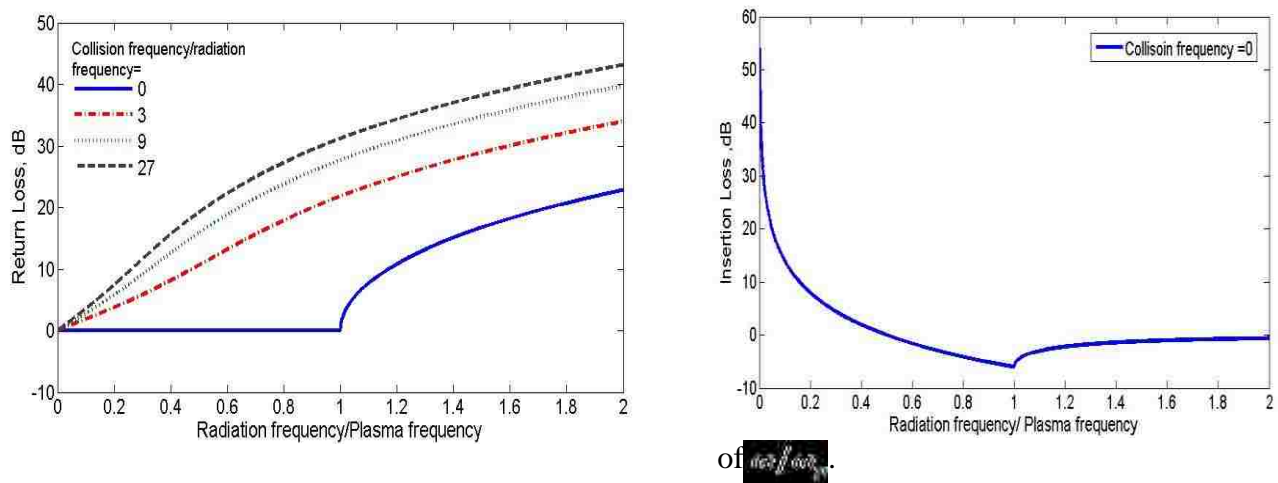
Figure 4.9. (a) Return loss, reflected electromagnetic power, and (b) insertion loss, transmitted power, as a function of ω/ω_c for collisionless plasma.

Knowledge of the plasma permittivity yields the reflection and transmission coefficients, which can be written as

$$r = \frac{\sqrt{\varepsilon_{ext}} - \sqrt{\varepsilon_{s}}}{\sqrt{\varepsilon_{ext}} + \sqrt{\varepsilon_{s}}} = |r| \angle \varphi_r \tag{4.34}$$

With some mathematical calculations, we can find the real and imaginary parts of the reflection coefficient as

50

$$R_{total}(\omega) = \left[|r_{N+1}|^2 \cdots r_N^2 \right]/\left[|r_{N+1}|^2 + r_N^2 + 2r_N r_{N+1} \cos\left(\frac{\phi_{N+1} - \phi_N}{2} \right) \right], \qquad (4.35)$$

$$R_{imag}(\omega) = \left[2r_N(\cdot)r_{N+1}(\cdot) \right]/\left[|r_{N+1}|^2 + r_N^2 + 2r_N r_{N+1} \cos\left(\frac{\phi_{N+1} - \phi_N}{2} \right) \right].$$

The imaginary part of the reflection coefficient r, is responsible for producing the phase difference between the incident and the reflected waves. For m layers of plasma, the total phase difference neglecting multiple reflections is $\sum_{N+1} \phi$.

The reflected and transmitted power for each sublayer of the plasma are related to r and τ as

$$W_r = |r|^2 W_{inc} \qquad (4.36)$$

$$W_\tau = |\tau|^2 W_{inc}$$

and the absorption coefficient in the plasma is given by $\alpha = 1 - |r|^2 - |\tau|^2$.

The plasma layers at atmospheric pressure are the broadband absorbers of electromagnetic radiation. However, plasma parameters must be optimized to obtain efficient attenuation from electromagnetic waves. Generally, the propagation of microwaves into a LIP depends on several factors such as plasma number density, plasma thickness, plasma frequency, plasma lifetime, momentum transfer rate, and incident frequency. It is found that, in order to be a substantial microwave attenuator, a plasma layer must have an electron density in the range of 10^{16}-10^{20} m^{-3} and have a thickness equal to or greater than a wavelength of radiation [19]. In this section we investigate the effects of plasma parameters on the microwaves.

Figure 4.10 plots the properties of microwave in a LIP for different electron densities and plasma slab thickness of d=0.05 m.

According to Fig. 4.10(a), in the resonant regime $\omega_p \approx \omega$ and in some bands the incident power will be attenuated significantly. When the incident frequency increases, the absorption of the electromagnetic wave will decrease due to the low collision frequency of the plasma. Therefore, by increasing the electron density, the absorption will be increased as well. It is seen experimentally that in low density plasmas waves cannot be absorbed.

Figure 4.10(b) plots the dependence of the transmission coefficient on the incident frequency for different plasma densities. It shows that, by increasing the electron density, the

transmitted power will decrease. Thus, in low density plasmas, the GHz wave can be transmitted through the plasma with high transmission and less absorption. At higher frequencies, electrons cannot oscillate with the incident electromagnetic frequency and most of the power will be transmitted through the plasma.
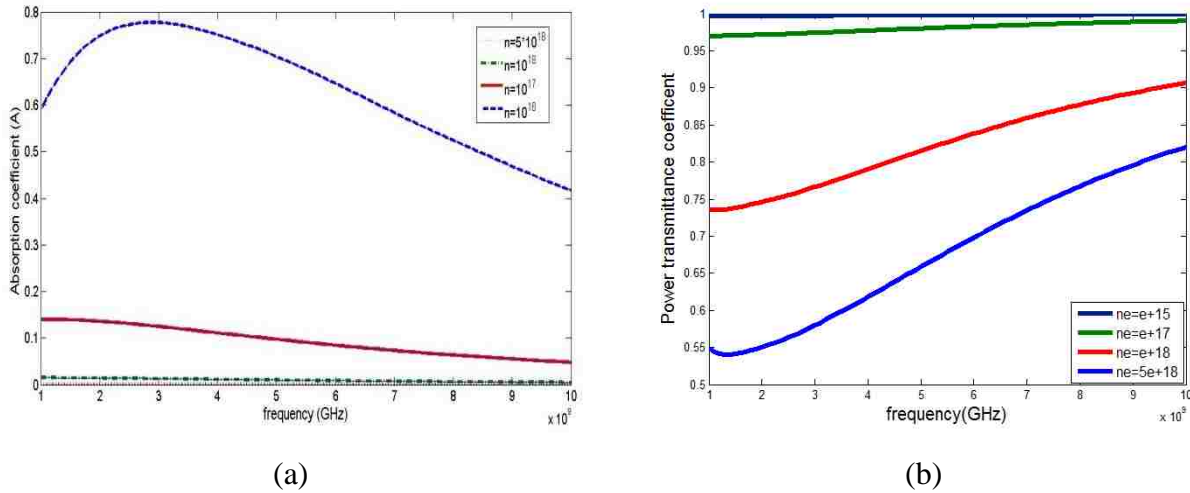
Figure 4.10 (a) Calculated absorption coefficient and (b) transmission coefficient as a function of frequency for different electron densities.

Figure 4.11 plots the characteristics of the propagation of microwaves in a uniform plasma with different collision frequencies and electron density $n_e = 10^{18} m^{-3}$. The plasma axial dimension is assumed to be 0.05 m. It is obvious that the propagation of GHz waves is affected by the collision frequency. Physically, the average absorption coefficient (A $= 1 - \|r\|^2 - \|\tau\|^2$) of the microwave increases with increasing collision frequency since the transferred momentum from the charged particles to the neutral particles increases. Thus, the absorbed energy of GHz waves increases as well. It must be mentioned that the overall change of the reflected energy is distinct; that is, because in this plasma the GHz wave frequency is in the range of the plasma frequency and cannot completely penetrate into the plasma slab. By increasing the collision frequency, the transmission will drop respectively. This result is similar to the case considered by Babaei for microwave propagation in a carbon plasma [57]. It is seen that, by increasing the collision frequency, the curves of transmitted and reflected power become flat, which means that T and R are not affected by changes in frequency.
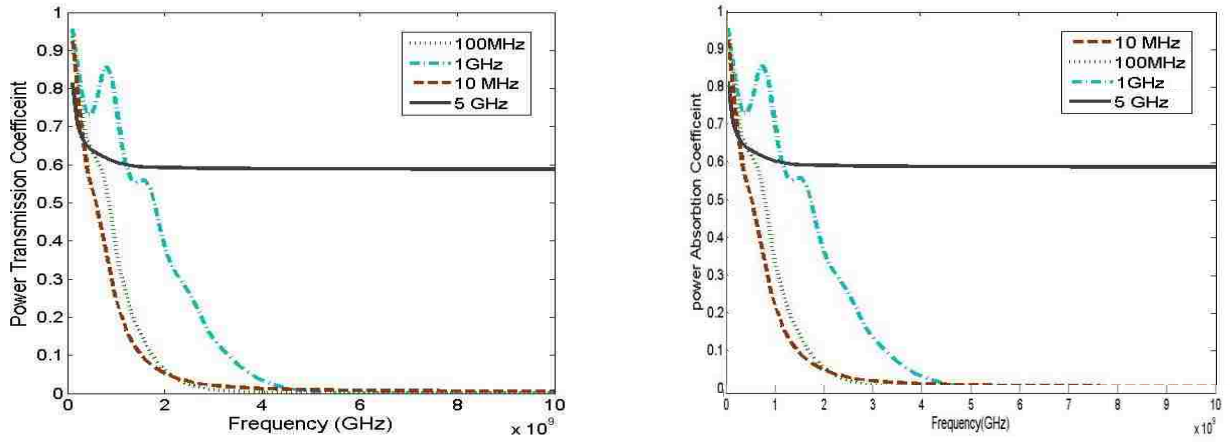
Figure 4.11. The transmission and reflection coefficients as a function of frequency for different collision frequencies.

The above results indicate that the characteristic absorption spectra in the GHz frequency range are very direct and are a practical tool for measuring the collisional properties, temperature, and electron density of LIPs. Meanwhile, by adjusting the LIP parameters such as gas species and temperature, the plasma can be used as a novel tool to control microwave propagation [58].

Figure 4.12 plots the dependence of microwave propagation on different plasma thicknesses, d=0.01 m, d=0.1 m, d=0.3 m, and d=0.5 m. The plasma density and the collision frequency are assumed to be $n_p = 10^{18}$ m^{-3} and $\nu_{en} = 1\ GHz$, respectively. It can be seen that, by increasing the plasma thickness, the transmitted power and the reflected power decrease, but the absorbed power increases. This is due to the fact that the amplitudes and the phases of the microwaves are related to the plasma thickness.
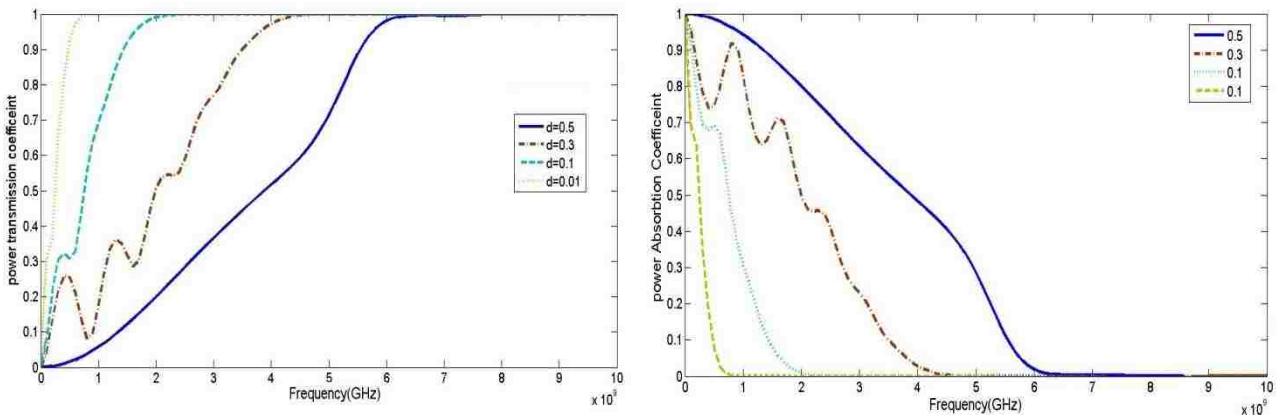
Figure 4.12. The transmitted and reflected powers as a function of frequency for different plasma thicknesses.

It must be mentioned that in our calculations the effects of multiple reflections from the plasma interfaces are ignored. However, multiple reflections have important impact on plasmas used for stealth applications and must be taken into account for accurate results.

As the microwave passes through the finite plasma thickness, it is seen that the wave exhibits a series of geometric, Fabry-Perot resonator-like resonances as a result of constructive and destructive interference of multiple waves scattered from the back and front interfaces [42]. A Fabry-Perot resonator is a pair of partially reflecting parallel plates that can be an ideal model for the problem of reflection from within a LIP. It is assumed that microwave is incident on the front interface and some portion of it is reflected back and some is peneterated into the resonator casuing multiple reflections in the resonator. Assuming that there is no absorption in the plate (R + T = 1), the transmitted and reflected intensities are given by

$$\frac{I_r}{I_i} = \frac{F \sin^2\left(\frac{\Delta\varphi}{2}\right)}{1 + F \sin^2\left(\frac{\Delta\varphi}{2}\right)}$$

$$\frac{I_t}{I_i} = \frac{1}{1 + F \sin^2\left(\frac{\Delta\varphi}{2}\right)}$$

(4.37)

where $\Delta\varphi$ is the phase difference between two successive reflected or transmitted waves $\Delta\varphi = 2kd$. $F = 4R/(1 - R^2)$ is the coefficient of finesse and is a function of the surface reflectivity. Figure 4.13 shows that the intensity profile of these multiple waves is not sinusoidal. A plot of the transmitted and reflected intensity as a function of $\Delta\varphi$ for different F is shown. If $\Delta\varphi = 2kd = \pi, 3\pi, 5\pi, \dots$, then all the power can be absorbed in the plasma cavity. In contrast, when $\varphi = 2kd = 0, 2\pi, 4\pi, \dots$, the transmitted power can be maximal. By choosing the right thickness of the LIP, the plasma can act like a resonator and attenuate all the microwave power through the resonance and collisional absorption.
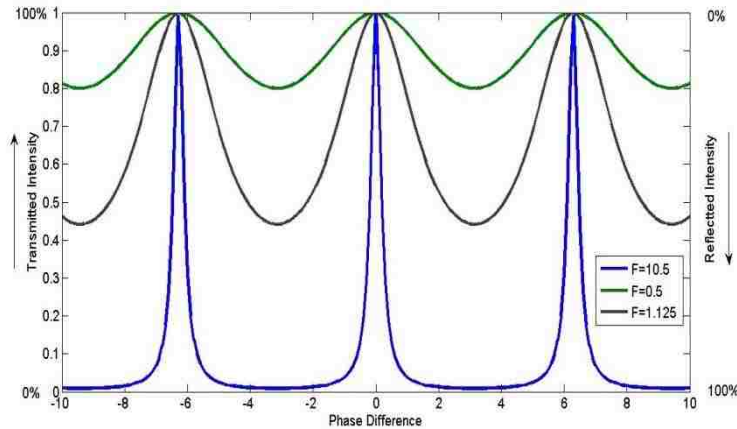
Figure 4.13. The transmitted intensity of the multiple-wave interference pattern produced by a Fabry-Perot

In summary, the absorption, transmission, and reflection of microwaves in a uniform LIP are affected by the plasma parameters such as electron density, plasma thickness, and collision frequency. Thus, GHz waves can be used as a good diagnostic tool for high density such as those found in tokomaks.

Higher frequencies, such as in the THz range, can also be considered to probe the properties of plasma-wave interactions. Due to the high degree of transparency of a LIP to THz waves, the THz waves can be used for space communications, information transmission, or reentry of a spacecraft into the Earth's atmosphere [58].

4.2.2. Electromagnetic Propagation through Nonuniform Plasma

The characteristics of electromagnetic wave propagation through a nonuniform plasma slab are studied in this section. The effects of plasma parameters on the absorbed, reflected, and transmitted powers are discussed. An unmagnetized nonuniform plasma slab can be modeled as a three-dimensional grid, where each grid has a constant electron density n_e. Such grids behave as a tunable matching absorber that can be used for maximum absorption of electromagnetic waves. A nonuniform LIP provides several advantages, such as effective collision frequency, varying plasma density, adjustable plasma dimensions, and tunability. We will discuss the propagation of electromagnetic waves through a one-dimensional plasma slab with uniform plasma subslabs based on the wave impedance method. The calculation results show that the effect of the density gradient on the transmitted and absorbed power, as well as the frequency band of resonant absorption, is

55

significant. This model is acceptable as the first approximation under the assumption that the plasma properties vary slowly along the wave propagation path. In addition, wideband absorption of the atmospheric plasma is achieved for high collision frequency and high electron density with increasing density profile of finite length. Generally, the steady state plasma acts as a frequency selective medium for shielding and stealth applications. Thus, broadband absorption of microwaves can be achieved by modifying the plasma's density gradient [17]. Another complete analysis can be performed using the scattering matrix method (SMM), where each interface and each uniform region is represented by a 2×2 matrix. The SMM leads to a hard and computationally intensive result, which can be shown in a product form of matrices and their inverses.

In this study, an electromagnetic wave given by $E = E_0 exp(j\omega t - \gamma z)$ is normally incident onto a nonuniform plasma. The reflection, transmission, and absorption coefficients are modeled. In each layer the electron density is constant and because of that the propagation constant γ is also constant. In the impedance transformation model, a plane wave propagates into a plasma sublayer obeying Maxwell's equations

$$\nabla \times H = -j\omega\varepsilon_0 E \qquad (4.38)$$

$$\nabla \times H = \sigma E + j\omega\varepsilon E$$

The temporal dependence of the plane wave is expected to be $exp(j\omega t)$ and ε is the complex dielectric constant of the plasma. The resulting wave equation is

$$\nabla^2 E = \frac{\partial^2 E}{\partial z^2} = \omega^2 E \qquad (4.39)$$

where c is the speed of light. The plane wave is propagating in the z-direction, $exp (j\omega t - \gamma z)$, where $\gamma = \alpha + j\beta$ is the complex propagating constant which is given by

$$\gamma = j\frac{\sqrt{\mu\varepsilon_r}\omega}{c} \qquad (4.40)$$

According to the Fig. 4.14, the plasma is divided into equal thin widths and adjacent sublayers. The total electron density profile along the plasma sublayers is assumed to be

$$n = n_{max} \sin(z\pi/d) \qquad 0<z<d, \qquad (4.41)$$

56

where n_{e0} is the maximum electron density at the center of plasma and d is the thickness of plasma. Experimentally, the electron density profile can be measured by different methods, which will be discussed in Chapter 5.
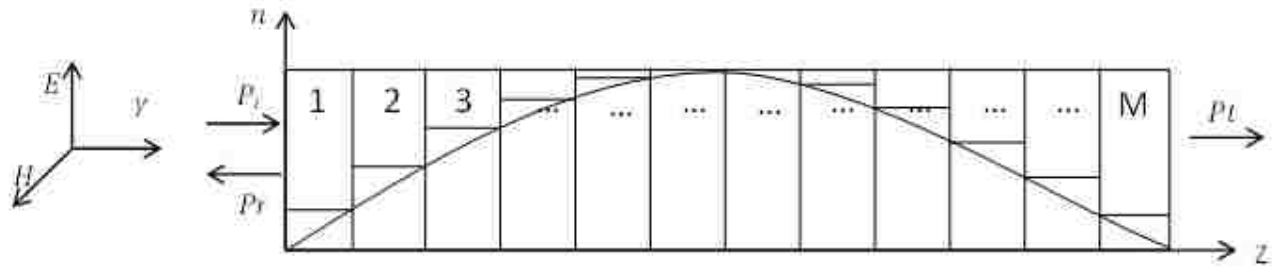
Figure 4.14. Electromagnetic wave propagation through a nonuniform plasma layer with equal width sublayers.

Propagation of electromagnetic waves through a nonuniform plasma leads to multiple reflections and transmissions at the interfaces. The total reflected, transmitted, and absorbed powers, P_r^n, P_t^n, P_a^n, can be calculated. For simplicity, the multiple reflections between interfaces can be neglected. The complex dielectric constant of the each subslab and the reflection coefficient at each interface were calculated earlier.

The total input reflection coefficient is related to the attenuation coefficient of each sublayer α_n and can be written as

$$R_{in}^n = R_1^n + R_2^n e^{-2\alpha_2 d} + R_3^n e^{-2\alpha_3 d} + \cdots + R_n^n e^{-2\alpha_n d}$$ (4.42)

$$R_{in}^n = \sum_{s=1}^{n} R_{s+1}^n e^{-2\alpha_s d}$$

where n is the number of sublayers. For n layers of the plasma, the total phase difference between the incident wave and the total reflected wave neglecting multiple reflections is $\sum_{s=1}^{n} \beta_s l$.

The total reflected power can be calculated from the attenuation constant α_s, and the reflection coefficient R_s of each sublayer. The total reflected power can be rewritten for all n sublayers of the plasma as

$$P_R^{tot} = P_z \left[r^2_1 + \sum_{j=2}^{M} \left(r^2_j \prod_{k=1}^{j-1} \left(e^{-2\alpha_k d_k} (1-r^2_k) \right) \right) \right] \tag{4.43}$$

Thus, the total transmitted power is

$$P_T^{tot} = P_z \prod_{k=1}^{M} \left(e^{-2\alpha_k d_k} (1-r^2_k) \right) \tag{4.44}$$

The electromagnetic wave experiences attenuation in each plasma sublayer, which can be expressed by the total absorbed power

$$P_A^{tot} = P_z - \left(P_R^{tot} + P_T^{tot} \right). \tag{4.45}$$

The effects of unmagnetized plasma parameters on the reflected, absorbed, and transmitted powers are calculated for a nonuniform electron density with a parabolic spatial distribution. To calculate the total reflected power the plasma is divided into 6 subslabs. The plasma frequency is constant in each sublayer. The maximum electron density n_{max} is located at the center of the plasma. The plasma parameters are selected based on previous calculations and measurements. The normalized reflected power P_R^{tot}/P_z as a function of wave frequency f for maximum density $n_{max} = 1.65 \times 10^{18} \, m^{-3}$ and different collision frequencies, 10 GHz - 5 GHz - 1 GHz - 500 MHz, is shown in Fig. 4.15. These collision frequencies can be achieved by changing the pressure of the background gas or the kinetic energy of electrons. The reflection decreases when the collision frequency increases. It is obvious that, for the higher microwave frequencies, the reflection goes to zero. Figure 4.16 plots the normalized reflected power P_R^{tot}/P_z as a function of frequency for a collision frequency of $\nu = 100 \, GHz$ and different maximum electron densities, 5×10^{16}, 5×10^{17}, 5×10^{18}. It can be seen that the reflected power increases when the plasma density increases. From the previous results, it can also be concluded that a highly collisional but low density plasma can reduce the amount of reflections. These two features are difficult to produce because the low density plasmas are usually have low collision frequencies as well. Turbulent plasmas can achieve these conditions.
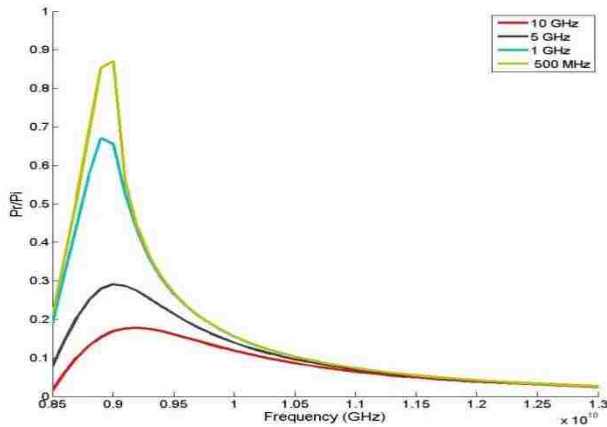
Figure 4.15. Reflected power versus frequency.
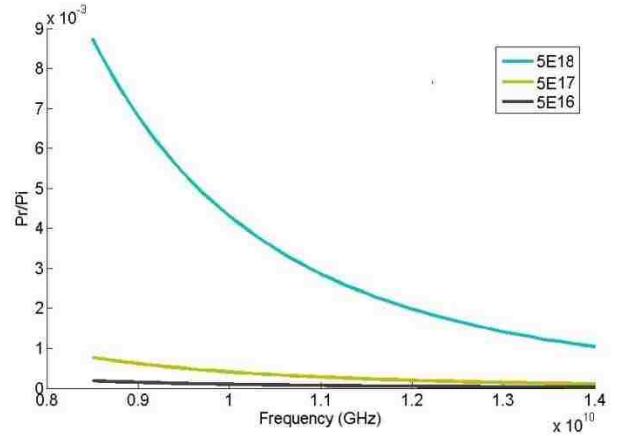
Figure 4.16. Reflected power versus frequency.

4.2.3. Resonant Absorption

It is well known experimentally and theoretically that at low frequencies ($\omega \ll \omega_p$) electromagnetic waves with amplitude of $eE/m\omega c$ <<c cannot propagate into an overdense plasma. However, a high power electromagnetic wave with relativistic parameter $eE/m\omega c \approx$ ε can be totally absorbed by an overdense plasma through the resonant absorption mechanism [59]. The overcritical plasma has a negative dielectric constant, which is very important to a number of areas such as inertial condiment fusion (ICF) experiments for heating a thermonuclear fuel pellet by laser light [60].

In fact, the medium with both negative permittivity $\varepsilon < 0$ and negative permeability μ<0 is called a left handed material (LHM) or a metamaterial. A LHM has unusual properties for creating an "ideal lens" with subwavelength resolution. A common property for materials with negative permittivity is that their boundaries can support propagation of surface waves. Pendry pointed out that a super lens can support evanescent wave amplification by excitation of surface plasmas [61].

Generally, the LIP has two absorption mechanisms, collisional absorption and resonant absorption. In the collisional absorption mechanism, laser light is transformed into electron thermal motion and the electrons can gain kinetic energy through collisions with ions and background gas. In the resonant absorption mechanism, the linear conversion in a nonuniform plasma with sharp

density gradient leads to a resonant excitation of surface plasma wave, which subsequently decays giving rise to energetic electrons [60]. The amplification of evanescent waves on the surface of overdense plasma is a basic concept behind the absorption of electromagnetic wave by overdense plasma.

The surface plasma wave is a mix of longitudinal and transverse waves and can couple with electromagnetic fields. As shown in Fig. 4.17, the surface plasma wave can be excited on the plasma-plasma interface when the dielectric constant changes sign. In Fig. 4.17, surface plasma waves can be excited at x=0. In fact, the surface of a plasma with negative permittivity can behave as a surface wave resonator (SWR). This kind of resonator exists on both sides of an overcritical plasma. When one of the resonators is excited by the external oscillating field, then because of the coupling, the second resonator can be excited as well. In other words, the electromagnetic wave can leak into the plasma slab by exciting the surface plasma wave. The energy of both surface waves can be dissipated by re-emission into the plasma. This can lead to the absorption of the electromagnetic wave.

Only the evanescent wave of the incident electromagnetic wave, which has w/c<k, can excite the surface plasma waves through the resonant excitation. When the quality factor Q of the SWR is high, similar to ordinary resonators, the amplitude of oscillations of the second SWR is the same as the first SWR. This leads to the plasma transparency. The point is that, the coupling between SWRs is related to the plasma thickness. Coupling of the SWRs decreases exponentially when one increases the plasma thickness. In fact, the resonators are isolated from each other and the excitation of first SWR is not transmitted to the other one. This means that the electromagnetic wave can be dissipated in the overdense plasma.
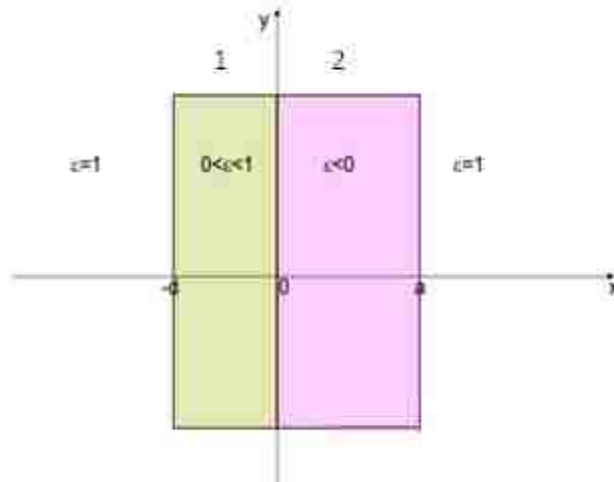
Figure 4.17. Plasma with different dielectric constants.

Since it is impractical to create thin overdense plasma, the transmission of electromagnetic waves through the plasma is also impossible. In practice, the electromagnetic wave can excite only one SWR on one side of the plasma slab. Resonant interaction of the electromagnetic wave with the plasma surface wave can lead to total absorption. The surface waves can dissipate the electromagnetic wave into the plasma.

By assuming that the interface is located at x=0, for x<0 the plasma has a constant plasma frequency of ω_{pII} and for x>0 has a different plasma frequency ω_{pI}. Through the fluid and Maxwell's equations, one can obtain the dispersion relation of surface wave at the cold plasma-plasma interface as

$$k_z = \frac{\sqrt{(A - \omega^2)(\omega^2 - 1)}}{\sqrt{1 + A - 2\omega^2}} \tag{4.46}$$

where $A = \frac{\omega_{pI}^2}{\omega_{pII}^2}$ and ω is normalized to the plasma frequency in region 2 where $x < 0$ and k_z is normalized to the classical skin depth [60]. The plasma surface wave is an evanescent wave propagating on the interface away from x-z plane. By knowing the surface plasma dispersion relation, the frequency range of the evanescent wave for the proper resonance can be calculated.

4.3. Laser Filaments

The characteristics of electromagnetic waves interaction with different configurations of laser filament, in atmospheric pressure, are theoretically investigated. Single wire-plasma line, hollow cylindrical virtual waveguide, two plasma wires, and stack of filaments are considered. Deformable mirrors can be used to spatially distribute the intense ultrashort laser pulses in order to produce multiple filaments. Many factors, such as filament diameter, spacing, operating microwave frequency and electron density can be taken into consideration to calculate the propagation and attenuation parameters. The optimum spatial configurations are also proposed.

Formation of filaments is a result of the nonstationary self-action of laser radiation in a nonlinear media. Filamentation can be achieved by applying an ultra-short high-power radiation sufficient for the appearance of the Kerr self-focusing effect. During the self-focusing the intensity exceeds the medium photo-ionization threshold leading to plasma generation. The plasma filament can be generated by balancing the self-focusing and defocusing effect along the femtosecond laser path. This creates a long weak plasma column in air persisting over several tens of meters and its formation has been observed as far as a few kilometers. Laser filamentation has many applications. It can be used as a terahertz radiation sources triggering high-voltage discharges in megavolt switches and more recently to guide energy in the form of electric current and electromagnetic (EM) radiations. Transfer of pulsed EM radiation in air using the laser plasma as a guiding structure has been proposed in [82], and this scheme is of the great interest since it offers a solution to confine the high natural divergence of the EM radiations directionally and maintains a high energy density over long distances.

Generally, the critical power for self-focusing can be defined as:

$$P_{cr} = \frac{(1.22\lambda_{vr})^2 \pi}{32 n_0 n_2} \qquad (4.47)$$

which represents the minimum instantaneous laser peak power, P, for the self-focusing to be occurred [83]. The self-focusing length can be modified based on the laser power and the medium characteristics:

$$L_{self} = \frac{0.367 a_0}{\left[\left(\frac{P}{P_{cr}}\right)^{1/2} - 1\right]} \qquad (4.48)$$

where $z_R = \frac{\pi w_0^2}{\lambda}$ is Rayleigh range. For many of the experiments, laser pulse energy of ~100mJ with a pulse width of 100 fs is used. It corresponds to an instantaneous peak power of $P \approx 1 \times 10^{12}$ W or 1 TW. For a typical Ti, sapphire laser amplifier driven to saturation operating at a wavelength near 800 nm, the self-focusing length L_{SF} is on the order of a few centimeters.
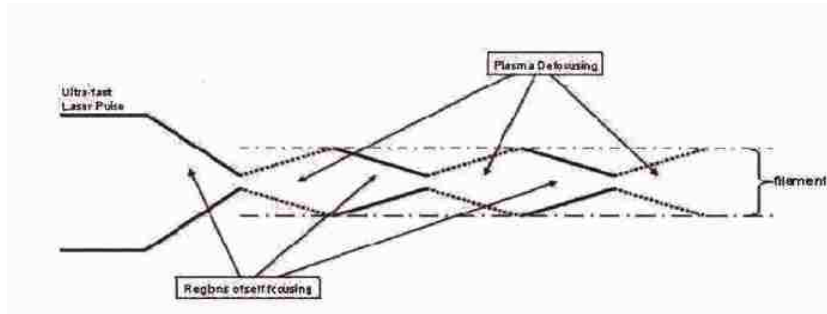
Figure 4.18. Filament formation [83].

4.3.1. Single Dense Plasma Filament

In this work we consider the propagation of an electromagnetic wave along a uniform plasma cylinder surrounded by free atmospheric space. The density gradient of the plasma filament can be modeled properly by a chosen average density. One can obtain the wave equation for the axial component, E_z, of the wave electric field in cylindrical coordinate system as:

$$\frac{\partial^2 E_z}{\partial \rho^2} + \frac{1}{\rho}\frac{\partial}{\partial \rho}(E_z) + \left(\frac{1}{\rho^2}\frac{\partial^2 E_z}{\partial \phi^2}\right) + \frac{\partial^2 E_z}{\partial z^2} + \frac{\omega^2}{c^2}\varepsilon_r \mu_r E_z = 0. \tag{4.49}$$

The azimuthally symmetric solution is $E_{zj} = [A_j J_0(\gamma_j \rho) + B_j Y_0(\gamma_j \rho)] \exp(-\gamma z)$, where $\gamma_j = \sqrt{\gamma^2 + \frac{\omega^2}{c^2}\varepsilon_{rj}\mu_{rj}}$ and j=1, 2 are corresponding to plasma and air respectively. Propagation constant, γ, of the EM waves along the plasma channel can also be written as [85]:

$$\gamma = \omega/c_r(1 - x_0)^{1/2} \tag{4.50}$$

where $x_0 = c(2\pi\sigma_p^2/\omega c) \ln^{-1}(72/c_r)$ is a parameter describing the loss in the line, ω is the microwave angular frequency, and σ is the conductivity of the plasma line defined as $\sigma = \omega_p^2 \nu \varepsilon_0/(\omega^2 + \nu^2)$. The collision frequency is given by $\nu = \nu_N + \nu_{ei}$ and for the weakly

ionized gas at 1atm, the collision frequency is in the THz range. The attenuation length of microwave radiation propagating along the plasma channel is determined by the imaginary part of the propagation constant, $\gamma = 1/\text{Im}(\beta)$, while the real part determines the phase velocity of the wave. The coupling distance d_{coup}, which represents the co-operating distance between the plasma filament and microwaves such that the plasma recombination at the plasma line trailing end does not affect propagation of microwave radiation, can be calculated as: coupling distance=coupling time×microwave signal velocity, i.e.,

$$d_{coup} = \left| \frac{0.3 c_{max}}{c - \beta_{ph}} \right| \times \beta_{ph} = \frac{0.3 c_{max}}{\frac{c}{\beta_{ph}} - 1} \qquad (4.51)$$

By using the definition of the Bessel function, the electric field can be reduced to $E_{z1} = A J_0(\gamma_1 r) \exp(-\gamma z)$ for $r \le a$ (in plasma) and $E_{z2} = B K_0(\gamma_2 r) \exp(-\gamma z)$ for $r > a$ (outside of plasma). The azimuthal component of the magnetic field in the plasma can be written as $B_{\phi 1} = \frac{A i \omega \varepsilon_1}{\gamma_1} J_1(\gamma_1 r) \exp(-\gamma z)$. By considering the boundary condition at r=a, we can get

$$\varepsilon_2 \gamma_1 J_0(\gamma_1 a) K_1(\gamma_2 a) = \varepsilon_1 \gamma_2 J_1(\gamma_1 a) K_0(\gamma_2 a) \qquad (4.52)$$

from which the propagation coefficient can be calculated. We can describe the plasma as a dielectric media and assume the collision frequency is independent of velocity and also ε_1 can be written by so called Lorentz formulation, as $\varepsilon_1 = 1 - \frac{\omega_p^2}{\omega^2}$. In a more rigorous description, the dependence of the electron collision frequency on electron velocity has to be taken into account, but then both *v* and ω_p in Eq. (4.52) can be treated as properly defined effective values [84].

Typical results of numerical calculations of the attenuation coefficient are presented for different collision frequencies. For constant values of the collision frequency and plasma radius, *α* monotonically decreases with growing electron density.
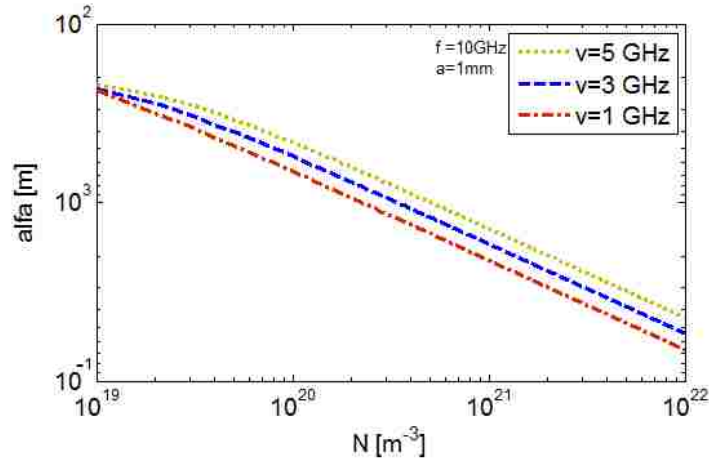
Figure 4.19. Calculated attenuation coefficient as a function of electron density for various collision frequencies.

4.3.2. Two Parallel Laser Filaments

Two cylindrical sets of filament can be modeled as two parallel waveguides separated by distance, d, which can support TEM wave. In this regime the plasma conduction current is sufficiently larger than the displacement current, and the plasma behaves more like a metal than a dielectric. The plasma filament conductivity is very low in comparison with that of metal, which causes very strong microwave damping in such waveguides. The plasma filament can also be modeled as a dielectric based on the total internal reflection. At the specific range of both concentrations of free electrons and the microwave wavelength, the refractive index of laser-induced filaments decreases relative to the surrounding atmospheric air, allowing index guiding of the microwave radiation.
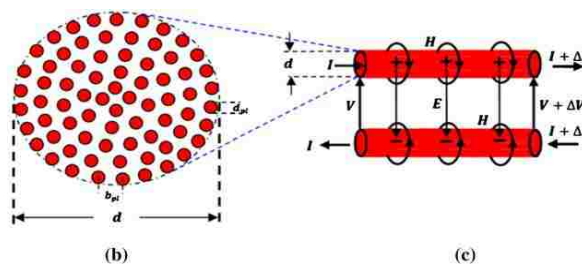
Figure 4.20. Plasma waveguide.

From transmission line theory the dispersion relation can be obtained as [86]:

$$\gamma^2 = \omega^2 \varepsilon \mu \left(1 + i\frac{\sigma}{\varepsilon \omega}\right) = \gamma'^2 \quad \mathcal{W}'^2 \qquad (4.53)$$

65

For $\text{[illegible]} \cdot \omega L$ the spatial decay decrement is: $\text{[illegible equation]}$. The plasma dynamic immediately after the end of the laser pulse producing the plasma is determined by recombination processes. The concentration of n_e after the ionizing laser pulse changes by the following law: $\text{[illegible equation]}$. The imaginary part of propagation constant, [illegible] can be rewritten by $\text{[illegible equation]}$, which describes the time evolution of the decay decrement. The microwave intensity at the output of the transmission line is then given as

$$\text{[illegible equation]} \tag{4.54}$$

where [illegible] is the microwave field intensity at the input. As a result, a pulsed microwave signal is formed and its duration is determined by the decay time of plasma and the distance between the receiving and transmitting waveguide sections. The characteristic duration, t_{mw}, of the microwave pulse transmitted through the double line proves to be inversely proportional to the line length z [87]

$$\text{[illegible equation]} \tag{4.55}$$

The amplitude of microwave pulse propagating in the double line decreases, and the pulse duration decreases proportional to 1/z. As a result, ultrashort microwave pulses are formed at the output of the line and the parameters of these pulses can be controlled by varying the length of the line.

Figure 4.21 shows the loss (db/m) as a function of electron density for different wire distances. The radiation loss [illegible]_{rad}, in addition to the plasma loss, must be taken into account when the lines are separated to some distance and at higher frequencies. An increase in the electrical width [illegible] leads to fewer losses. Thus, to minimize the radiation loss of the line an optimization of the electric width is needed.
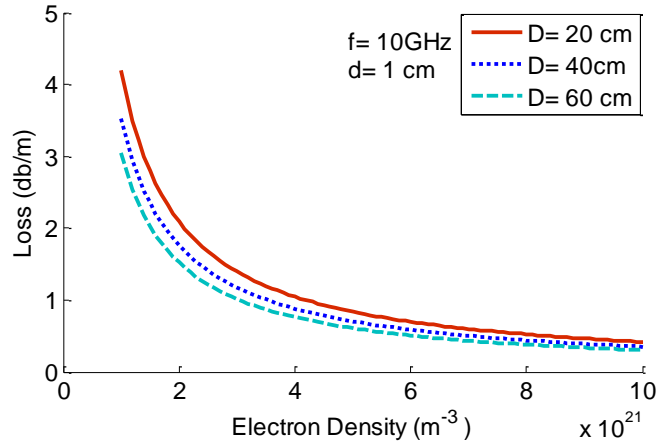
Figure 4.21. Loss as a function of electron density.

4.3.3. Set of Laser Filaments

Since the wavelength, λ_{mw}, of microwave radiation is substantially less than the diameter of the laser filament and the skin depth is larger than radius of filament, the EM wave cannot be coupled efficiently along the plasma wire. Thus, a set of plasma filaments can be produced with a rectangular cross section to act as a bigger filament. When a femtosecond laser pulse with rectangular intensity distribution in its cross section propagates in air, a stack of plasma can be formed behind the pulse and this stack can be used to decapitate the microwave radiation. If the plasma conduction current is sufficiently larger than the displacement current, $\boxed{}$, the field in this plasma decays at a distance on the order of few wavelengths. The efficient concentration of free electrons depends on spacing, b, between adjacent plasma channels, $\boxed{}$. The intensity distribution of the optical field of Gaussian filaments can be expressed as

$$\boxed{} \tag{4.56}$$

where L is the number of rows, n is the number of pulses, r_0 is radius of Gaussian pulse, $\boxed{}$ is pulse duration, and t is total thickness , t=2a+(L-1)b. If the peak power of each pulse in the circle exceeds the critical self-focusing power, $\boxed{}$, a rectangular bunch of

plasma channels can be formed in air, as shown in Fig. 4.22. Under the condition of b $\ll \lambda_{mw}$, the effective electron concentration, $\overline{N}_e$, is calculated as follows:

$$\overline{N}_e = \frac{1}{Ab^2}\int_{-b}^{b}\int_{-b}^{b} N_e(x,y)N_e\,dx\,dy \qquad (4.57)$$
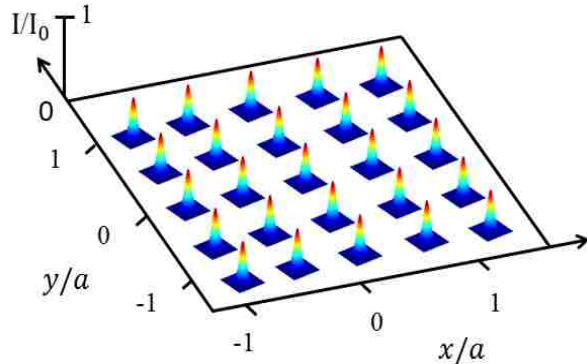
Figure 4.22. Intensity distribution in the cross section of a bunch with regular initial modulation for formation of a rectangular filament channels with N = 25.

For spacing between adjacent plasma channels given as $N_e=10^{15}$, $b_{pl}=$ 700 μm, the effective concentration is about $\overline{N}_e = 10^{12}\ cm^{-3}$ and the plasma thickness is 3.3 mm. As the spacing, b_{pl}, decreases, the mean electron concentration increases, which corresponds to an increase in the conductivity of filaments and the propagation loss of microwave signal. For the case $\lambda_{mw}=3$ cm and $\overline{N}_e = 10^{12}\ cm^{-3}$, the skin depth and the conductivity will be $\delta = 700$ μm and $\sigma = 0.07\ \frac{1}{\Omega\cdot cm}$, respectively. With this in mind, we can shape the set of laser filaments on the surface of supersonic vehicle and couple electromagnetic waves into them

4.3.4. Hollow Filament Waveguide

A circular waveguide of non-ionized atmospheric air surrounded by several rings of plasma filament can be induced by the propagation of high-power femtosecond laser pulses in air [88]. This structure can guide the microwave power in a certain direction and in a same time attenuate it. The effective electron density in this virtual waveguide can be calculated as $\overline{N}_e = \eta N_e$. η is the plasma filling factor, the ratio of plasma channel volume to total volume.
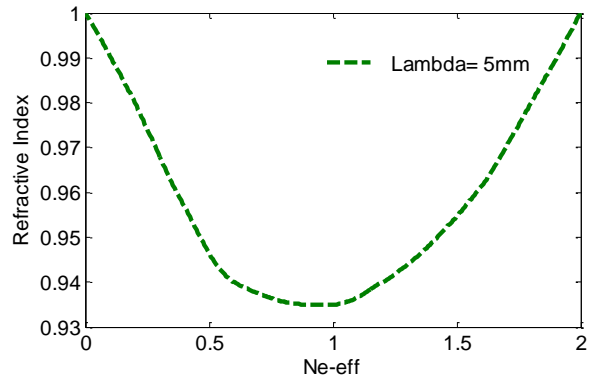
Figure 4.23. Virtual waveguide refractive index as a
function of effective electron density.

This kind of virtual waveguide can be treated as a fiber optic cable (refractive index is less than refractive index of air).

CHAPTER 5

PLASMA AND OTHER DIAGNOSTICS

5.1. Principle of Plasma Shadowgraphy

A LIP is characterized by its high temperature, high density, small dimensions, and very short lifetime. Several effective experimental methods can be used to diagnose the different features of a LIP such as shadowgraphy, interferometry, techniques to infer electrical conductivity, fluorescence detection, and acoustic radiation detection, among others. These methods have their own advantages and disadvantages, but the optical Schlieren and shadowgraphy techniques can be useful to diagnose the spatial and temporal evolution of a nonuniform laser plasma based on the refraction of light for different electron densities. In this technique a beam of light from an intense source passes through the plasma and hits the photographic detecting plane, as shown in Fig. 5.1.
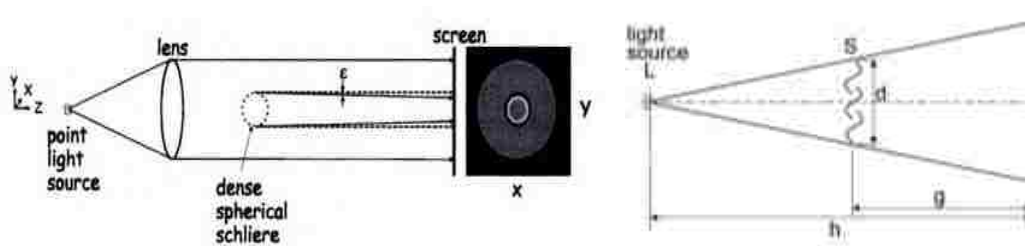
Figure 5.1. A diagram of a parallel-light direct shadowgraph observation of a dense object using a shadowgraphy technique [62].

The optical inhomogeneities refract the light ray in proportion to the gradients of their refractive indices in the x and y plane, as indicated in Eq. (5.1)

$$\frac{\partial^2 x}{\partial x^2} = \frac{1}{n}\frac{\partial n}{\partial x}, \qquad \frac{\partial^2 y}{\partial x^2} = \frac{1}{n}\frac{\partial n}{\partial y} \tag{5.1}$$

The angular ray refraction in the x and y directions for a two-dimensional plasma with axial length of l_z is:

$$\varepsilon_x = \frac{l_z}{n_{00}}\frac{\partial n}{\partial x}, \qquad \varepsilon_y = \frac{l_z}{n_{00}}\frac{\partial n}{\partial y} \tag{5.2}$$

where n_{00} is the refractive index of the surrounding gas. $\frac{\partial n}{\partial x}$ and $\frac{\partial n}{\partial y}$ cause the refraction and if n is uniform the volume is illuminated uniformly [62]. If there is a second derivative of n, there will be variation in the illumination of the screen. Areas where the second derivative is negative will act as converging lenses [8]. The refraction of incident light with angle ε yields displacement Δa on the screen with respect to S, which is the main principle of shadowgraphy

$$\varepsilon \cdot g = \Delta a \tag{5.3}$$

The contrast of the direct shadowgram in parallel light, based on Schardin [30], is

$$\frac{\Delta I}{I_0} = \frac{\Delta a}{a} = g \tag{5.4}$$

If the incident beam has uniform intensity the expressions for minimum resolvable refraction angle ε_{min} and minimum applicable light source diameter d_{min} are

$$\varepsilon_{min} = 1.33\sqrt{\lambda/g} \tag{5.5}$$

$$d_{min} = g\sqrt{\lambda/g}. \tag{5.6}$$

The Schlieren and shadowgraphy methods are closely related and spatial variation of the dielectric constant (electron density) can be measured using both of them. They are appropriate for short lifetime and the high density plasmas but have some disadvantages. The Schlieren method requires an accurate positioning of a knife-edge for refracted light, whereas no such cutoff is needed

in shadowgraphy. Also, the illuminance level in the Schlieren image is related to the first spatial derivative $\frac{\partial n}{\partial x}$. However, shadowgraphy is related to the second derivative $\frac{\partial^2 n}{\partial x^2}$, which makes it suitable for measuring shockwaves and turbulence that occur in the environment of supersonic flight. Eventually the Schlieren image shows the deflection angle while the shadowgraph displays the ray displacement from the deflection,[63]. Shadowgraphy is less sensitive than the Schlieren method and shows the characteristics of the object without major changes in illumination. If the incident beam intensity is I then the detected intensity I_{det} is given by [63]

$$\frac{I_{det}}{I} = 1 + I_o \left\| \frac{\partial n^{\prime 2}}{\partial x^2} + \frac{\partial n^{\prime 2}}{\partial y^2} \right\| \left(\int n(x,z)dz \right)$$

(5.7)
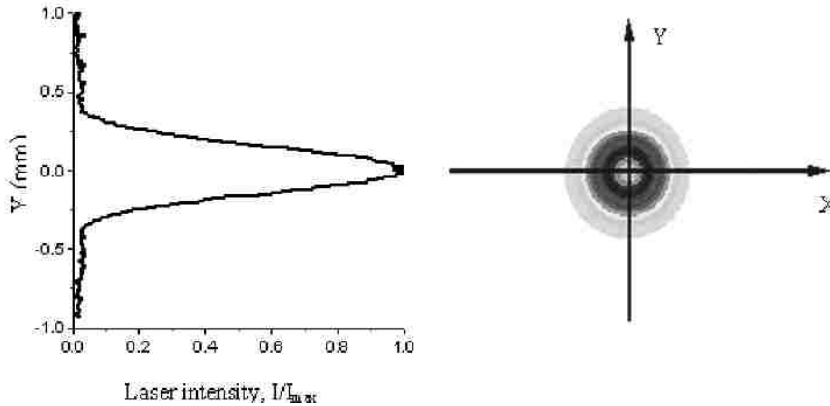
Figure 5.2. Refraction of a laser beam by a uniform laser plasma [64].

5.2. Principle of Acoustic Radiation Diagnostic

Another method to diagnose plasma-related parameters is the acoustic radiation method, which can provide information on the dimension, intensity distribution, and electron density of the LIP. The advantages of the acoustic radiation method are its simplicity, its sensitivity, and its fine spatial resolution, thanks to the slow speed of sound. Figure 5.2 shows the experimental setup for this diagnostic.

The plasma channel can be produced by high power nanosecond laser pulses in air. In the plasma, air molecules are partially ionized through the MPI and CCI processes. Photoelectrons are released from molecules with a kinetic energy of a few eV, corresponding to temperatures on the

72

order of 10^4-10^5 K. The kinetic energy of the initial electrons can be transferred to the background gas, ions, and neutral molecules through elastic and inelastic collisions. The gas is heated to high temperature when thermal equilibrium is achieved in the plasma. It is estimated that the time for energy transfer from electrons to heavy species is in the range of 10^{-9}-10^{-8} s. In addition, a final equilibrium temperature is approximately 1200 K, corresponding to 0.1 eV, which is achieved in a plasma filament 10^{-6} - 10^{-5} s after initiation of the laser pulse [65]. The heated gas expands and leads to shockwaves. The plasma shockwaves propagate outwards to pressurize the air molecules and eventually decay to the sound waves that can be captured by the electret of the fast microphone. For a given gas and a given wavelength, electron density and plasma dimensions can be related to the intensity of the sound wave [65],[66].
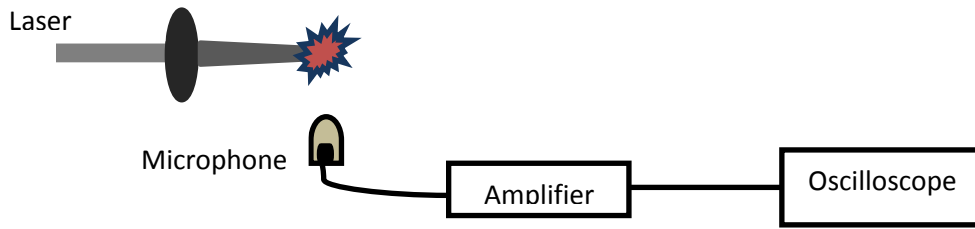
Figure 5.3. Schematic diagram of the acoustic radiation diagnostic employed.

Electrons in the plasma spark are mainly generated from N_2 and O_2 molecules. Thus, the rate equation and continuity equation for the electron density can be rewritten as [67],[68]

$$\frac{dN_e(\chi,t)}{dt} = N(t) \times N(\chi) = N_{N_2}(t) \times N_{N_2} + N_{O_2}(t) \times N_{O_2}$$

(5.8)

where $N(\chi) = N_{mod}(\chi) = N_{N_2} + N_{O_2}$. N_{O_2} represents the density of oxygen $N_{O_2} = 0.21\, N_{mol}$, and N_{N_2} is the density of nitrogen molecules in air $N_{N_2} = 0.78\, N_{mol}$. At atmospheric pressure, this corresponds to $N_{N_2} = 2 \times 10^{19}$ cm^{-3} and $N_{O_2} = 5 \times 10^{18}$ cm^{-3}, respectively. $N_{N_2}(t)$ and $N_{O_2}(t)$ are the corresponding electron generation rates that will be enhanced exponentially due to CCI caused by laser intensity

$$N_{N_2/O_2} = N_{r,N_2/O_2} \times |I(\chi,t)/I_r|^{N_s/O_s},$$

(5.9)

where N and I_r are a pair of experimental values used as reference points. They can be estimated for nitrogen and oxygen from ionization data obtained by Talebpour *et al.* [69],

73

$I_{T,N_2} = I_{T,O_2} = I_T = 10^{13}$ W/cm^2. The corresponding ionization rates are $W_{T,N_2} = 2.5 \times 10^{9}$ W/cm^2 and $W_{T,O_2} = 2.38 \times 10^{9}$ W/cm^2 respectively. In atmosphere, the density of N_2 is three times greater than the density of O_2. We should mention that the ionization rate of oxygen is not much higher than that of nitrogen, although the ionization potential of oxygen (12.1 eV) is lower than that of nitrogen (15.6 eV). Thus, in our estimation, the contribution of ionization both from nitrogen and oxygen must be accounted for.

The electron density can be estimated by

$$W_{ie} = [W_{O_2}(t) \times W_{GO_2}(z) + W_{N_2}(t) \times W_{N_2}(z)] \times \tau, \tag{5.10}$$

where τ is the characteristic ionization time, which is on the order of the laser pulse duration.

The rate of kinetic energy growth of electrons is [50],[52]

$$\frac{\partial W_k(z,t)}{\partial t} = \frac{e^2 \nu_{eff}}{2m\omega^2} \int_{-\infty}^{+\infty} \frac{2\nu(z,t)}{A_0(z)} dz \times W_{ie}(z,t) \times \tau \left\| \frac{\partial\phi(z)}{2} \right\|^2 l, \tag{5.11}$$

where e is the electron charge, ν_{eff} is the effective collision frequency between electrons and neutral particles, and $\phi(z)$ and l are the diameter and the length of laser plasma, respectively. Then, the average energy of the electron in the plasma spot is

$$W_k(z,t) = \frac{e^2 \nu_{eff}}{2m\omega^2} \int_{-\infty}^{+\infty} \frac{2\nu(z,t)}{A_0(z)} dz \times \int_{-\infty}^{t} W_{ie}(z,t') dt' \times \tau \left\| \frac{\partial\phi(z)}{2} \right\|^2 l. \tag{5.12-a}$$

By solving the rate equation and substituting into the previous equation we obtain

$$W_k(z,t) = \frac{e^2 \nu_{eff}}{2m\omega^2} \frac{\tau}{A_0(z)} \left\| \frac{\partial\phi(z)}{2} \right\|^2 l \times \int_{-\infty}^{+\infty} \nu(z,t) dt \times \int_{-\infty}^{t} W_{T,N_2} \left\| \frac{\nu(z,t')}{I_T} \right\| [W_{N_2} + (W_{N_2} + W_{O_2})] dt'$$

$$\tag{5.12-b}$$

The acoustic wave generated by the laser plasma is proportional to the pressure modulation of air $S(t) = A \times P_m f(t)$, where P_m is the amplitude of the pressure wave, A is the gain of the microphone, and $f(t)$ is the temporal function of the shockwave. Due to the small area of the detecting head of the microphone, the spherical sound wave can be approximated as a plane wave. Thus, the sound wave intensity can be written as $I_p = P^2(t)/2\rho_a c_s$, where ρ_a is the density of air

and v_{ac} is the acoustic wave phase velocity. The detected energy of the sound wave from the plasma with length l can be written as

$$E_{ac}(z) = 2\pi_{ac}hl \times \int_{-\infty}^{t=\infty} P^2(t)\,dt = \frac{2\pi_{ac}hl}{2\rho_{ac}c_{ac}} \times \int_{-\infty}^{t=\infty} p^2(t)\,dt \tag{5.13}$$

where P(t)=$S_m(z)i^2(t)/4$ and

$$E_{ac}(z) = \frac{\pi hl}{\rho_{ac}c_{ac}} \times \left| \frac{S_m(z)}{4} \right|^2 \int_{-\infty}^{t=\infty} i^2(t)\,dt . \tag{5.14}$$

Here $S_m(z)$ is the detected peak voltage signal at position z and r is the average distance of the plasma from the microphone. The sound energy is proportional to the absorbed energy.

The sound energy is related to the optical energy absorbed by electrons $E_{ac} = \gamma E_{op}$. Eventually, the peak sound signal is related to the plasma light intensity through [11]

$$S_m(z) = C\sqrt{E_{ac}(z)}, \tag{5.15}$$

where C is a constant given by

$$C = \left[\frac{1}{\gamma} \frac{\pi hl}{\rho_{ac}c_{ac}} \frac{l}{4\pi r^2} \int_{-\infty}^{t=\infty} i^2(t)\,dt \right]^{-1/2} . \tag{5.16}$$

Thus, the temporal distribution of the electron density along the laser plasma can be obtained by using this model in conjunction with the microphone response. The laser used has a Gaussian temporal profile $I(z,t) = I_0 \exp\left[-\left(\frac{t}{\tau_0}\right)^2 \right]$, τ_0 is the initial pulse duration.

The electret microphone that has been used in the experiment has following features:

- $t \sim 15$ μs rise-time
- uses a variable capacitor made of thin sheet aluminized Mylar (electret – dielectric material with a permanently embedded charge)
- FET (field effect transistor) built in to provide pre-amplification
- An external voltage is used to drive the FET
- The resistor sets the output gain and impedance.

5.3. X-Ray Detector

Although the LIP has a wide spectrum, a substantial amount of absorbed laser energy is transformed into X-rays, up to 10%, through the phenomena of bremsstrahlung, bound-bound transitions, and free-bound transitions. Therefore, the LIP can be used as a high brightness X-ray source. The spectral properties of X-rays emitted from the LIP depend on the wavelength, pulse duration, repetition rate, X-ray energy, and choice of target material. An X-ray streak camera, X-ray framing camera, X-ray spectroscopy, gated microchannel plate, and silicon PDs are the main methods which can be used to diagnose the conditions of the targets, air, and study the time-resolved X-ray emission. The obtained spectra, both line and continuum, consist of lines corresponding to the elements of the target.

Generally, X-ray spectra can be obtained with various crystals or grating-dispersed spectrometers, such as a PD and charged coupled device (CCD). The X-ray flux from these measurements can be recorded directly with film or by a solid-state imaging electret. A PD is more able to withstand the high instantaneous flux levels present in laser-plasma experiments, and it is more appropriate for use in direct X-ray detection. Among all types of PDs, the silicon PD (SPD) is more accurate and has a nonlinear response with X-ray energy and gets saturated at comparatively low X-ray fluence [9],[18],[70]. Similar methods can be used to detect the microwave induced plasma (MIP) and microwave-assisted LIP [71].

X-ray intensity is limited at high laser intensity that produces hot electrons in the plasma. By decreasing the laser wavelength and due to the increase in the critical density as a result of efficient laser absorption in the plasma the X-ray intensity increases [72].

Figure 5.3 shows the schematic diagram of a PD. Electrons will be released from the PD by interaction of photons with a photocathode without any delay, and whose energies are related to the wavelength of the incident photons (λ_{ph}). Due to a biasing voltage (V_0) applied between the photocathode and anode, a linear electric field between electrodes ($E = V_0/d$) accelerates the electrons toward the anode. Here d is the separation between electrodes. Electrons will be accelerated by the linear electric field and the electron velocity increases linearly with time t_r, which is approximately the rise time of the PD.

The current density induced by electrons is given by

$$i = qv/d, \tag{5.17}$$

where q is the electron charge and v is the electron velocity due to the linear electric field, which can be written as

$$v = \left(\frac{qE}{m_e}\right)T \qquad 0 \leq T \leq \tau, \tag{5.18}$$

where m_e is the electron mass. Current rises linearly with time until electrons reach the anode after traveling distance d in time τ. The expression for τ is given by [52]

$$\tau = d\left(\frac{m_e}{q}\right)^{1/2} V_b^{-1/2} = 2.7 \times 10^{-6} d/V_b^{1/2}. \tag{5.19}$$

The rise time of the PD is proportional to the bias voltage and the distance between the electrodes. The bias voltage can control the rise time as well as the induced current. The equivalent circuit for the PD can be a simple RC circuit with a time constant given by $R_L C = \lambda$. As shown in Fig. 5.3(b), the induced current flows through the capacitor C and load resistor R_L. The voltage V_L generated across the load resistor rises during the electron rise time and reaches maximum value V_m and then decays exponentially with time constant λ, which can be expressed as

$$V_L = V_m \exp(-T/\lambda), \tag{5.20}$$

which means that the fall time of the induced current is limited by the discharge time constant of the capacitor. Space charge on the PD cannot eliminate the induced current between the electrodes.
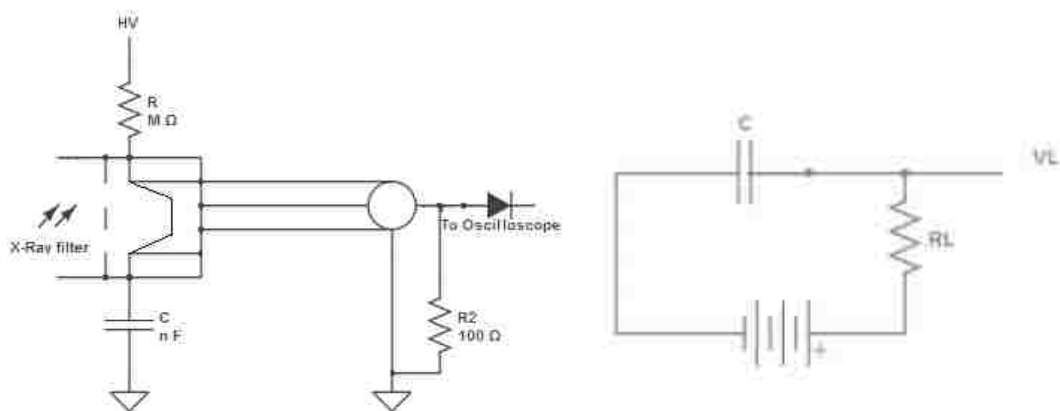

Figure 5.4 (a). Schematic diagram of single channel PD; (b) equivalent circuit of the PD.

Three main mechanisms are responsible for X-ray emission from the LIP, Bremsstrahlung, line emission from partially ionized atoms, and recombination emission occurring when an electron recombines with an ion. The X-ray yield due to these processes is dependent on the constitutive parameters of the target, air. Generally, Bremsstrahlung generates the continuum radiation and line emission is responsible for the line spectra. Thus, the total intensity of X-ray radiation can be calculated from the line and continuum intensities. The intensity of Bremsstrahlung radiation from a laser plasma of volume V (cm^3), electron density N_e (cm^{-3}), temperature T_e (eV), and ion density N_i (cm^{-3}) can be written as

$$\frac{dW_b}{dt} = 1.5 V N_e N_i \left(\frac{T_e}{k_B T_e}\right)^{1/2} \exp\left(-\frac{h\nu}{k_B T_e}\right) \tag{5.21}$$

Radiation is mostly emitted as a result of transitions between bound states of the ions. Therefore, the spectrum of emitted radiation consists of lines at discrete wavelengths rather than as a continuum. Power emitted as line radiation from a plasma of volume V (cm^3) is given by

$$W_{line} = 3.1 \times 10^{-25} V (k_B T_e)^{1/2} N_e N_i \exp\left(-\frac{E_a(t)}{k_B T_e}\right) \; \text{W}, \tag{5.22}$$

where $E_a(t)$ is the absorbed energy.

X-ray emission seems to be proportional to the volume and to the square of the electron and ion densities ($\propto N_e N_i$, where $N_e \approx N_i$) of the coronal plasma.

5.4. Microwave Detector

A piece of x-band waveguide that was sliced off was used to detect the microwave signal. The detector is embedded in a wall of microwave absorbing material. The receiving end of the detector is positioned in the maximum field of the TM$_{01}$ mode, which was predicted experimentally to be at a flare angle of approximately 10° from the geometrical center of the radiating horn antenna. The received signal is sent via a low loss coaxial cable into the screen room where it is monitored on an oscilloscope.

The microwave detector signal will not only be used for confirming the production of microwaves but also for collecting information on the time-synchronization of the laser pulse and the microwave wave beam.

Chapter 6

EXPERIMENTAL SET-UP AND DIAGNOSTICS

This chapter will present a description of the laser system, the HPM system, the diagnostics used in the experiments, the synchronization procedure of the laser and microwave wave beam, the experimental results, and the analyses of the data.

6.1. Characterization of the Q-switched Nd:YAG LIP

Here, the estimated laser energy absorbed in the LIP (or the laser spark) and typical microphone and PD responses to the laser spark will be discussed.

6.1.1 Energy Absorbed in the Laser Spark

In this set of experiments, a high power pulsed Nd:YAG Q-switched laser (Surlite SLII-20, Postmaster, wavelength: 1064 nm, energy per pulse 600 mJ) is used. The laser output is a Gaussian beam with cross section 7 mm, homogenous beam intensity (+/- 5%), and beam divergence of 0.5 mrad. The FWHM of the laser pulse is 7±1 ns.

The Gaussian cross section of the laser beam is reduced to 50 µm using a set of 1064 nm-coated cylindrical plano-convex lens (f=20 cm). All IR optical components are coated to provide 99% transparency at 1064 nm light.

Laser energy can be measured after the focusing lens by placing the energy meter in contact with the output edge of the objective lens where the laser intensity is not so high as to damage the detector. Due to dust in the air, transparency of the mirrors, and the coating of focusing lens, it is

found that almost 5% of the laser output beam's energy is lost. The laser energy available immediately after the focusing lens corresponding to a 600 ± 5 mJ laser output was measured by the energy meter to be 570 ± 5 mJ, corresponding to the measured incident laser energy to the focal spot. Therefore, laser energy of 570 ± 5 mJ was focused on to the 50 ▮▮▮radius spot size. The transmitted energy level is used as a reference level.

In order to measure the transmitted energy through the plasma the energy meter was placed 1 cm after the focal spot where the transmitted laser energy can be measured. These experiments were conducted at atmospheric pressure and in an uncontrolled environment. Due to the fact that the maximum plasma frequency divided by the laser frequency near the focal spot is ▮▮▮ < 0.01, we can conclude that small portion of the incident laser flux is scattered by the plasma and the laser absorption is primarily due to CCI and MPI processes. An average transmitted measured voltage is 86 mV, which is 7% of the incident energy. Therefore, approximately 93% of incident energy of the Nd:YAG laser pulse energy was absorbed at 631 Torr by the plasma at the focal region.

Figure 6.1. The time integrated photograph of the emission from an air spark using open shutter camera. The laser entered from the left hand side.

Figure 6.1 shows the photograph of LIP that was captured by an open shutter camera transverse to the direction of the laser.

6.1.2 Microphone and Photodiode Response of Laser Spark

Shockwaves generated by the laser spark can be detected with a broadband microphone which converts the change in air pressure into voltage. The typical signal captured by microphone from shockwaves of LIP is presented in Fig 6.2. The rise time of the microphone that was used is 20 µs.
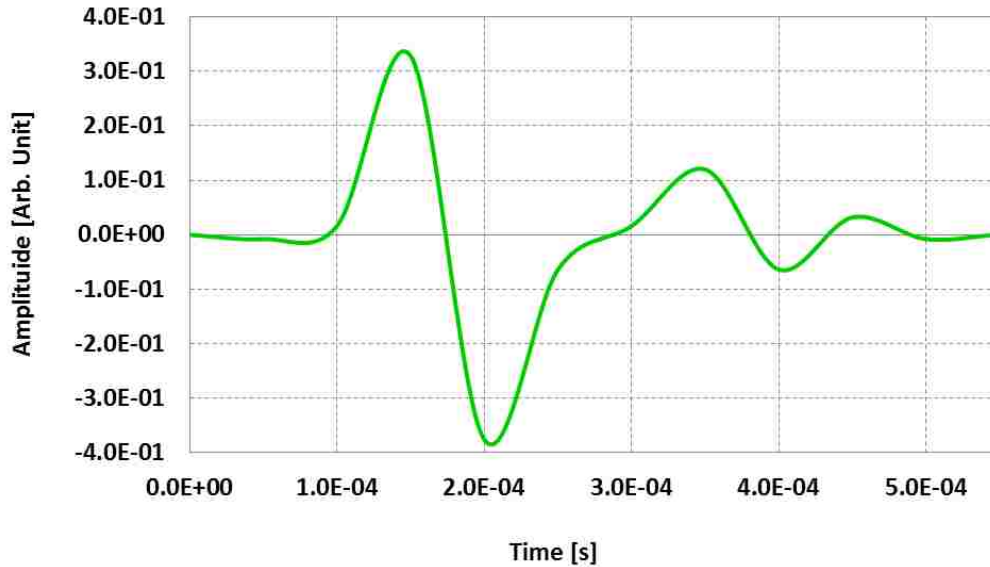
Figure 6.2. Microphone response to laser spark.

A fast PD was implemented to capture the optical emission from the plasma. The PD used in these experiments has a rise time of 10 ns. Figure 6.3 shows the PD response indicating a total laser plasma lifetime of ~200 ns. The PD was also used for detecting temporal synchronization of the microwave signal.
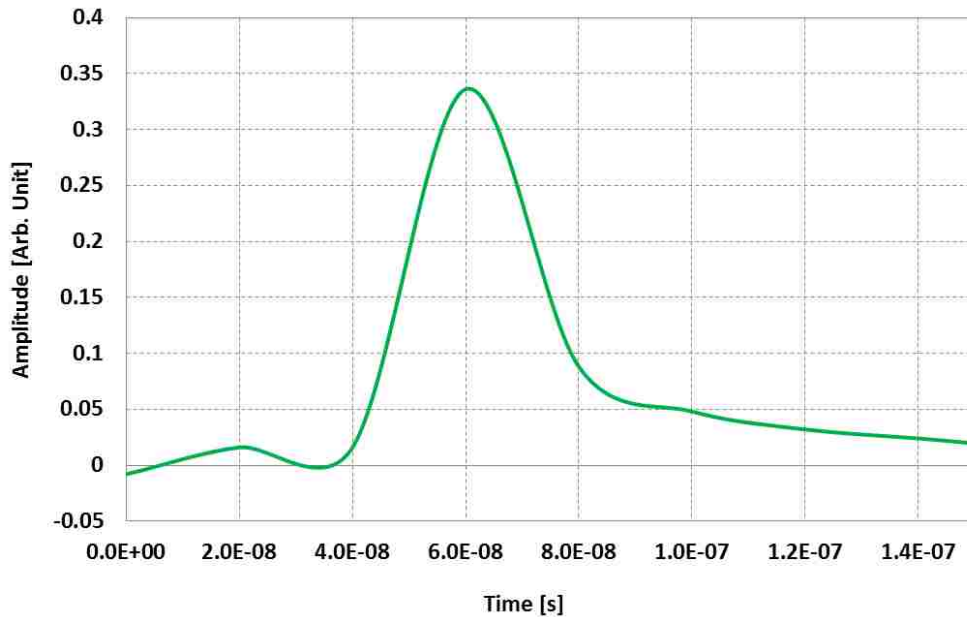
Figure 6.3. PD response of the laser spark.

6.2. SINUS-6 Accelerator and Microwave Source

6.2.1 Characterization of the SINUS-6 Accelerator

To generate high-power pulsed microwaves, two types of electron beam accelerators can be used: induction accelerators and direct-action accelerators. Direct-action accelerators have two types: capacitive and inductive energy storage system. The SINUS-6 electron accelerator that is used in this experiment is a capacitive type.

The SINUS-6 is a high current, short pulse, repetitive pulsed electron beam accelerator at the Pulsed Power, Beams, and Microwaves Laboratory at the University of New Mexico. Figure 6.4 presents a block diagram of SINUS-6 electron beam accelerator.
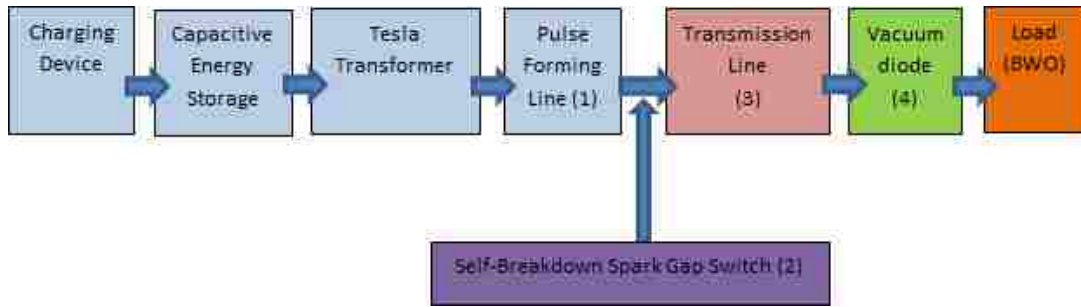
Figure 6.4. Block diagram showing the principle elements of the SINUS-6.

The main parts of this accelerator are: primary capacitor, Tesla transformer, a pulse-forming line, a high voltage spark gap switch, a transmission line, magnetically insulated oil-vacuum interface, and a cold cathode vacuum diode. The SINUS-6 electron beam accelerator is capable of providing a maximum voltage and current of 700 kV and 6 kA, respectively. It has a FWHM duration of 12 ns. Figure 6.5 shows the voltage from capacitive divider probe.

Figure 6.6 shows the jitter time of the self-breakdown switch for a sample of 23 shots. Despite some large fluctuations, there are instances of consecutive shots with almost no jitter.
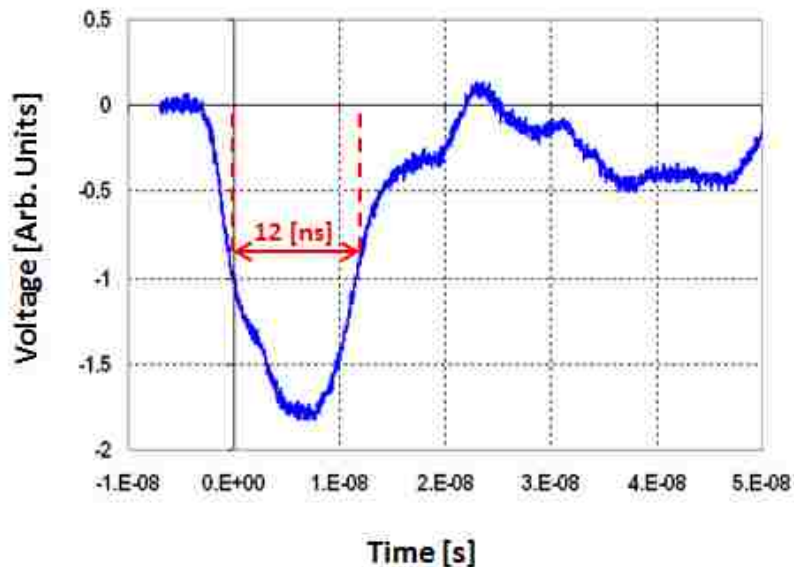
Figure 6.5. SINUS-6 diode voltage waveform.
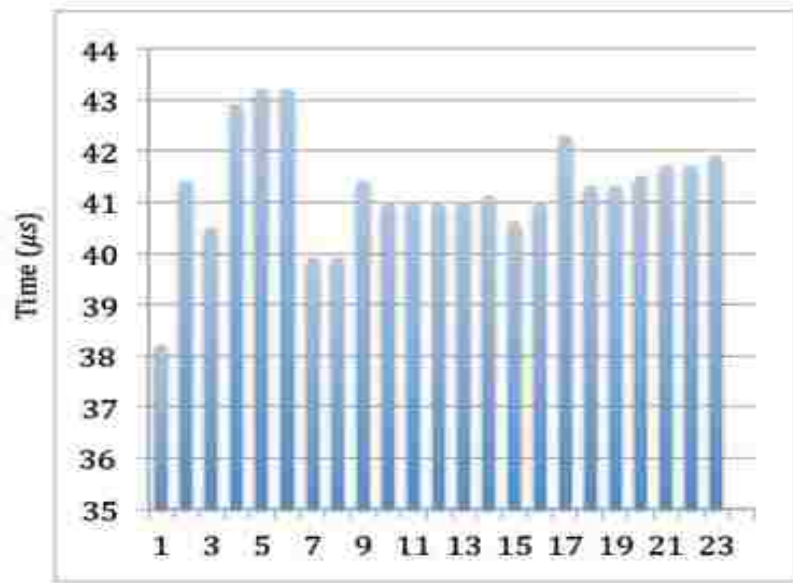
Figure 6.6. Quantitative measurement of the jitter time of SINUS-6.

6.2.2 Microwave Source

An HPM pulse can be generated using a slow wave structure such as is done in a backward wave oscillator. A backward wave oscillator (BWO), also called carcinotron or backward wave tube, is a vacuum tube that is used to generate intense microwave pulses. It belongs to the traveling-wave tube family. It is an oscillator with a wide electronic tuning range. An annular cathode with explosive emission emitter is used to generate an electron beam that interacts with a slow-wave structure (SWS) and produces Cherenkov radiation. It sustains the oscillations by propagating a traveling wave backwards against the beam. The generated electromagnetic wave power has its group velocity directed opposite to the direction of motion of the electrons. The generated HPM beam is reflected in the forward direction by means of a resonant reflector and extracted using a horn antenna. Figure 6.7 shows a schematic diagram of a BWO and the typical radiated mode.

To perform the experiment with BWO, we first aligned the electron beam to be concentric with the SWS. To verify the spatial distribution of output mode, we placed a neon discharge tube grid in front of the horn antenna to be exposed to the microwave signal. Figure 6.8 shows the output "donut"-like cross-section obtained experimentally, indicative of the TM_{01} mode pattern.
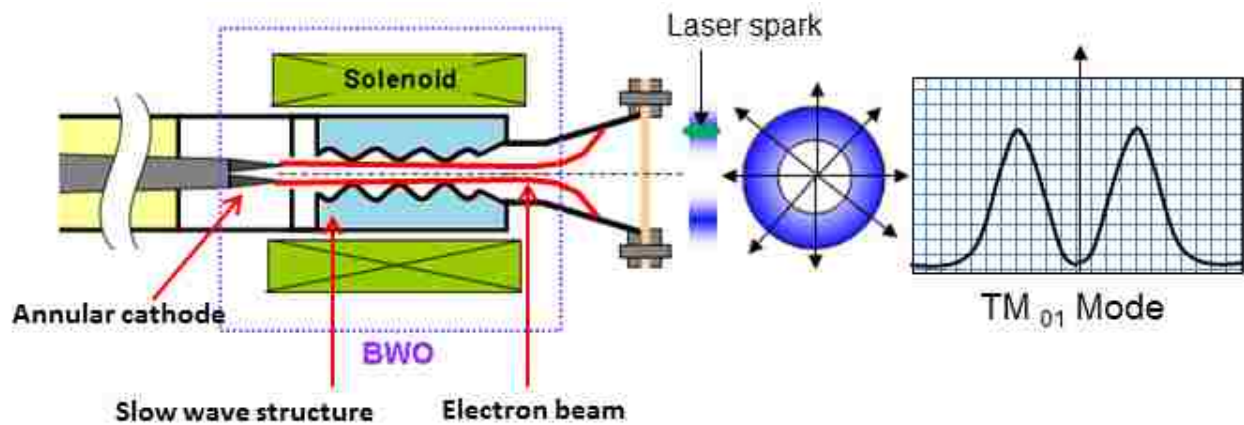
Figure 6.7. Spatial distribution of the TM_{01} mode.
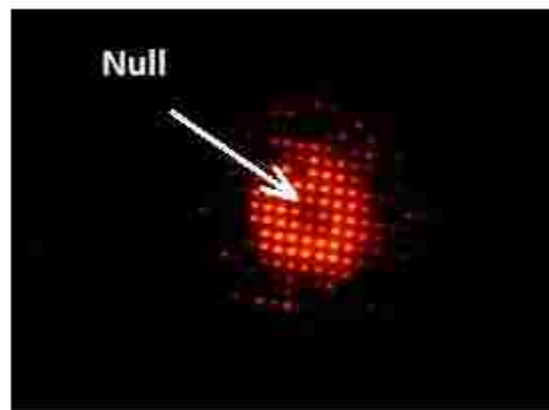
Figure 6.8. Spatial distribution of the TM_{01} mode produced by the BWO and captured using an array of neon discharge bulbs.

Experiments were conducted at a peak voltage of 430 kV and constant magnetic field of 2 T. Under these conditions the BWO is capable of generating microwave powers reaching 400 MW with operating frequency of 10 GHz.

Figure 6.9 (left) shows a representative sample of the RF pulse measured experimentally using a 12 GHz digital oscilloscope. Figure 6.9 (right) is the FFT of the RF signal showing a single frequency operation of 10.2 GHz.
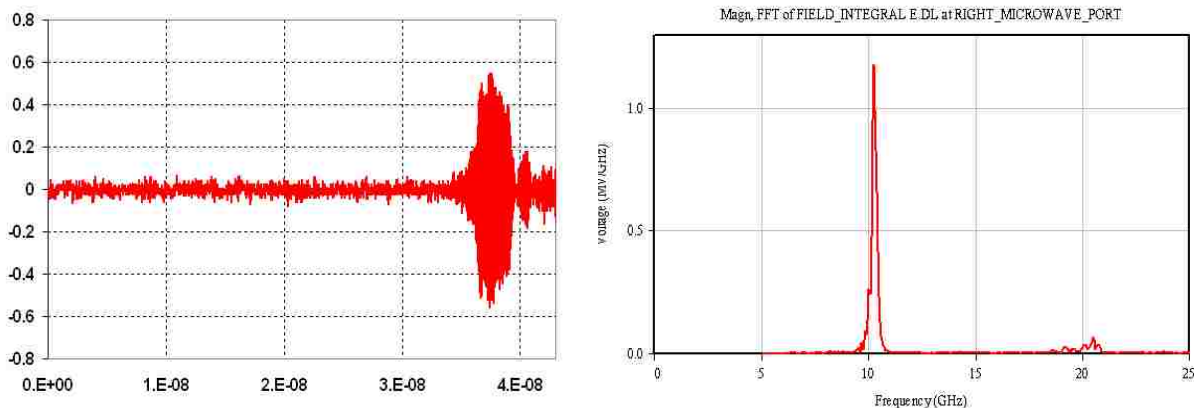
Figure 6.9. Example of RF signal (left) and its corresponding FFT (right).

Thus far the characteristics of the laser, pulsed power, and HPM system that were used in these experiments have been outlined. In the next section the spatial and temporal synchronization will be discussed.

6.3. Microwave Laser Synchronization

In order to achieve laser initiated microwave breakdown of air, a single pulse from the 20 Hz rep-rated laser spark had to be synchronized in space and time with a single microwave wave beam. In this section the procedure for temporal synchronization will be discussed followed by spatial synchronization.

6.3.1 Scheme for Laser-Microwave Temporal Synchronization

SINUS-6 is operated by a LabView program. The two objects that are controlled by the LabView program are the discharge of the capacitor bank energy into the solenoid followed by firing of the accelerator. Figure 6.10 shows the timing diagram of SINUS-6. Two 150-10██ pulses with a delay of t=3 ms between them are sent from a control box to trigger the two actions mentioned above. It takes t=3 ms for the current to reach its peak value after the capacitive energy is discharged into the solenoid.

87
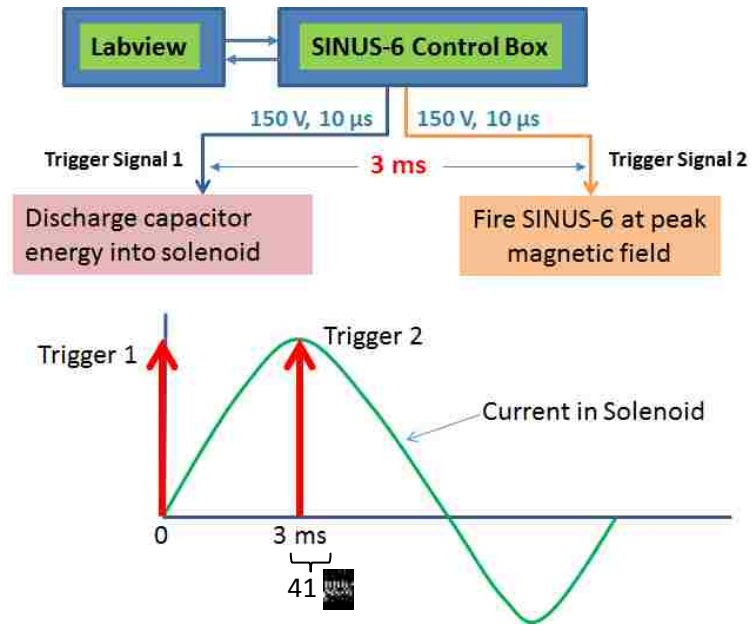
Figure 6.10. Timing diagram of the two signals sent from the SINUS-6
control box, trigger signals.

Approximately 41 µs after the second trigger signal is sent, voltage appears on the diode. This time includes the charging time of the Tesla transformer discussed in section 6.2.1.

The laser system requires two 10 µs-5V trigger signals, one for the flash lamp and one for the Q-switch. The delay between these signals is 190 µs. A Berkeley Nucleonics, Model 725, 8 channel delay generator was used to set the time delay between all the trigger events required for synchronizing the microwave pulse with the laser spark.

A master clock that uses pulse streaming at 20 Hz was used to control the flash lamp and the Q-switch. A push button switch was implemented to serve two functions:

(i)   To keep the SINUS-6 control box isolated from the delay generator,

(ii)   To select a single pulse from the master clock that would be used for synchronizing the laser spark with the microwave pulse.

Figure 6.11 shows the timing diagram that summarizes the trigger timings involved in the synchronization of the pulses.
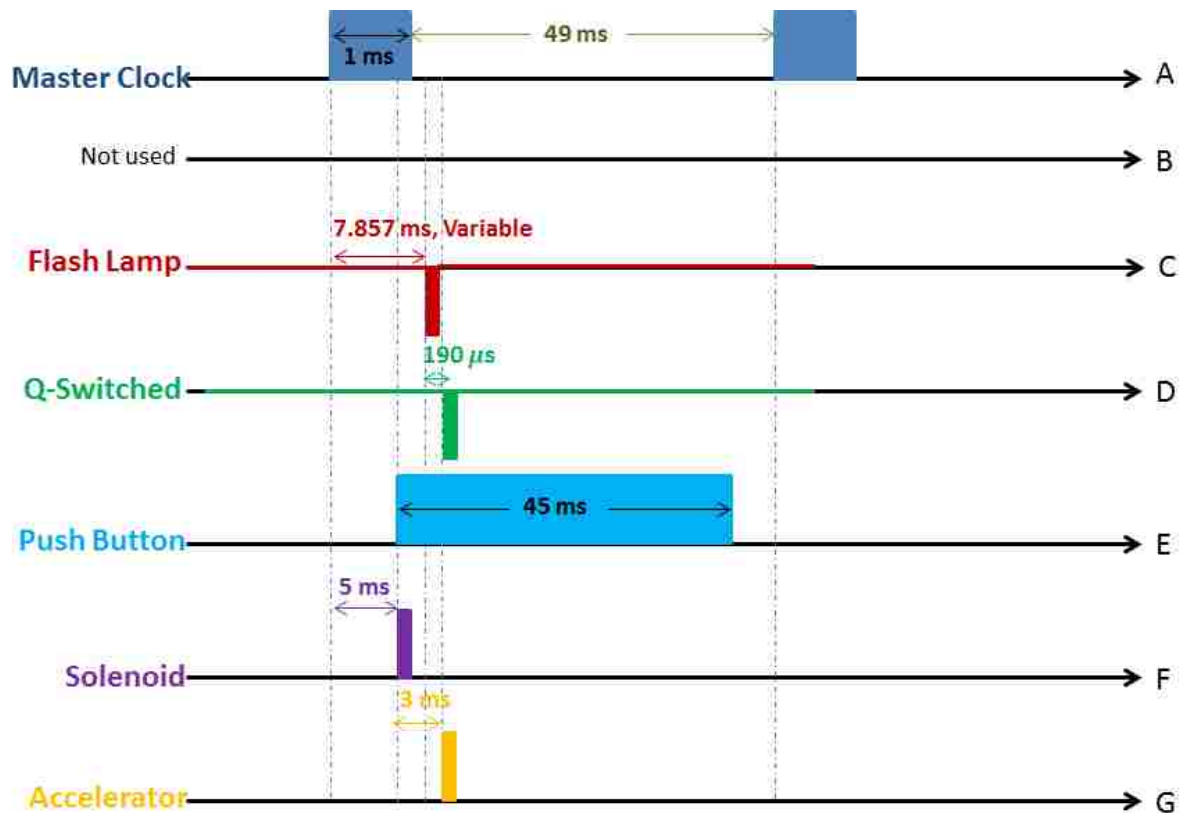
Figure 6.11. Timing diagram for tr0igger pulses used for synchronization.

The duration of the push button switch was kept to less than 49 ms in order to prevent the triggering of two consecutive pulses from the master clock. The flash lamp delay time (indicated as variable on Fig. 6.11) was adjusted to synchronize the laser spark (Q-switch) with the microwave pulse. The logic program for the delay generator input and output channels are written based on C language.

Figure 6.12 is a photograph of the diagnostics and controls. Additional safety features were included to protect the Tesla transformer charging circuit and the SINUS-6 control box from the occasional spurious signals that are sent from the delay generator when its logic program is altered and memory is being refreshed. The spurious signals are a series of 3 pulses of varying pulse durations.
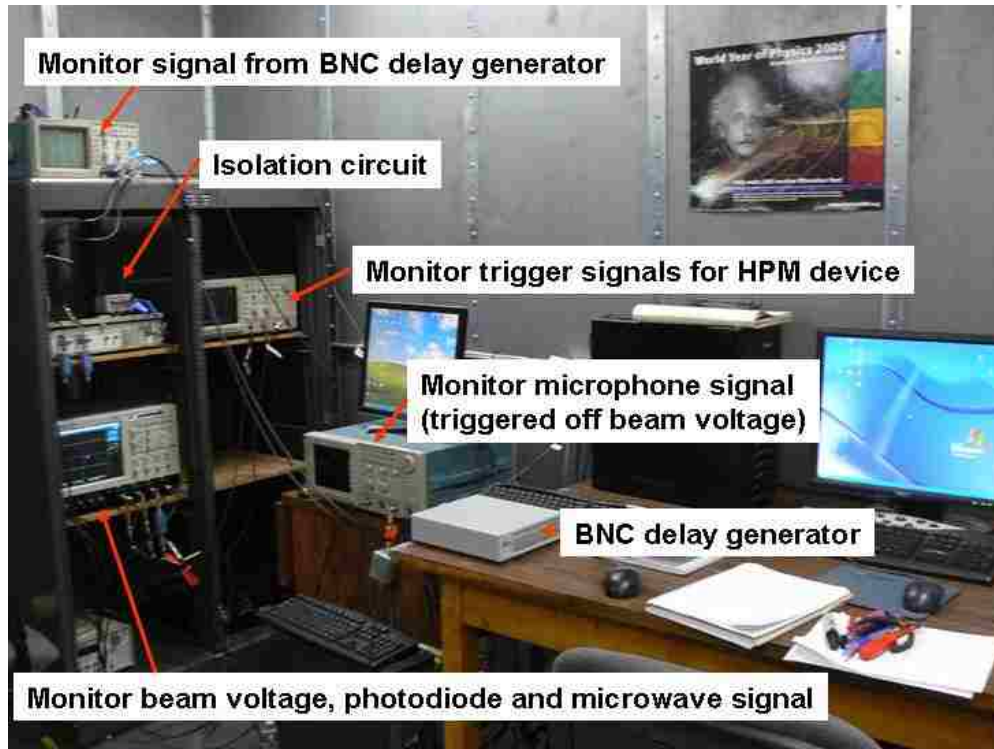
Figure 6.12. Photograph of the diagnostics integrated in the screen room.

When the push button switch (discussed previously) allows the trigger pulses from the delay generator to be received by the SINUS-6 control box, the signal first passes through two specially designed pulse stretchers. The output of the pulse stretchers are T'd off where one part of the signals are observed on an oscilloscope and the other part is kept isolated from the SINUS-6 control box by means of a Tektronix relay switch which stays in the open state. The acceptable shape of the pulse observed on the oscilloscope is shown in Fig. 6.13. Once this waveform was confirmed on the oscilloscope, a second series of pulses was accepted from the delay generator, this time with the relay in its closed state so that trigger signals could be received by the control box and from there sent for microwave production.
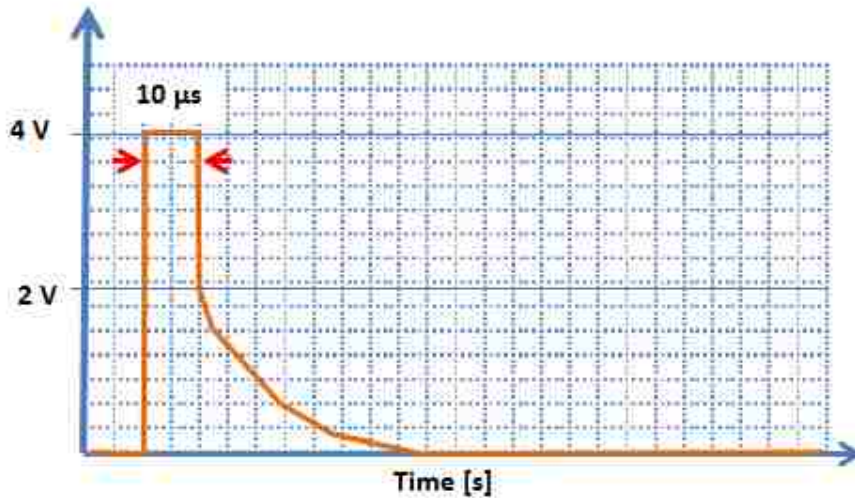
Figure 6.13. Output of pulse stretcher for safe operation of SINUS-6 system.

6.3.1 Scheme for Laser-Microwave Spatial Synchronization

In order for the laser spark to interact with the microwave signal spatial synchronization of the two signals was essential. This section will describe how spatial synchronization was achieved. A parabolic dish was used to focus the microwave energy. The electron beam voltage was increased to increase the microwave output power to a high enough level that it would cause air to breakdown in the focal point of the parabolic dish. A Sony Alpha digital camera with manual shutter option was used to capture the photograph of air breakdown occurring from the focused microwaves. A three-dimensional grid was used to resolve the location of the air breakdown region. Figure 6.14 shows the air breakdown. Similar photographs as shown in Fig. 6.14 were used to determine the focal point of the dish. The laser spark was then positioned in this spot. Figure 6.15 shows a comprehensive schematic of the experimental setup.

Figure 6.14. Photograph of air breakdown attributed to the focused microwave wave beam.
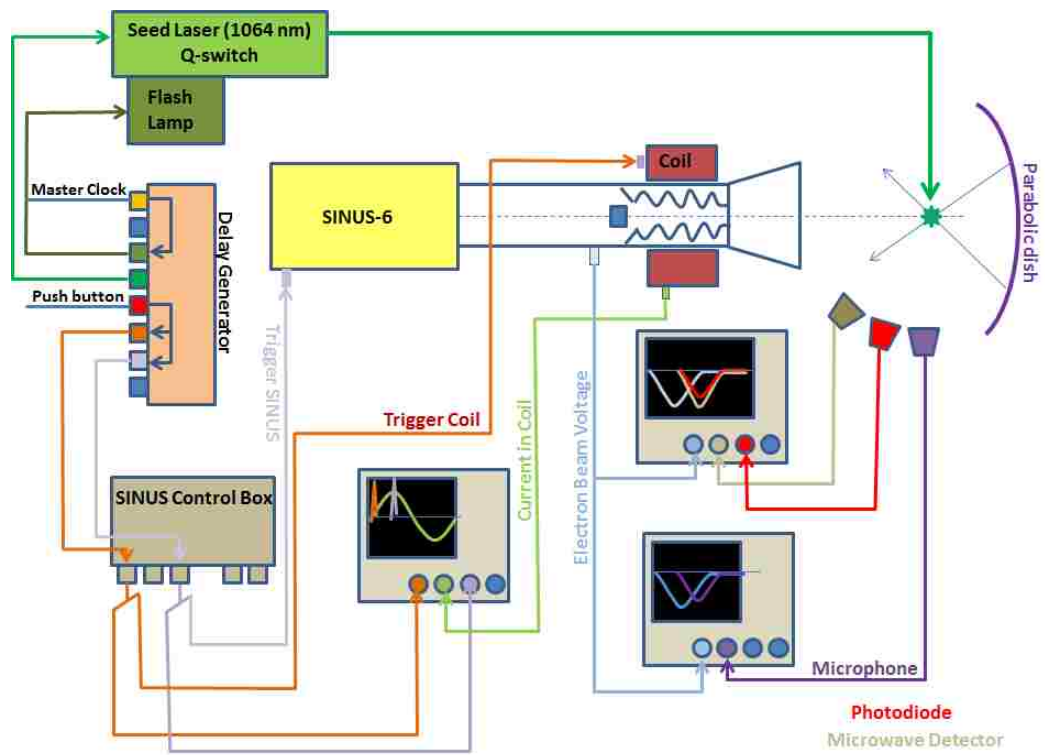
Figure 6.15. Schematic of the experimental and diagnostic setup

6.4 Experimental Results

In this section the diagnostics will be discussed briefly (they have been discussed in more detail in Chapter 5) followed by the experimental results.

6.4.1 Diagnostics

Due to the unavailability of the probe laser that was initially intended for shadowgraphy the experimental data will be analyzed based on the data obtained from a PD, microphone, and microwave detector.

The PD used in these experiments had a rise-time of <10 ns, which makes it suitable for capturing the light signal from the laser spark and also pick up any enhancement of the light signal that may occur due to laser-microwave interaction. A cut-off waveguide was used to detect the microwave signal and was placed next to the PD. Identical cables were used to deliver the signals from the microwave detector and the PD to the oscilloscope. The delay between the two signals was used for determining the temporal synchronization between the two signals. An electret microphone was used to sense variation in the pressure due to air breakdown. The physical locations of each diagnostic are clearly indicated in Fig. 6.15.

6.4.2 Results

The experimental results are presented in this section. Figure 6.16 shows the time delay between the PD signal and the microwave signal taken over a course of two days. The large fluctuation in the data is attributed to the jitter of the two systems, most of which is very likely due to the beam voltage fluctuation. Despite the large jitter the data sample indicates that at least 6 shots out of 100 are well within 100 ns timing accuracy. The negative delays mean that the laser pulse came before the microwaves and the positive delays mean that the laser pulse came after the microwaves. Figure 6.17 shows the screen-shots taken from the oscilloscope for some of data samples that were saved for post processing. It must be noted here that on Day 2 of the experiments the data for delays that fell within +/- 100 ns were captured for post-processing, which made the comprehensive data analysis very challenging.
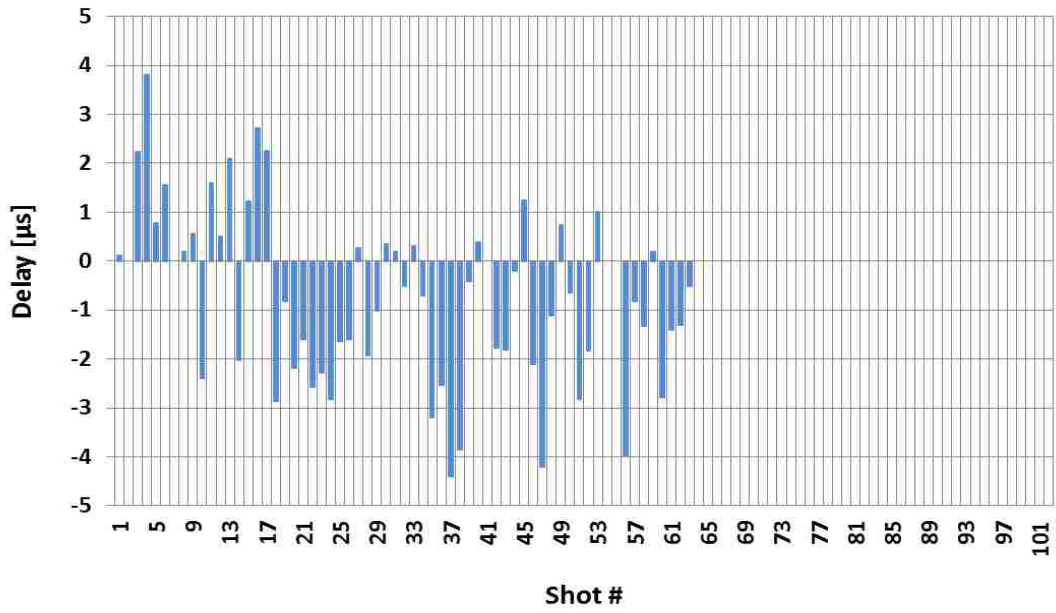
Figure 6.16. (a). Delay between the laser and microwave signal (Day 1).
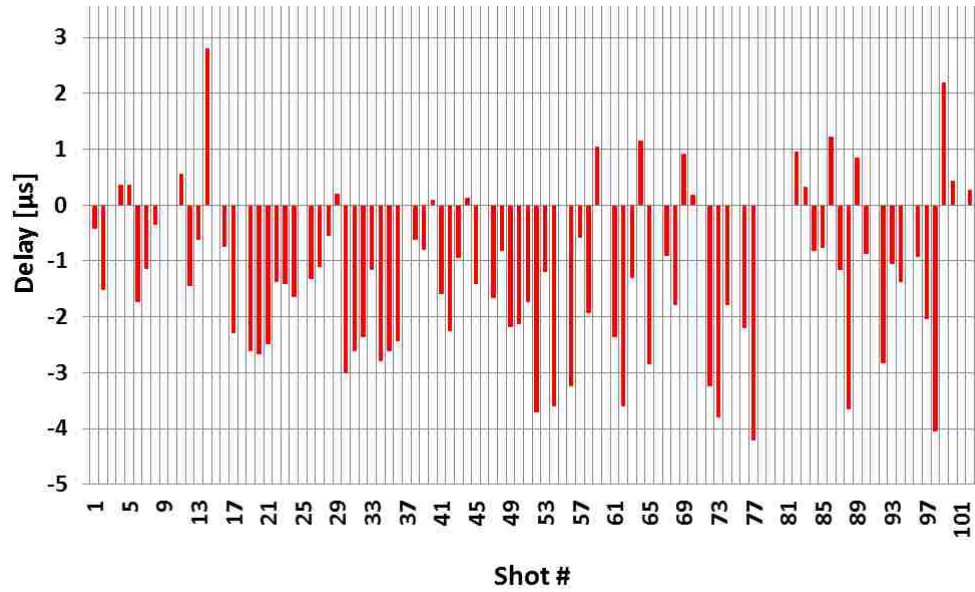
Figure 6.16. (b). Delay between the laser and microwave signal (Day 2).
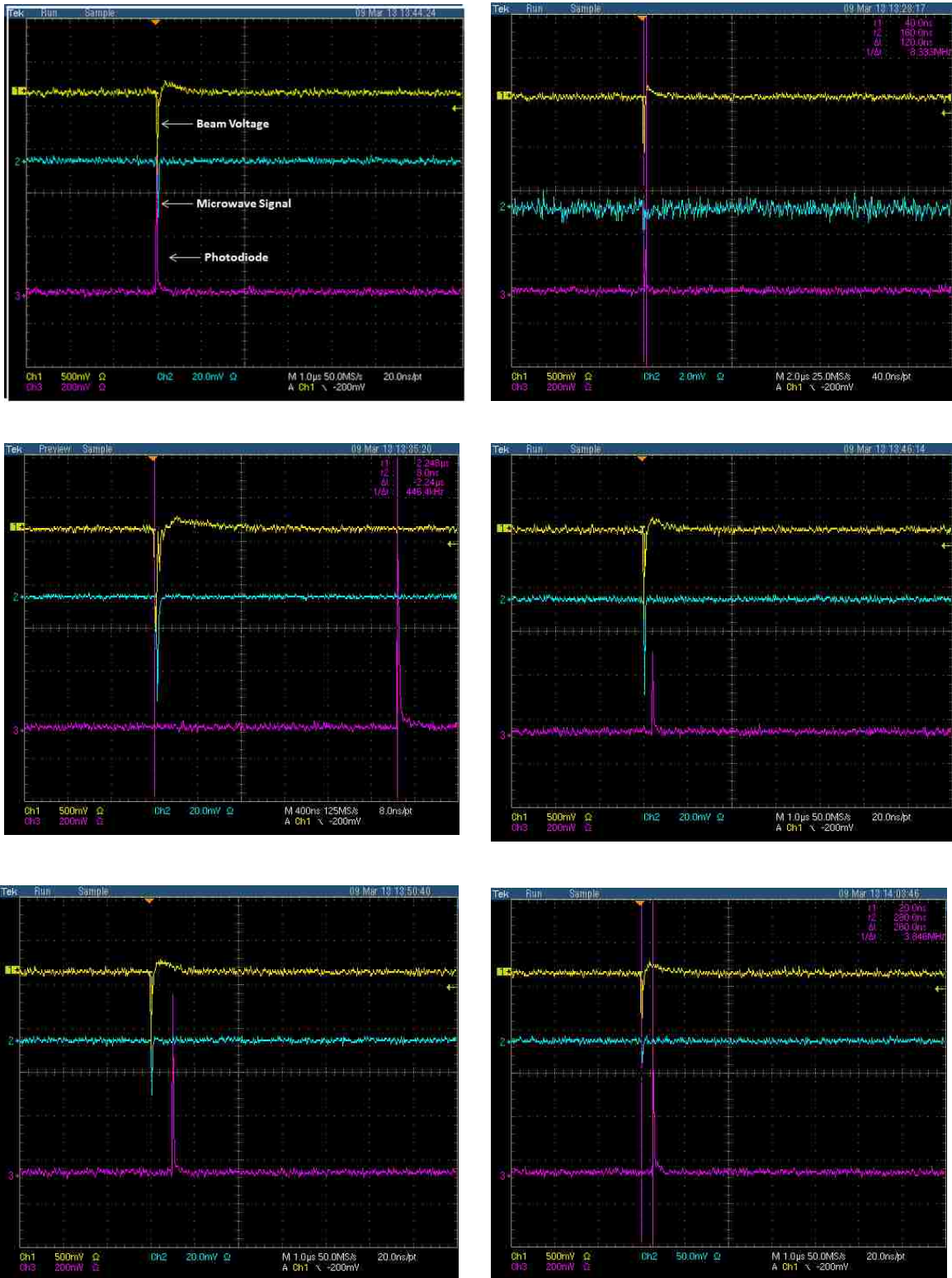
Figure 6.17. Screenshots showing the delay between the PD and the microwave signal (yellow- beam voltage, blue-microwave signal, pink-PD signal).

Figure 6.18 shows the PD amplitude as a function of the delay between the laser and the microwave signal for a sample of 25 shots.
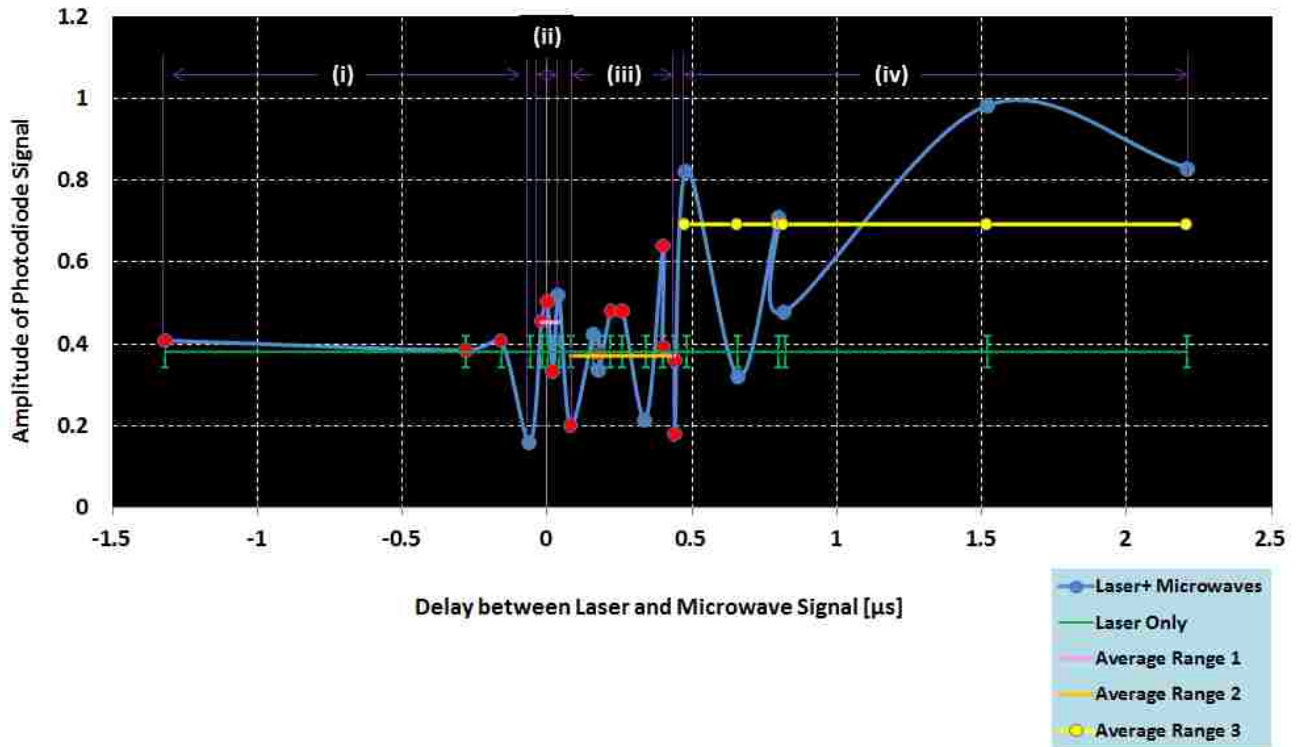
Figure 6.18. PD amplitude as a function of delay between the laser and microwave signal (Blue dots: Day 1, Red dots: Day 2).

The green line is the average data for a sample of 10 pulses taken for the case when just the laser spark was firing. The errors bars on the green data line indicate the fluctuations of the laser light amplitude. This data set serves as a reference for observing the degree of amplification in the PD signal due to laser-microwave interaction.

For analysis the above data set has been divided into four time intervals:

(i) $t_{delay} < -40$ ns (laser spark appeared before the microwave signal),

(ii) t_{delay} between +/- 40 ns (laser and microwave signal within the time range of absolute overlap),

(iii)   40 ns $< t_{delay} < 500$ ns (intermediate range for microwave signal appearing before the laser pulse),

(iv) $t_{delay} > 500$ ns (microwave signal appears well before the laser pulse)

Here t_{delay} represents the delay between the PD and the microwave signal.

(i) For $t_{delay} < -40$ ns there is no amplification in the PD signal. Any aberration falls within the limits of the fluctuations of the laser spark.

(ii) For -40 ns $< t_{delay} < +40$ ns, a slight amplification of the PD signal is detected. This amplification could be attributed to interaction between the laser and the microwave signals.

(iii) For 40 ns $< t_{delay} < 500$ ns, called the intermediate range, the average of the scatter in the data shows no amplification of the PD signal. In fact the data indicates a 3 % drop in the average amplitude of the PD signal compared to the average laser line.

(iv) For $t_{delay} > 500$ ns, where the microwave signal appears well before the laser pulse, there is a noticeable amplification of the PD signal, contrary to our expectations. The average of the scatter shows a 60% increase in the amplitude of the light signal.

A probable explanation of the data trends observed in (ii) and (iv) could be explained using the electron diffusion time. In (ii) the free electrons produced by the microwaves do not have enough time to diffuse and, therefore, when the laser pulse is incident in the volume of ionized air produced by the microwaves the expected avalanche ionization effect is weak. While in (iv) where several hundred nanoseconds have elapsed after the microwave signal, the electrons diffuse further so that when the laser spark is incident upon it the avalanche ionization effect is greatly increased, thus leading to the amplification of the light signal.

However, it must be noted that the amount of data available for the above conclusion is limited and it is therefore recommended that further investigation be carried out to further validate the results presented above.

Figure 6.19 shows the PD response as a function of time for the four time categories described above.

Unfortunately, the microphone data could not be used for analysis and interpretation of the data because of the sensitivity of the electronics to the microwave and X-rays.
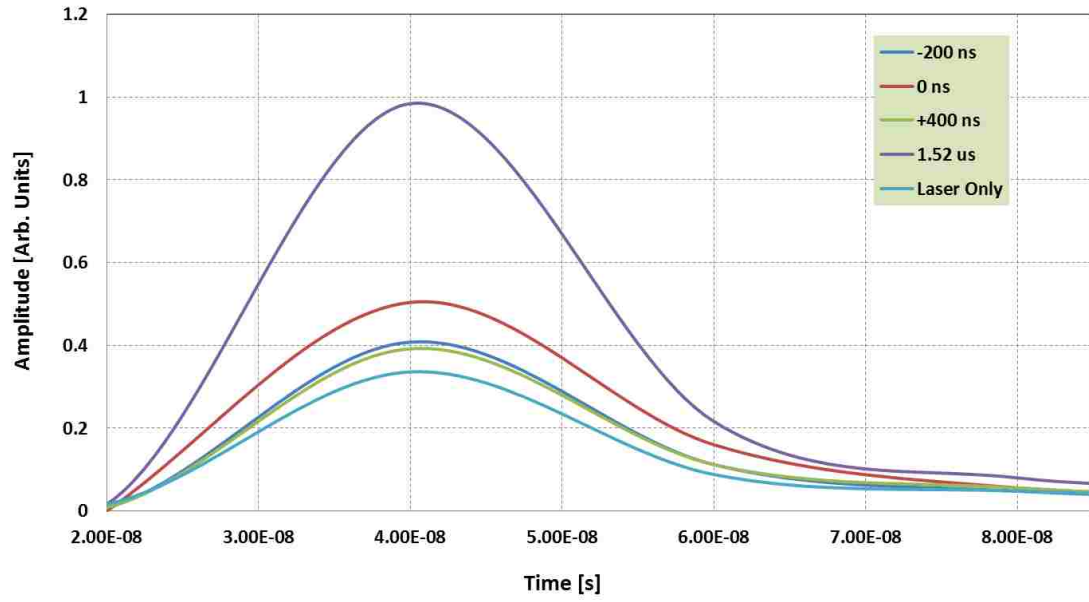
Figure 6.19. PD responses for different time delays.

Chapter 7

EXPERIMENTAL POST DATA ANALYSIS

7.1. Breakdown Threshold Measurement

Based on the Stricker experiment on the breakdown threshold of nitrogen and oxygen, breakdown threshold has been defined as the lowest laser intensity at which a visible spark is produced [73]. Flux which produces air breakdown for 50% of the laser pulses is used as the definition of breakdown threshold in this thesis. The occurrence of breakdown was determined by observing a visible spark at an angle perpendicular to the laser beam direction using a high speed (ns rise time) visible photo detector while gradually increasing the intensity for each laser pulse. The possibility of dry air breakdown for 10 laser shorts for different laser energies is presented in the figure.
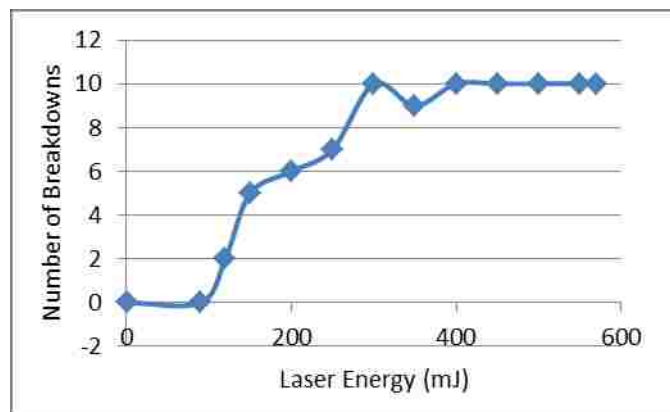
Figure 7.1. Probability of the laser-induced breakdown formation for increasing laser energies.

The temporal decay of light intensity emitted from the LIP, in which the time zero (t = 0) is the beginning of the laser pulse. The measurements were conducted in atmospheric pressure (631 Torr) at room temperature. The primary measurement is the incoming laser energy with the corresponding intensity at the focal spot then calculated. The focal length of the focusing lens used is 20 cm and the width, w_o of the unfocused laser beam used is 7 mm with a laser beam divergences of 0.5 mrad. The focal region can be approximated as a cylindrical shape with the radius of [25]

$$r_s = \frac{f(\Delta\alpha)}{2} = 5.00 \times 10^{-2}\,mm \tag{7.1}$$

and axial focal length (depth of focus) of

$$l_z = \frac{(\sqrt{2}-1)f^2(\Delta\alpha)}{2rw_b} = 11.3 \times 10^{-6}\,m \tag{7.2}$$

where f is the focal length of the lens, r_w is the laser beam radius at the half peak irradiance, and $\Delta\alpha$ is beam divergence ($\Delta\alpha$ = 0.5 mrad for Surlite SLII-20).The diffusion length, δ, can be obtained by [46] [73]

$$\left(\frac{1}{\delta}\right)^2 = \left(\frac{1}{r_s}\right)^2 + \left(\frac{1}{l_z}\right)^2 \tag{7.3}$$

which gives a value of $\delta = 3.7 \times 10^{-5}$, very similar to the value used for laser-induced breakdown in nitrogen and oxygen combined gas [73].

In our experiment, we used different convex lens with f= 5, f = 8 cm, f=20 cm and resulted in breakdown with different dimensions. However, one with a longer focal length and one with a shorter focal length achieved different spot sizes due to laser intensification.

Based on [29], the pulsed laser breakdown data is comparable to the steady state continuous wave microwave breakdown case. Although the laser energy is pulsed (7 ns) the electric field has high oscillation rate within a single pulse. The threshold breakdown in air using a focused laser radiation is independent of pulselength and can be treated as if in steady state if the number of cycles contained within the pulse is more than 10^6 [13],[32].

The breakdown threshold laser intensity I_B at the focal minimum, as mentioned in Chapter 3, is: $I_B = W_B/\pi r^2 t_p$ and the breakdown threshold electric field is determined using [76]:

$$E_b = 1.54 \times 10^4 |r|^{\frac{2}{3}} \quad \text{V/m.} \tag{7.4}$$

In our experiment, we just measure the breakdown threshold for air for atmospheric pressure, 631 Torr. E_b for dry air at 631 Torr was measured to be 36 $\times$ 10^6 V/cm. It was observed [32] that E_m decreases for pressures ranging from 40 Torr to 3800 Torr, which is expected when the laser frequency $\omega = 4.33 \times 10^{14}$ Hz, is higher than the electron collision frequency ν_e. This means that for a high frequency wave fields, there are many oscillations of the electric field per collision. Because of this, we can use the concept of the effective electric field for energy transfer. E_{eff} shows the effectiveness of the electric field in coupling its energy to the electron with the field multiplied by the factor of $1 + \omega^2/\nu_e^2$.

$$E_{eff}^2 = E^2/\sqrt{(1 + \omega^2/\nu_e^2)}. \tag{7.5}$$

The electron collision frequency is by $\nu_e = \beta \times 10^9 \times P$, where β depends on the gas with a value of 5.33 for Air data [29] [73]. The pressure P is in Torr.

As noticed, the propagation of an HPM wave beam through air can lead to breakdown. The high density plasma generated by HPM air breakdown results in the reflection, absorption, scattering, enhancement of the field amplitude, broadening of the breakdown spectrum, and self-focusing of HPM. As the first step, we studied the microwave air breakdown thresholds for different parameters.

In the present work, the beam divergence θ_{div} is assumed to be 1.0 mrad and f = 0.6604 m (26 inches). Using these numbers in the above formulae, we can calculate the characteristic diffusion length

$$\left(\frac{1}{\Lambda}\right)^2 = \left(\frac{1}{L}\right)^2 \left(\frac{2.4}{r}\right)^2 \tag{7.6}$$

which gives a value of $\Lambda = 0.753$ cm.

The threshold for breakdown in air for focused 10 GHz microwave radiation becomes essentially independent of pulselength for durations in excess of 1 ns. For shorter pulse durations, in the picosecond regime, the threshold leads to increase and become less pressure dependent [74]. In this thesis we shall discuss the breakdown phenomena in air near 300 K. At sufficiently low frequency air will breakdown when the rms electric field intensity is greater than

$$E_b = \left[30 \right] \times \left[\text{air pressure (mmHg)} \right]. \tag{7.9}$$

At higher frequencies E_b scales linearly with f, the frequency. The breakdown threshold intensity can be defined as [75]

$$E_{bd} = 1.94 \times 10^2 \sqrt{I_b} \times 10^{-4} \frac{V}{cm} \tag{7.10}$$

where E is the rms field in V/cm and P is expressed in MW/cm^2. MacDonald [46] and Kroll [75] expressed the threshold power flux for breakdown in the form of:

$$P_{bd} = 1.44 \left[p^2 + 2.1 \times 10^6 \times \lambda^{-2} \right] \quad \text{MW/cm}^2, \tag{7.11}$$

where p is the atmospheric pressure in units of standard pressure and λ is the RF wavelength in units of microns. Equation (7.11) can be reexpressed as a function of frequency

$$P_{bd} = 1.44 \left[p^2 + 2.4 \times 10^{-6} \times f^2 \right] \quad \text{MW/cm}^2. \tag{7.12}$$

Figure 7.2 shows the breakdown power as a function of microwave wavelength (f^{-1}) for different pressures as predicted by the microwave formula of Eq. (7.11). Frequency ranges from 1 GHz ($\lambda = 3 \times 10^5 \mu m$) to 100 GHz ($\lambda = 3 \times 10^3 \mu m$). It seems to overestimate the breakdown power by more than an order of magnitude under certain conditions and these results can be extrapolated to laser frequencies.

For some experimental conditions, $\omega/\nu \gg 1$, the effective breakdown electric field is

$$E_{eff} = E_b \left(\frac{\nu}{\omega} \right) \tag{7.14}$$

where ω is the microwave frequency and ν is the electron collision frequency which is given by $\nu = \beta \times P \times 10^9$. P is pressure in Torr, β is a constant related to gas parameters with a values of 5.3 for air [73] [46, 76]. The effective electric field, E_{eff}, is plotted in Figure 7.3 as a function of pressure ranging from 1 atm (see level) to 0.013 atm (100,000 feet) and it is observed to increase within the pressure range which means the effectiveness of energy coupling through electron collisions is higher when compared to lower pressure conditions. The effective breakdown field intensity E_{eff} depends on the actually existing field intensity and can be significantly smaller

depending on the ratio of the RF frequency to the mean collision frequency. The utility of such a comparison has been demonstrated for microwave-generated breakdown in air [46].
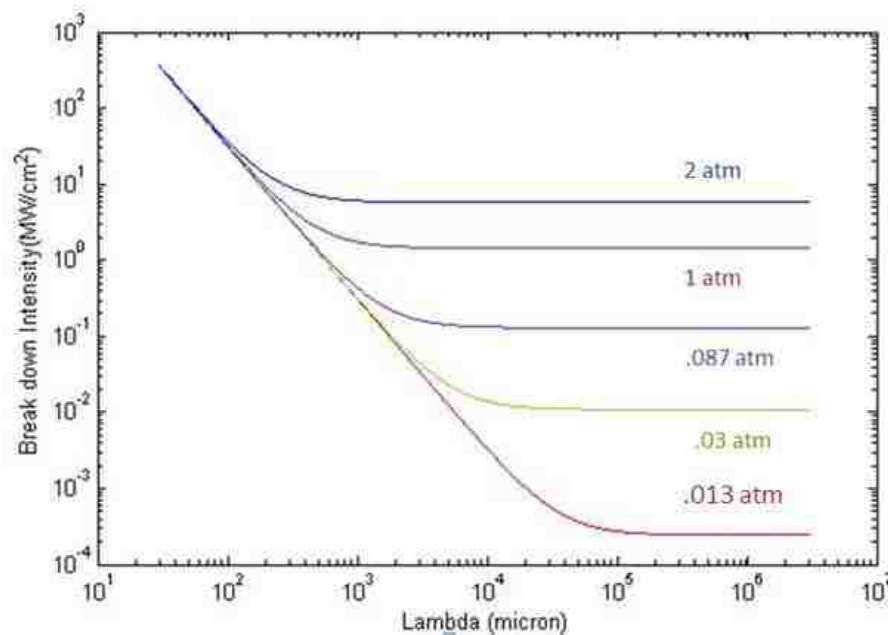
Figure 7.2. The breakdown intensity as a function of microwave wavelength (f -1) for different pressures.

It has been observed that, at 10 GHz RF frequency, for gas pressures above 50 Torr and pulselengths in the 10^{-9} s range (in our case, 7 ns), gas breakdown is best described by the CCI processes [46]. It is important to note that for breakdown at high altitudes the main interest is given to low pressure at the left side of plot. At high frequency the variation of the electric field leads to ionization phenomena in which the diffusion length is much smaller than the value of � obtained from geometry. Thus, at low pressure (high altitude) the large volumes cannot lead to large diffusion lengths. In fact, analysis shows that the ▐ cannot normally exceed a value of approximately one wavelength of electric field (3 cm) [73]. Figure 7.3 is a "universal plot" for microwave breakdown.
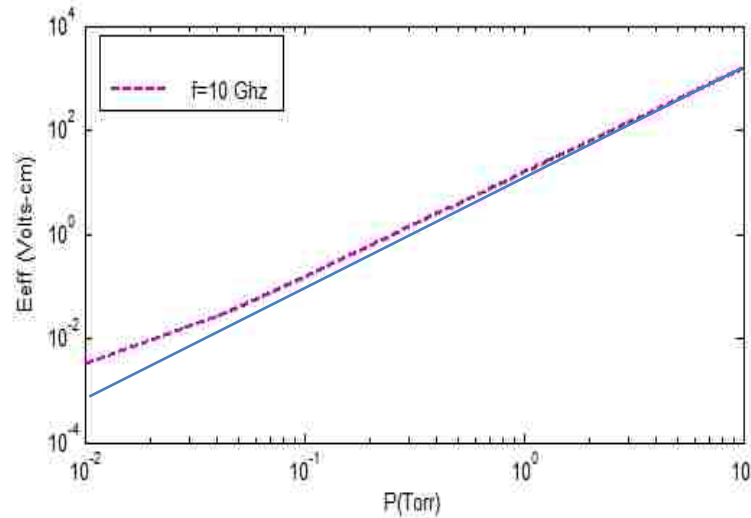
Figure 7.3. Plot of E_{eff} as a function of P for diffusion length, Λ, for 0.753 cm.

Based on this trend the electric field breakdown threshold decreases as a function of pressure. The E_b for 631 Torr (local pressure) can be calculated to be around 35 $\times 10^{6}$ V/cm.

The LIP is compared with microwave data using universal plots and shows good agreement [29]. The universal plot represents major parameters of laser breakdown including pressure, electric field, frequency, and diffusion length.

The values of E_{eff} obtained from our air breakdown data can be compared with microwave universal plots for air. According to this result the breakdown threshold for air at 1064 nm wavelength radiation converges with the microwave breakdown data at sub atmospheric pressures and deviates significantly at very low pressures. For low pressures, the gas is low collisional and the MPI will dominates over the collisional cascade breakdown.

Figure 7.3 shows the laser breakdown data (solid line) for air from 0.013 atm to 10 atm. In order to compare it with the collisional microwave breakdown, the 1064 nm laser-induced breakdown data where MPI processes is important at lower pressures, a correction for the MPI process as a function of pressure is necessary. From the breakdown data, the portion of MPI effects as a function of pressure $p^{-1/3}$ is eliminated by correcting with a multiplicative factor E_{bt} $\times$ [(E_{BCC} *(p)* + E_{BMPI} (p)) / E_{BCC}(P)]. The corrected collisional cascade data shifts to much higher values at low pressures where the MPI process is significant compared to higher pressures where collisional processes dominate. It means that a higher electric field is required in order to obtain breakdown at lower pressures without the influence of MPI processes. The breakdown threshold values were then

multiplied by a scaling factor of 2.2, in order to fit with the microwave breakdown plot to examine the overall trend of the data with pressure.

The scaled data has a good agreement with classical microwave air breakdown. The scaling factor is attributed to the presence of microscopic dust particles of order several microns that has been shown to reduce breakdown for short wavelength lasers but does not influence on the longer wavelength microwave breakdown [37]. The difference between the 10 GHz microwave frequency and the 0.2×10^{15} Hz laser frequency is quite remarkable for pressure scaling.

7.2. Analysis of Plasma Density Decay

Based on the continuity equation and in the absence of an ionizing source, the plasma decay can be described by [33]:

$$\frac{\partial n_e}{\partial t} = D \nabla^2 n_e - \nu_a n_e - \alpha n_e^2 - \beta n_e^3 \tag{7.15}$$

where D is the ambipolar diffusion coefficient, ν_a is the attachment rate, α is the two-body (electron-ion) recombination rate coefficient, and β is the effective radiative recombination rate coefficient for three-body collisions. The term $D\nabla^2 n_e$ represents electron diffusion and is approximated by the term Dn_e/Λ^2 where Λ is the characteristic diffusion length of the laser plasma was calculated in Chapter 3 [77]. The diffusion coefficient can be derived as $D = kT_e/m_e \nu_m$ and ν_m is the electron-molecule effective-collision frequency, given by: $\nu_m = n_n \sqrt{[8kT_e/\pi m_e]}$. Due to higher density in the core of plasma, the low rate of diffusion near the plasma center can be verified. Our experiment shows that the maximum axial length of the laser plasma is approximately 1 cm.

The attachment of an electron to a molecule leads to the formation of a negative ion and corresponds to a decrease in the number of free electrons in the plasma. Air behaves like an electronegative gas. The attachment frequency $\nu_a = \nu_{ada} + \nu_{3ba}$ is the sum of frequencies caused by the two main attachment processes such as the dissociative attachment ν_{ada} $[O_2 + e \rightarrow O^- + O]$ and the three-body attachment ν_{3ba} $[O_2 + e + T \rightarrow O^- + T (T = O_2, N_2)]$ processes. The dissociative attachment frequency is defined as, $\nu_{ada} = h_n \alpha_{dda}$, where h_n is the attachment efficiency, which is a

weak function of electron energy and ν_{en} is the electron neutral collision frequency. Based on Chan the value of $\mu_{en} = 1.5 \times 10^{-4} \, s^{-1}$ [28] and the electron neutral collision frequency is given by $\nu_{en} = n_0 \sigma_0 v_{th}$ where $n_0 = 10^{18} \, cm^{-3}$ [24]. The dissociative electron attachment frequency is $\nu_{att} = 3.1 \times 10^2 \, 1/s$. In the case of three-body attachment reaction O_2 is used as the third body since the same reaction with N_2 as a third body presents much smaller cross sections. The three-body electron attachment rate for the attachment process $O_2 + e + O_2 \rightarrow O_2^- + O_2$ is

$$2.05 \times 10^{-30} \left[\frac{300}{T_e} \right]^{1/2} \exp\left[\frac{600}{T_n} \right] \quad (cm^6/s) \quad [17].$$

For temperature of $T_e = 4000$ K, the three body attachment frequency is $\nu_{3att} = 3.6 \times 10^2 \, S^{-1}$. Based on the experiment that was performed by Thiyagarajan [32], the attachment loss term and diffusion term are small compare to $\frac{\partial n}{\partial t}$ and can be neglected. Thus, the continuity equation can be written as

$$\frac{\partial n_e}{\partial t} = -\alpha n^2 - \beta n n_e^2 \tag{7.16}$$

Another form of loss plays an important role in the post-discharge stage: charged particle recombination (negative ions with positive ions or electrons with positive ions). Similarly, the electron-ion recombination consists of two- and three-body recombination processes. The two-body electron-ion recombination rate, α_r, is a combination of dissociative α_{diss} and radiative α_{rad} recombination rates ($\alpha_r = \alpha_{diss} + \alpha_{rad}$).

The radiative recombination coefficient α_{rad} is

$$\alpha_{rad} = \sigma_{rad} v_e = 2.74 \times 10^{-13} (T_e)^{-1/2} \tag{7.17}$$

The cross section of the radiative recombination mechanism $M^+ + e \rightarrow M + h\nu$ is very small ($\sigma_{rad} \approx 10^{-20}$) [17]. The dissociative recombination process is $M_2^+ + e \rightarrow M^* + M$ (T=O_2, N_2). M^* is an electrically excited state. The electron dissociative recombination coefficients α_{diss} for N_2^+ and O_2^+ as a function of electron temperature T_e can be written as [78, 79]

For N_2^+: $$\alpha_{diss}(e) = 2.02 \times 10^{-6} T_e^{-0.5} \quad cm^3/s, \tag{7.18}$$

For O_2^+: $$\alpha_{diss}(e) = 1.21 \times 10^{-6} T_e^{-0.7} \quad cm^3/s, \tag{7.19}$$

Considering the ratios of N_2 and O_2 (N_2: 79%, O_2: 21%) in air, the total electron-ion dissociative recombination coefficient is: $\alpha_{ei} = 0.79\,\alpha_{ei(N)} + 0.21\,\alpha_{ei(O)}$.

The two body recombination coefficient can be compared with the recombination coefficient calculated from measured electron densities at different times, by using following expression [80]:

$$\alpha_{ei} = \frac{\left|\dfrac{1}{n_{e1}} - \dfrac{1}{n_{e2}}\right|}{|t_2 - t_1|} \tag{7.20}$$

where n_{e1} and n_{e2} are electron density at two closely measurement times t_2 and t_1. It is observed that three body recombination is dominant in early times of post-discharge stage and is larger than the two body recombination process [24].

In three body recombination, a number of electrons are heating the ions and forming the exited atoms ($E_i \gg KT_e$). This process follows by $A^+ + e + e \rightarrow A^* + e$ and it is observed that it is the main recombination process for high density equilibrium plasmas. The excited atoms can go to the ground state by radiative transition. The effective three-body recombination coefficient α_3 (cm^6/s) is a function of electron temperature, as follows from [24], [79]

$$\alpha_3 = 1.32 \times 10^{-24} \left(\frac{T_e}{10^4}\right)^{-4.4} \tag{7.21}$$

Figure 7.4 shows the approximate theoretical plasma decay, which is the integral of the rate equation. The plasma region is assumed to be spherical and isotropically decaying.
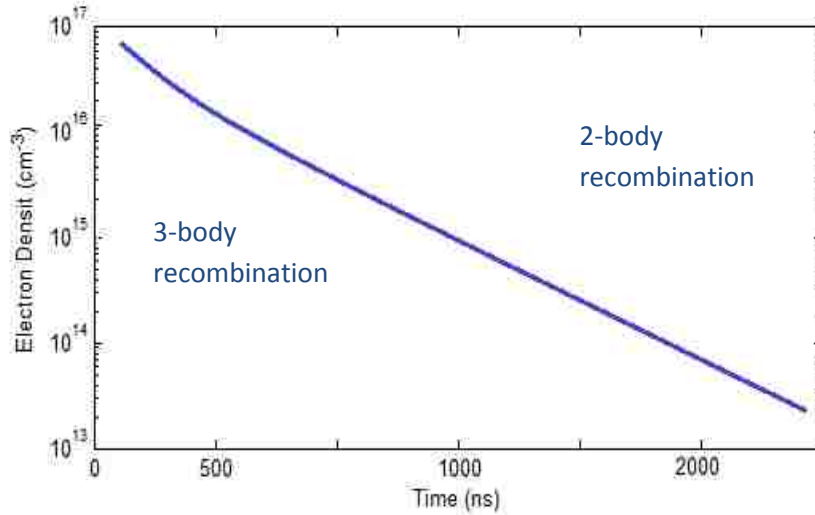
Figure 7.4. Theoretical plasma decay model.

It is obvious that the electron density based on the theoretical model decays at a slow rate due to the fact that only two major loss terms, two- and three-body recombination mechanism, are noticed in the theoretical model. There are other complex air reaction mechanisms involved in air plasma process and they can lead to make a difference between the theoretical mode and the measured data. Due to the approximation that we used, the theoretical calculation is not accurate for t>200 ns.

Chapter 8

CONCLUSIONS, DISCUSSION, AND SUGGESTIONS FOR FUTURE WORK

8.1. Conclusions and Discussions

The measurements and analyses of high power radio electromagnetic waves interacting with a LIP have been investigated. The measurements of laser-induced breakdown for air using a 1064 nm, 600 mJ, 7 ns Nd:YAG laser radiation for atmospheric pressure where significant MPI as well as CCI processes are important has been successfully carried out. The measured breakdown threshold field intensities are scaled to the microwave theory by correcting for the MPI processes at atmospheric pressure. For 600 ± 5 mJ (804 mV) laser incident energy, an average of 86 mV was measured by energy meter to be transmitted through the plasma. It is 93% of the incident energy. Therefore, approximately 540 mJ of the Nd:YAG laser pulse energy was absorbed at 631 Torr by the laser plasma at the focal region. The energy absorbed by the plasma can be increased by increasing the pressure.

Diagnostics, such as PD, microphone, and microwave detector, were implemented to analyze the spatial and temporal evolution of the LIP and also its synchronization with the HPM wave beam. By using these diagnostics and analytical calculations, the plasma volume, shockwave velocity, and hot core air pressure were measured. An average shockwave velocity of 4×10^4 m/sec was measured from the expanding plasma.

The theoretical propagation characteristics of electromagnetic waves through a nonuniform laser plasma were also studied. The transmitted, absorbed, reflected, and scattered powers have

been calculated using the impedance transformation technique. It showed that the laser plasma can be used as a tunable microwave absorber for radar and stealth applications.

8.2. Suggestions for Future Work

In this Thesis, the physics and features of 1064 nm Q-switched Nd:YAG LIP in atmospheric air is characterized using different diagnostics. The laser focused system and optical diagnostics are well developed in the experiment. The LIP formed agrees well with the classical and quantum mechanical microwave breakdown theories [29]. In addition, interaction of an HPM wave beam and the LIP is studied experimentally and analytically. With these understandings this research can be further extended in several areas. The suggestions for future work are as follows.

8.2.1. Angle and Polarization of Incident Electromagnetic Wave - Influence of Secondary Electron Impact

In the interaction of an HPM wave beam and LIP studies, it has been observed that the incident angle of the electromagnetic waves also play a significant role in the absorption efficiency. This is due to the secondary electron emission profile with respect to the angle of incidence. The secondary electron emission coefficient is a function of both incident energy and incident angle of the electromagnetic wave, as shown in Fig. 8.1.

It was also shown [60] that an overcritical density plasma slab can be totally absorptive to an obliquely incident electromagnetic wave. High absorption is achieved due to the interference of the evanescent waves in the subcritical region. The transmission coefficient has the resonant character due to the excitation of a plasma surface mode. In a warm plasma case, the excitation of the propagating longitudinal, electrostatic, modes becomes possible. It is demonstrated that these longitudinal excitations facilitate the total absorption of an opaque plasma slab creating additional resonances in the absorption property of the system.
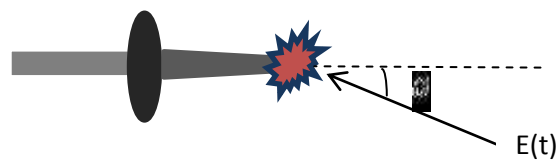

Figure 8.1. Schematic of the energy and angle of incidence of electromagnetic wave.

8.2.2. Effect of Laser Beam Polarization

The Q-switched laser beam is an unpolarized uniform intensity beam. Different beam polarization has different effects on energy absorption. The effect of polarizing the laser beam on the breakdown threshold for dry air by either perpendicular polarized or parallel polarized mode suggests an important area to be explored.

8.2.3. UNM PUSRAD 110

To increase the temporal and spatial synchronization probability, it is possible to use another electron beam accelerator. The University of New Mexico's (UNM's) Pulserad 110 electron beam accelerator can be used to produce a voltage pulse with a rise time of 4 ns, duration of 30 ns, maximum current of 18 kA, and amplitude of 350 kV into a 20 ns load. The basic construction of the Pulserad 110a electron beam accelerator comprises a 6-stage Marx bank, 20 ohm, 30 ns pulse forming line, a fast oil-breakdown switch, a matched transmission line, an oil-vacuum interface, a low inductance vacuum chamber, and a load. With its present design Pulserad 110a is capable of delivering a total power of 6.3 GW to a matched load of 20 ohm. The most significant feature of the Pulserad 110 is the oil-breakdown switch that has been designed to give the pulse a rise time of less than 4 ns. We can use the Pulserad 110 accelerator to drive a relativistic magnetron to produce HPM to deliver 1 GW peak power with the frequency of 3.4 GHz (s-band). The advantages of this setup would be:

I) It could be externally triggered by a delay generator and therefore be easily synchronized with the laser system in the temporal domain.

II) Microwave power extracted from the magnetron will reach 1 GW causing high density ionization, thereby making it easier to detect the air breakdown plasma by shadowgraphy.

III) Microwave pulse duration would be at least 3 times longer than the current test setup, which would increase the chances of laser spark-μwave radiation.

IV) The magnetron oscillating at a frequency three times less than the BWO would again improve the overall laser spark-μwave interaction.

Furthermore, a better physical evolution model of the LIP in atmospheric pressure and more complete description of the propagation of electromagnetic wave in laser plasma can be suggested. Development of a computer code written in more a powerful PIC based language (e.g., FORTRAN

and C), in a new graphical representation of data output, and with fully automatic link to diagnostic equipment, could give information about the LIP or physical characteristic of the enhancement of LIP with an HPM wave beam.

The hypothesis of plasma defocusing, rather than plasma absorption, can be assumed in this Thesis to be the main cause of the so-called 'plasma shielding' observed in laser plasmas; additional study has to be performed in the future to corroborate this statement.

For future work, better diagnostic equipment, including a CCD fast speed camera, shadowgraphy, and spectroscopy, are needed to accurately determine the plasma enhancement characteristics during laser microwave interaction, identifying the initiating of ionization, and plasma duration time.

To reduce the jitter time of spark gap switch, it is possible to use another type of switch such as laser triggered spark gap switch. It is also possible to reduce the size of switch by using another type gas such as SF_6.

Appendix

A.1. Two Dimensional Fast Fourier Transform

Fewer operations are required when a two-dimensional Fast Fourier Transform (FFT) algorithm is applied to evaluate Eq. (2.15) numerically. For this purpose it is noted that the steady state version ($U = 1$) of Eq. (2.15) can be rewritten as

$$T(x, y, z, t) = \int_{-\infty}^{+\infty} \int_{-\infty}^{+\infty} AI(x', y', z') W(x - x', y - y', z, t) \, dx' \, dy' \tag{A.1}$$

which is a convolution of the intensity profile AI and the function W, with respect to the coordinates x and y, i.e., $T = AI * W$, where $*$ denotes the convolution operator. Hence, by applying the two-dimensional Fourier transform $F_2\{.\}$, Eq. (2.15) can be rewritten as

$$F_2\{T\} = F_2\{AI * W\} = A \, F_2\{I\} F_2\{W\} \tag{A.2}$$

where the well-known equality $F_2\{f * g\} = F_2\{f\} F_2\{g\}$ has been applied. Finally, by applying the inverse Fourier transform to this expression yields,

$$T = A F_2^{-1}\{F_2\{I\} F_2\{W\}\} \tag{A.3}$$

By replacing the continuous convolution by discrete convolution, and using the two-dimensional FFT method, the temperature distribution 2.15 can be calculated numerically. This method was used to calculate the temperature profile in a substrate.

A basic condition for the two-dimensional Fourier transformation is that the function to be transformed is periodic in the xy plane. This is not the case for the intensity profile I and the function W, and will introduce errors in the evaluation of the temperature distribution. These errors are introduced by the truncation of I and, i.e., if L (grid size) is chosen too small, then for $\|y\| > L$ and $\|y\| > L$, $W(x, y) \neq 0$ and $I(x, y) \neq 0$. The errors are significant for low temperatures only. To reduce these errors, the region of calculation should be chosen sufficiently large. As a rule of thumb, one should choose $L > 3d$, where d is the diameter of the laser beam.

A.2. Time Delay Between Voltage on the Line and Photodiode Voltage

Table A.1 The time delay between voltage on the line and the PD voltage.

SHOT	DELAY	SHOT	DELAY	SHOT	DELAY	SHOT	DELAY
Shot 1	0 ns	Shot 5	200 ns	Shot 9	180 ns	Shot 13	260 ns
Shot 2	360 ns	Shot 6	80 ns	Shot 10	320 ns	Shot 14	200ns
Shot 3	360 ns	Shot 7	120 ns	Shot 11	420 ns	Shot 15	0 ns
Shot 4	0 ns	Shot 8	0 ns	Shot 12	0 ns	Shot 16	0 ns

List of References

1. N. Kroll and K. M. Watson, "Theoretical study of ionization of air by intense laser pulses," Phys. Rev., Vol. A 5, pp. 1883-1905, 1972.

2. P. F. Browne, "Mechanism of gas breakdown by lasers," Proc. Phys. Soc. London, Vol. 86, pp. 1323-1332, 1965.

3. P. Schaaf, *Laser Processing of Materials Fundamentals, Applications and Developments.* New York: Springer, 2010, p. 234.

4. O. M. Gradov and L. Stenflo, "Anomalous transmission of electromagnetic energy through a plasma slab," Phys. Scr., Vol. 25, pp. 631-631, 1982.

5. F. Y. Jin, "Effects of external magnetic field on propagation of electromagnetic wave in uniform magnetized plasma slabs," Comput. Phys. Commun., Vol. 175, pp. 545-552, 2006.

6. R. A. Kishek, "Multipactor discharge on metals and dielectrics: Historical review and recent theories," Phys. Plasmas, Vol. 5, pp. 2120-2126, 1998.

7. B.A. Demidov et al., "Energy absorption caused by beam instability of plasma in toroidal system," Sov. Phys. JETP, Vol.19, pp. 337-339, 1964.

8. J. B. Pendry, "Negative refraction makes a perfect lens," Phys. Rev., Vol. 85, pp. 3966-3969, 2000.

9. R. J. Vidmar, "On the use of atmospheric-pressure plasmas as electromagnetic reflectors and absorbers," IEEE Trans. Plasma Sci., Vol. 18, pp. 733-741, 1990.

10. M. Laroussi, "Interaction of microwave with atmospheric pressure plasmas," Int. J. Infrared Millim. Waves, Vol. 16, pp. 2069-2083, 2003.

11. M. Laroussi and W.T. Anderson, "Attenuation of electromagnetic waves by a plasma layer at atmospheric pressure," Int. J. Infrared Millim. Waves, Vol. 19, pp. 453-464, 1998.

12. B. J. Hu S. L. Lai, "SMM analysis of reflection, absorption, and transmission from nonuniform magnetized plasma slab," IEEE Trans. Plasma Sci., Vol. 27, pp. 1131-1136, 1999.

13. B. Guo and X.G. Wang, "Power absorption of high-frequency electromagnetic waves in a partially ionized magnetized plasma," Phys. Plasmas, Vol. 12, pp. 84506-84509, 2005.

14. D. L. Tang, "Interaction of electromagnetic waves with a magnetized nonuniform plasma slab," IEEE Trans. Plasma Sci., Vol. 31, pp. 405-410, 2003.

15. L. J. Radziemski and D.A. Cremers, *Lasers-Induced Plasmas and Applications*. New York: Marcel Dekker, 1998, p.437.

16. P. Raizer, *Gas Discharge Physics*. New York: Springer, 1999, p. 449.

17. T. P. Hughes, *Plasma and Laser Light*. New York: Wiley and Sons, 1975, p. 449.

18. G. Bekefi, *Principles of Laser Plasmas.* New York: Wiley, 1976, p.695.

19. J. P. Singh and S.N. Thakur, *Laser-Induced Breakdown Spectroscopy*. Amsterdam: Elsevier, 2007, p. 429.

20. C. H. Chan, "Significant loss mechanisms in gas breakdown at 10.6 μm," J. Appl. Phys., pp. 441179-441188, 1973.

21. S. Soubacq E Schall and J Batina, "Investigation of a gas breakdown process in a laser-plasma experiment," J. Phys. D Appl. Phys, Vol. 37, pp. 2686-2702, 2004.

22. A. Yu, Il'inski'i and L.V. Keldysh, *Electromagnetic Response of Material Media*. New York: Plenum Press, 1994, p. 63.

23. J. Stricker and J. G. Parker, "Experimental investigation of electrical breakdown in nitrogen and oxygen induced by focused laser radiation at 1.064 μm," J. Appl. Phys., Vol. 53, pp. 851-855, 1982.

24. M. Thiyagarajan and S. Thompson, "Optical breakdown threshold investigation of 1064 nm," J. Appl. Phys., Vol. 111, pp. 73302-73309, 2012.

25. M. Young and M. Hercher, "The dynamics of laser-induced breakdown in gases," J. Appl. Phys., Vol. 38, pp. 4393-4340, 1967.

26. P. Veyrié, "Contribution à l'étude de l'ionisation et du chauffage des gaz par le rayonnement d'un laser déclenché," J. Phys. France, Vol. 31, pp. 41-56, 1970.

27. R. A. Zeldovich, *Physics of Shockwave and High-Tempreture Hydrodynamic Phenomena*. New York: Academic Press, 1996, p. 896.

28. M. Laroussi, "Interaction of microwave with atmospheric pressure plasmas," Int. J. Infrared Millim. Waves, Vol. 16, pp. 2069-2083, 1995.

29. A. D. MacDonald, *Microwave Breakdown in Gases*. New York: Wiley, 1995, p. 201.

30.   M. Thiyagarajan and J. E. Scharer, "Experimental Investigation of 193-nm Laser Breakdown in Air," IEEE Trans. Plasma Sci., Vol. 36, pp. 2512-2521, 2008.

31.   A. Braun G. Korn, X. Liu, D. Du, J. Squier, and G. Mourou, "Self-channeling of high-peak power femtosecond laser-pulses in Air," Opt. Lett., Vol. 20, pp. 73-75, 1995.

32.   M. D. Perry, "Multiphoton ionization of the noble-gases by an intense 10^{14}-W/Cm^2 dye-laser," Phys. Rev. A., Vol. 37, pp. 747-760, 1998.

33.   I. P. Shkarofsky, "Review of gas-breakdown phenomena induced by high-power lasers," RCA Rev., Vol. 35, pp. 48-78, 1974.

34.   F. V. Bunkin and M.V. Fedorov, "Bremsstrahlung in a strong radiation field," Sov. Phys. JETP., Vol. 22, pp. 844-847, 1966.

35.   Y. R. Zeldovich, "Cascade ionization of light by a light pulse," Sov. Phys. JETP., Vol. 20, pp. 772-779, 1964.

36.   K. R. Stalder, R. J. Vidmar and D. J. Eckstrom, " Observations of strong microwave absorption in collisional plasmas with gradual density gradients," J. Appl. Phys., Vol. 72, pp. 5089-5094, 1997.

37.   J. T. Chia, S. E. Martin, D. R. Carlson, R. J. Jones, and E. M. Wright "Operating characteristics of a femtosecond amplification cavity for infrared frequency combs", Phys. Rev., Vol. 87, pp. 23817-23824, 2013.

38.   T. Ditmire, "Simulations of heating and electron energy distributions in optical field ionized plasmas," Phys. Rev., Vol. 54, pp. 6735-6740, 1996.

39.   W. E. Scharfman and T. Morita, "Focused microwave technique for measurement of ionization rate collision frequency," J. Appl. Phys., Vol. 35, pp. 2016-2020, 1964.

40.   F. L. Morgan, R. Evans, and C.G. Morgan, "Laser beam induced breakdown in helium and argon," J. Appl. Phys., Vol. 4, pp. 225-235, 1971.

41.   C. H. Chan, C. D. Moody, and W. B. Mcknight, "Significant loss mechanisms in gas breakdown at 10.6 μm," J. Appl. Phys., Vol. 44, pp. 1179-1188, 1971.

42.   W. P. Allis and D.J. Rose, "The transition from free to ambipolar diffusion," Phys. Rev., Vol. 93, pp. 84-93, 1954.

43.   A. V. Gurevich, N. D. Borisov, and G. M. Milikh, *Physics of Microwave Discharge: Artificially Ionized Regions in the Atmosphere.* Amsterdam: OPA, 1997, p. 205.

44.   E. Schamiloglu, R. Jordan, M. D. Harworth, L. D. Moreland, I. V. Pegel, and A. D. Roitman "High-power microwave-induced TM(01) plasma ring," IEEE Trans. Plasma Sci., Vol. 24, pp. 6-7, 1996.

45.   T. A. Milligan, *Modern Antenna Design*. New York: McGraw-Hill, 1985, p. 632.

46.   A. D. Macdonald, D. U. Gaskell, and H. Gitterman, "Microwave breakdown in air, oxygen, and nitrogen," Phys. Rev., Vol. 130, pp. 1841-1850, 1963.

47.   D. A. Lisak, "Breakdown in air-filled microwave waveguides during pulsed operation," J. Appl. Phys., Vol. 56, pp. 1414-1419, 1984.

48.   K. L. Kelly, "Microwave reflections from a vacuum ultraviolet laser produced plasma sheet," J. Appl. Phys, Vol. 85, pp. 63-68, 1999.

49.   B. J. Hu, G. Wei, and S.L. Lai, "SMM analysis of reflection, absorption, and transmission from nonuniform magnetized plasma slab," IEEE Trans. Plasma Sci., Vol. 27, pp. 1131-1136, 1999.

50.   S. S. Harilal, "Influence of ambient gas on the temperature and density of laser produced carbon plasma," Appl. Phys. Lett., Vol. 72, pp. 167-169, 1998.

51.   W. Shen, "Properties of a vacuum ultraviolet laser created plasma sheet for a microwave reflector," J. Appl. Phys., Vol. 78, pp. 6974-6979, 1995.

52.   M. Friedman and S. M. Hamberger, "Electrical conductivity of a highly turbulent plasma," Phys. Rev. Lett., Vol. 21, pp. 674-677, 2003.

53.   L. E. Gurevich and R. G. Tarkhany, "Propagation of electromagnetic waves in a quantizing magnetic field in a uniaxial crystal with an electron plasma," Sov. Phys. Semicond., Vol. 3, pp. 962-966, 1970.

54.   M. A. Heald, C. B. Wharton, *Plasma Diagnostics with Microwaves.* Malabar: R. E. Krieger Pub. Co., 1978, p. 258.

55.   B. A. Moliton, *Basic Electromagnetism and Materials.* New York: Springer, 2010, p. 427.

56.   J. Santoru and D.J. Gregoire, "Electromagnetic-wave absorption in highly collisional plasmas," J. Appl. Phys., Vol. 74, pp. 3736-3743, 1993.

57.   S. Babaei and M.S. Solari, "Microwave attenuation of hydrogen plasma in carbon nanotubes," J.Appl. Phys., Vol. 104, pp. 124315-124319, 2008.

58.   C. X. Yuan, "Propagation of terahertz waves in atmospheric pressure microplasma with Epstein electron density profile," J. Appl. Phys, Vol. 109, pp. 63305-63310, 2011.

59. Y. P. Bliokh, J. Felsteiner, and Y.Z. Slutsker, "Total absorption of an electromagnetic wave by an overdense plasma," Phys. Rev. Lett., Vol. 95, pp. 73301-73309, 2005.

60. E. Fourkal, "Evanescent wave interference and the total transparency of a warm high-density plasma slab," Phys. Plasmas, Vol. 13, pp. 92113-92121, 2006.

61. D. R. Smith, D. Schuring, and J. B. Pendry, "Negative refraction of modulated electromagnetic waves," Appl. Phys. Lett., Vol. 81, pp. 2713-2715, 2002.

62. G. S. Settles, *Schlieren and Shadowgraph Techniques: Visualizing Phenomena in Transparent Media*. New York: Springer, 2001, p. 376.

63. I. H. Hutchinson, *Principles of Plasma Diagnostics.* Boston: Cambridge Uni. Press, 2009, p. 433.

64. M. Villagran-Muniz, H. Sobral, and E. Camps, "Shadowgraphy and interferometry using a CW laser and a CCD of a laser-induced plasma in atmospheric air," IEEE Trans. Plasma Sci., Vol. 29, pp. 613-616, 2001.

65. F. Vidal, "Modeling the triggering of streamers in air by ultrashort laser pulses," IEEE Trans. Plasma Sci., Vol. 28, pp. 418-433, 2000.

66. J. Yu, "Sonographic probing of laser filaments in air," Appl. Opt., Vol. 42, pp. 7117-7120, 2003.

67. A. Talebpour, M. Abdel-Fattah, and S.L. Chin, "Focusing limits of intense ultrafast laser pulses in a high pressure gas: road to new spectroscopic source," Opt. Commun., Vol. 183, pp. 479-484, 2000.

68. J. Kasparian, R. Sauerbrey, and S.L. Chin, "The critical laser intensity of self-guided light filaments in air," Appl. Phys. B, Vol. 71, pp. 877-879, 2000.

69. A. Talebpour, J. Yang, and S.L. Chin, "Semi-empirical model for the rate of tunnel ionization of N-2 and O-2 molecule in an intense Ti : sapphire laser pulse," Opt. Commun., Vol. 163, pp. 29-32, 1999.

70. J. Dowden, P. Kapadia, and N. Postacioglu, "An analysis of the laser plasma interaction in laser keyhole welding," J. Phys. D-Appl. Phys., Vol. 22, pp. 741-749, 1989.

71. K. J. Jankowski and E. Reszke, *Microwave Induced Plasma Analytical Spectrometry.* CA: RSC, 2011, p. 248.

72. V. N. Rai, M. Shukla, and H.C. Pant, "An x-ray biplanar photodiode and the x-ray emission from magnetically confined laser produced plasma," Pramana, Vol. 52, pp. 49-65, 1999.

73. J. Stricker and J.G. Parker, "Experimental investigation of electrical breakdown in nitrogen and oxygen induced by focused laser-radiation at 1.064 μm," J. Appl. Phys., Vol. 53, pp. 851-855, 1982.

74. P. Belland, C. DeMichelis, M. Mattioli, and R. Papoular ,"Spectral analysis of backscattered light from a laser-produced plasma," Appl. Phys. Lett., Vol. 18, pp. 32-33, 1971.

75. R. Tambay R. K. Thareja, "Laser-induced breakdown studies of laboratory air at 0.266, 0.355, 0.532, and 1.06 μm," J. Appl. Phys., Vol. 70, pp. 2890-2892, 1991.

76. U. Jordan, "On the effective diffusion length for microwave breakdown," IEEE Trans. Plasma Sci., Vol. 34, pp. 421-430, 2006.

77. A. Garscadden, M. J. Kushner, and J. G. Eden, "Plasma physics issues in gas-discharge laser development," IEEE Trans. Plasma Sci., Vol. 19, pp. 1013-1031, 1991.

78. A. Takahashi and K. Nishijima, "Kinetic model of gas heating of laser-produced plasmas by CO_2 laser in atmospheric air," Japn. J. Appl. Phys., Vol. 37, pp. 313-319, 1998.

79. X. M. Zhao, "Femtosecond ultraviolet-laser pulse induced lightning discharges in gases," IEEE J. Quantum Electron., Vol. 31, pp. 599-612, 1995.

80. K. Akhtar, "Characterization of laser produced tetrakis (dimethylamino) ethylene plasma in a high-pressure background gas," IEEE Trans. Plasma Sci., Vol. 32, pp. 813-822, 2004.

81. S. Prasad, C. Leach, k. Prestwich, C. J. Buchenauer, M. Fuks, and E. Schamiloglu, "Experimental demonstration of the output characteristics of the A6 magnetron on pulserad 110a, a very short rise-time accelerator at UNM," IEEE Vac. Electron. Conf., pp. 495-496, 2012.

82. G. A. Askar'yan, "Laser-induced waveguide propagation concept," Sov. Phys. JETP., Vol. 28, pp. 732, 1969.

83. A. Gaeta, "Catastrophic collapse of ultrashort pulses," Phys. Rev. Lett., Vol. 16, pp. 3582-3585, 2000.

84. M. Carlos, *Microwave Discharges: Fundamentals and Applications.* New York: Plenum, 1992, p. 564.

85. J. A. Stratton, *Electromagnetic Theory.* New York: McGraw-Hill, 2007, p. 615.

86. L. A. Vainshtein, *Electromagnetic Waves.* Moscow: Radio i Svyaz', 1988, p. 354.

87. N. A. Bogatov, A. I. Kuznetsov, A. I. Smirnov and A. N. Stepanov, "Channeling of microwave radiation in a double line containing a plasma filament produced by intense femtosecond laser pulses in air," Quantum Electron., Vol. 39, pp. 39-985, 2009.

88. O. M. Gradov and L. Stenflo, "Anomalous transmission of electromagnetic energy through a plasma slab," Phys. Scr., Vol. 25, pp. 631-631, 1982.

89. V.V. Valuev, A.E. Dormidonov, V.P. Kandidov, S.A. Shlenov, V.N. Kornienko, V.A. Cherepenin, "Plasma channels formed by a set of filaments as a guiding system for microwave radiation," J. Commun. Technol. Electron., Vol. 55, pp. 208–214, 2010.